Numerical approaches to model and monitor geomechanical reservoir integrity

Dissertation

Zur Erlangung des akademischen Grades

"Doktor der Naturwissenschaften"

Im Promotionsfach Geologie/Paläontologie

Am Fachbereich 09 für Chemie, Pharmazie, Geographie und Geowissenschaften

der Johannes Gutenberg-Universität Mainz

von

Beatriz Martínez Montesinos

geboren in Barcelona, Spanien

JOHANNES GUTENBERG UNIVERSITÄT MAINZ

JG|U

Mainz, 2019

Abstract

The emergence of new ideas to obtain energy from the earth subsurface and to store radioactive waste on it impels us to further investigate the response of geological media to forces and temperature variations.

For instance, injection of water into wells at high pressures to create fractures and increase permeability of rocks is a widely employed technique to enhance geothermal systems or gas reservoirs. Therefore, increasing our understanding about how such actions influence and are affected by the local stress state of the reservoir and how fractures propagate through it is necessary to efficiently develop extraction projects and, hopefully, to avoid undesired side effects.

Also, placing nuclear waste in repositories below the surface monitored by acoustic transmission of seismic signals is currently under investigation. Whereby, an optimal knowledge about how the heterogeneity of the medium and its changes are reflected on the seismic waves is necessary for the correct interpretation of the collected signals.

The physics involving these geological processes can be approximately expressed in a mathematical way through the laws of physics and the constitutive relationship of materials deriving in a set of partial differential equation whose complexity depends on the adopted physical model and the rheology of materials to be modelled. As, in most cases, the governing equations are not susceptible to analytical solutions, efficient numerical methods and software are required to simulate realistic problems.

We present, by a compilation of current theories, a general mathematical model describing the physics of poro-visco-elasto-plastic geological media.

Moreover, on the one hand, we present a computational massively-parallel 3D code to model fluid injection and crack propagation in poro-visco-elasto-plastic rheologies. We reproduce existing 2D benchmarks and give some examples of 3D cases. The results show the importance of the initial stress conditions on the development of failure zones and give a generalization of failure patterns generated from a local increase of pore pressure. Furthermore, we perform simulations of hydraulic fracturing for Well KM-8, UK, showing the significant influence of the permeability of rocks and its changes after fracturing on the development of failure areas.

On the other hand, we use the wave propagation software Sofi2D to simulate the seismic monitoring of a deep circular backfilled tunnel with the aim of increasing our ability to understand path effects and, therefore, to infer the situation inside a nuclear waste repository over time. We apply our results on the Full-Scale Emplacement Experiment at the Mont Terri underground rock laboratory.

Zusammenfassung

Die Entstehung neuer Ideen zur Gewinnung von Energie aus dem Untergrund der Erde und zur Lagerung radioaktiver Abfälle veranlasst uns dazu, die Reaktion geologischer Materialien auf Kraft- und Temperaturschwankungen weiter zu untersuchen.

Beispielsweise ist die Injektion von Wasser in Bohrlöchern bei hohen Drücken, um Brüche zu erzeugen und die Permeabilität von Gesteinen zu erhöhen, eine weit verbreitete Technik, um die Förderrate in geothermischen Systemen oder Kohlenwasserstoffspeichern zu verbessern. Daher ist ein besseres Verständnis, wie sich solche Aktionen auf den lokalen Spannungszustand des Reservoirs auswirken und von diesem beeinflusst werden, und die Art und Weise, wie sich Risse durch dieses ausbreiten, notwendig, um solche Projekte effizient zu entwickeln und unerwünschte Nebenwirkungen bestmöglich zu vermeiden.

Momentan wird zudem erwogen, Endlager für radioaktiven Abfall mit Hilfe akustischer Übertragung seismischer Signale zu überwachen. Hierfür ist ein optimaler Wissensstand, über den Einfluss der Heterogenität des Materials und wie diese die seismischen Wellen beeinflusst, notwendig, um die gesammelten Signale korrekt zu interpretieren.

Die zugrundeliegende Physik der geologischen Prozesse, kann durch die Gesetze der Physik und die konstitutiven Beziehungen der Materialien, die durch einen Satz partieller Differentialgleichungen abgeleitet werden, angenähert werden. Jedoch hängt deren Komplexität stark von dem verwendeten physikalis-

chen Modell und der Rheologie der zu modellierenden Materialien ab. Da die maßgebenden Gleichungen in den meisten Fällen nicht analytisch lösbar sind, sind effiziente numerische Methoden und Software erforderlich, um die genannten Probleme realitätsnah zu simulieren.

Durch eine Zusammenfassung aktueller Theorien, präsentieren wir in dieser Arbeit ein allgemeines mathematisches Model, welches die Physik poro-visko-elasto-plastischer geologischer Materialien beschreibt.

Zum Einen stellen wir einen, massiv-parallelen 3D Code vor, um Fluid Injektionen und Rissausbreitung in poro-visko-elasto-plastischen Rheologien zu modellieren. Mit Diesem können wir bestehende 2D Benchmark-Tests reproduzieren und einige Beispiele in 3D vorstellen. Die Resultate zeigen den Einfluss der initialen Spannungsbedingungen auf die Entwicklung von Schwächezonen und erlauben eine Generalisierung von, durch lokalen Porendruckanstieg ausgelösten, Schwächemustern. Weiterhin haben wir Simulationen hydraulischer Frakturierung für Well KM-8, UK, durchgeführt, die den signifikanten Einfluss von Gesteinspermeabilität und dessen Änderungen nach der Frakturierung auf die Entwicklung des Versagensbereiches, anzeigen.

Zum Anderen nutzen wir die Wellenausbreitungs-Software Sofi2D zur Simulation seismischer Beobachtungen eines tiefen, runden, verfüllten Tunnels, um unser Verständnis von Pfadeffekten zu verbessern und dadurch auf die Situation in Lagern radioaktiven Abfalls rückschließen zu können. Wir wenden unsere Resultate auf das Full-Scale Emplacement Experiment des Mont Terri Untergrund-Felslabors an.

Contents

List of Figures

List of Tables

List of Symbols

i, j	coordinates indexes
x_i	spatial coordinates
t	time
δ_{ij}	Kronecker delta function
D/Dt	material derivative with respect to time
$\hat{D}/Dt$	Jaumann derivative with respect to time
u_i	skeleton displacement
v_i	skeleton velocity
q_i	Darcy's velocity
T	temperature
g_i	gravity acceleration
H	volumetric heat source
H_l	liquid source
ε_{ij}	strain tensor
$\dot{\varepsilon}_{ij}$	strain rate tensor
θ	volumetric strain or dilation
$\dot{\varepsilon}_v$	volumetric strain rate
$\dot{\varepsilon}'_{ij}$	deviatoric strain rate tensor
$\dot{\varepsilon}_{II}$	second invariant of the deviatoric strain rate
$\dot{\varepsilon}^{pe}_{ij}$	poro-elastic component of the deviatoric strain rate
$\dot{\varepsilon}^{vs}_{ij}$	viscous component of the deviatoric strain rate
$\dot{\varepsilon}^{pl}_{ij}$	plastic component of the deviatoric strain rate
$\dot{\varepsilon}^{pl}_{II}$	rate of plastic distortion

$\dot{\varepsilon}_v^{pl}$	plastic volumetric strain rate
$\dot{\varepsilon}_{II}^{vs}$	second invariant of the viscous deviatoric strain rate
σ_{ij}	total Cauchy stress tensor
σ_{ij}^{eff}	effective stress tensor
P	pressure or mean normal stress
P_{eff}	mean effective stress or effective pressure
P_l	liquid pore-pressure
τ_{ij}	deviatoric stress rate tensor
τ_{II}	second invariant of the deviatoric stress rate
τ_{yield}	yield stress
Q	plastic flow potential
α	Biot-Willis coefficient
α_T	thermal expansion coefficient
λ_T	thermal conductivity
C_p	specific heat
ρ	density
η^*	effective viscosity
G	Shear modulus
ν	Poison's ratio
K	bulk modulus
λ	Lame's constant
C	cohesion
ϕ	friction angle
ψ	dilation angle
σ_T	tensile strength
μ	viscosity
k	permeability
μ	viscosity of the liquid
ρ_l	density of the liquid
S_s	specific storage
ϕ_l	effective porosity
α_l	matrix compressibility
β_l	liquid compressibility

Chapter 1

Introduction

1.1 Motivation

The high energetic demand in recent times has led us to explore new energy procurement techniques. For example, in the mid-twentieth century, hydraulic fracturing began to be used to enhance oil reservoirs (Clark et al. (1949)) and nuclear industries start to develop around the world (Munn (1979)). However, while earthquakes or contamination of aquifers can occur by using hydrofracturing techniques (e.g., Osborn et al. (2011), Vengosh et al. (2013), Cesca et al. (2014)), nuclear energy generates highly radioactive waste that could be stored in repositories below the surface (Apted & Ahn (2017), Müller et al. (2018)). Consequently, the geological processes involved in such issues must be investigated as thoroughly as possible in order to increase efficiency and decrease the risk of undesired side effects.

Enhancing geothermal systems or gas reservoirs by injecting fluid at high pressure to increase the natural permeability of the rocks and, thus, improve the productivity of the system is a potential way to obtain the necessary energy to meet our current needs. But exploitation of projects is expensive and, in addition, if it is not carried out safely, undesired side effects may occur (e.g., Lukawski et al. (2014), Majer et al. (2007), Nur (1971), Mignan et al.

(2015)). Therefore, increasing our understanding about how these actions influence and are affected by the local stress state of the reservoir and how fractures propagate through it is required.

On the other hand, one of the proposed solutions for radioactive waste management is placing it in repositories below the surface to minimize releases of the contained radioactivity into the environment (e.g., Gens et al. (2002), Seiphoori (2014), Siegesmund et al. (2014), Bohlen et al. (2015), Biryukov et al. (2016), Apted & Ahn (2017), Bossart (2017)). For this purpose, full-scale emplacements tests are being conducted to simulate such scenario (e.g., Müller et al. (2018)), and, to not compromise the sealing of the site, emission of seismic signals is used to monitor their internal state (e.g., E Manukyan (2012)). Hence, improve our understanding of path effect is crucial for a correct interpretation of the collected signals.

In all cases, the numerical modelling is a key means of inferring the subsurface response to potential scenarios as well as an aid to the analyses of field data and validation of conceptual hypothesis.

Nevertheless, as the rheology of rocks is complex and non-linear and, in most cases, the physics involving these processes are not amenable to analytical solutions, efficient numerical methods and software are required to simulate realistic problems.

Motivated by this requirement, the aim of this thesis is to provide some advances in numerical modelling to simulate these two current issues, the hydrofracturing and the seismic monitoring of a radioactive waste repository.

1.2 Methodology

Following current theories and models (e.g. Biot & Willis (1957), Murrell (1964), Vermeer & De Borst (1984), Skempton (1984), Paterson & Wong (2005), Moresi et al. (2007), Gerya (2009), Abeyartne (2012), Simpson (2017)), we build, in the context of continuous mechanics, a general poro-visco-elasto-

plastic numerical model governing geomechanical processes as hydrofracturing or seismic wave propagation . Then, we create, by improving the capabilities of the software LaMEM (Kaus et al. (2016)), a new software tool to simulate fluid injection and crack propagation in poro-visco-elasto-plastic rheologies and we use it to perform some simulations. Finally, we use the software tool SOFI2D (Bohlen et al. (2015)), which was created by other authors to simulate seismic wave propagation in visco-elastic setups (Bohlen (2002)), to build a 2D model of a cylindrical tunnel below the surface. Both software tools face the differential equations by staggered grid finite differences methods (Harlow & Welch (1965)) and use parallel computing techniques.

1.3 Structure

Chapter 2. Numerical approach

In this chapter, we present first the general mathematical model describing geomechanical processes such as fluid injection or wave propagation in poro-visco-elasto-plastic rheologies. To do that, we do a recompilation coming up from other authors of the basic ideas of continuous mechanics and we define the mathematical magnitudes describing such processes, the involved laws of physics and the constitutive relation of materials. Next, we present LaMEM and SOFI2D, the software tools used for the simulations in chapters 3, 4 and 5.

Chapter 3. 3D numerical simulation of fluid injection and crack propagation in geological media with complex rheologies

Here, we present the new computational massively-parallel 3D code to model fluid injection and crack propagation in poro-visco-elasto-plastic rheologies. We reproduce existing 2D benchmarks and give some examples of 3D cases.

The results show the importance of the initial stress conditions on the development of failure zones and give a generalization of failure patterns generated from a local increase of pore pressure.

Chapter 4. Numerical simulation of hydraulic fracture for Well KM-8

To better understand the influence of the material permeability on the development of failure zones, we use the software LaMEM to simulate the hydraulic stimulation of Well KM-8, located in PL080, North Yorkshire, UK. To perform the simulations, we consider different values for initial permeability of rocks and different values for permeability after failure occurs. Results show the importance of the knowledge of these parameters at the time to develop hydrofracturing projects.

Chapter 5. Numerical simulation of seismic monitoring of a radioactive waste repository

We use the viscoelastic forward modelling code SOFI2D to perform numerical simulations to investigate seismic wave propagation inside a cylindrical tunnel with the aim of increasing our ability to understand path effects and, therefore, to understand the situation inside a radioactive waste repository over time. We apply our results on the Full-Scale Emplacement Experiment at the Mont Terri underground rock laboratory.

Chapter 2

Numerical approach

2.1 Introduction

We present a general model for a fully saturated poro-visco-elasto-plastic porous medium. We do that by a recompilation of the basic ideas of continuous mechanics and poro-elasticity, defining the physical magnitudes, the involved laws of physics and the constitutive relation of materials describing such processes (e.g. Biot & Willis (1957), Murrell (1964), Vermeer & De Borst (1984), Skempton (1984), Paterson & Wong (2005), Moresi et al. (2007), Gerya (2009), Abeyartne (2012), Simpson (2017)). Next, we present two software tools that implement particular cases of the general physical model. LaMEM, implementing geomechanical deformation, and SOFI2D, implementing the elastodynamic equations.

2.2 Physical model

Continuum mechanics is commonly used to define a unified mathematical model to study the macroscopic behavior of a geological medium composed by solid and fluid materials, especially its motion and deformation under the action of forces and temperature variations.

Such an approach conceives the matter as an infinite set of particles filling everything assuming that physical magnitudes do not depend on any coordinate system and that the fields of interest are at least weakly differentiable.

That allows us to use tensorial and infinitesimal calculus to describe the medium and its changes through continuous and differentiable functions derived from the constitutive relations, characterizing the properties of a material, and from the principles of continuity of mass, momentum and energy.

2.2.1 Basic notions

Under the context of continuum mechanics, we assume the medium to be modelled mapped in a Cartesian coordinate system and, as notation, we adopt Einstein summation convention, indicating i and j coordinates indexes and x_i and x_j spatial coordinates. Vectors, $v = \sum_i v_i e_i$, are represented by v_i and two-second order tensors, $T = \sum_{ij} T_{ij} e_i \otimes e_j$, by T_{ij}, being $\{e_i, i = 1, 2, 3\}$ the basis of the chosen reference system. The identity matrix is denoted with the Kronecker delta function, δ_{ij}, defined as $\delta_{ij} = 1$ if i is equal to j and $\delta_{ij} = 0$ otherwise, and the material derivative with respect to the time of the vector v_i is notated by Dv_i/Dt.

To present the equations governing a poro-visco-elasto-plastic model we consider a representative part of the system assumed to be composed by a homogeneous visco-elasto-plastic skeleton poro-saturated with a liquid, where both phases coexist.

For the skeleton, the displacements of its particles are represented by vectors, u_i, and the velocities are defined by the derivatives with respect to time, t,

$$v_i = \frac{\partial u_i}{\partial t}. \tag{2.1}$$

The amount of deformation is done by the strain tensor, ε_{ij}, which, for small deformations, is related with the gradient of the displacements as

$$\varepsilon_{ij} = \frac{1}{2}\left(\frac{\partial u_i}{\partial x_j} + \frac{\partial u_j}{\partial x_i}\right). \tag{2.2}$$

Its first invariant represents the volume change, or dilation, and is given by

$$\theta = \varepsilon_{kk} = \frac{\partial u_i}{\partial x_i}. \tag{2.3}$$

The rate at which the displacements of particles change with time is represented by the strain rate tensor,

$$\dot{\varepsilon}_{ij} = \frac{1}{2}\left(\frac{\partial v_i}{\partial x_j} + \frac{\partial v_j}{\partial x_i}\right), \tag{2.4}$$

which can be decomposed into a volumetric and a deviatoric part.

The volumetric part is given by the first invariant,

$$\dot{\varepsilon}_v = \dot{\varepsilon}_{kk} = \frac{\partial v_i}{\partial x_i}, \tag{2.5}$$

which is called volumetric strain rate or rate of cubical dilatation responsible for irreversible inelastic volume changes such a due to dilatation, compactation or phase transformation, and, for poro-visco-elasto-plastic rheologies, can be expressed by a poro-elastic, a viscous and a poro-plastic component,

$$\varepsilon_{kk} = \varepsilon_v^{pe} + \varepsilon_v^{vs} + \varepsilon_v^{pl}. \tag{2.6}$$

The deviatoric part is given by

$$\dot{\varepsilon}_{ij}^{'} = \dot{\varepsilon}_{ij} - \frac{1}{3}\dot{\varepsilon}_{kk}\delta_{ij} \tag{2.7}$$

and can by expressed as well by the poroelasto-visco-plastic decomposition

$$\varepsilon_{ij}^{'} = \varepsilon_{ij}^{pe} + \varepsilon_{ij}^{vs} + \varepsilon_{ij}^{pl}. \tag{2.8}$$

The second invariant of the deviatoric strain rate tensor is defined as

$$\dot{\varepsilon}_{II} = \left(\frac{1}{2}\dot{\varepsilon}_{ij}^{'}\dot{\varepsilon}_{ij}^{'}\right)^{\frac{1}{2}}, \tag{2.9}$$

and second invariant for ε_{ij}^{pe}, ε_{ij}^{vs} and ε_{ij}^{pl} are defined in the same way.

On the other hand, the distribution of forces acting at any point in the parcel is described by the total Cauchy stress tensor, σ_{ij}. Theory of poroelasticity

(e.g., Biot & Willis (1957), Paterson & Wong (2005)) states that part of this stress is transmitted to the skeleton and another part is transmitted to the pore liquid, arising, from the principle of effective stress, the decomposition

$$\sigma_{ij} = \sigma_{ij}^{eff} - \alpha P_l \delta_{ij}, \tag{2.10}$$

where σ_{ij}^{eff} is the effective stress, responsible of skeleton deformation, P_l is the liquid pore-pressure and α is the Biot-Willis coefficient giving a relation between pore and bulk volumetric changes.

We define pressure or mean normal stress as

$$P_{total} = -\frac{\sigma_{kk}}{3}, \tag{2.11}$$

what allows us to express the deviatoric stress rate tensor as

$$\tau_{ij} = \sigma_{ij} + P_{total}\delta_{ij}, \tag{2.12}$$

which second invariant is defined as

$$\tau_{II} = \left(\frac{1}{2}\tau_{ij}\tau_{ij}\right)^{\frac{1}{2}}. \tag{2.13}$$

The effective pressure acting on the solid matrix and causing volumetric deformation can be expressed as

$$P = P_{total} - \alpha P_l, \tag{2.14}$$

while, for plasticity formulations, where $\alpha = 1$ can be considered (Skempton (1984), Lade & De Boer (1997), Paterson & Wong (2005)), the mean effective stress or effective pressure of the system is defined as

$$P_{eff} = P_{total} - P_l \tag{2.15}$$

We remark that we assume that, under compression, stresses are negative and pressure is positive.

2.2.2 Balance equations

The continuity equation states that the changes in the amount of an intensive property L (i.e. a property which is independent of the amount of material) are due to how much this quantity flows out through a volume boundary and how much changes due to sources or sinks Q inside the boundary. It is coming from the Reynold's transport and the divergence theorems and can be expressed as

$$\frac{DL}{Dt} + \frac{\partial \cdot (Lv)}{\partial x_i} + Q = 0. \tag{2.16}$$

Mass conservation equation - Volumetric deformation

The continuity equation applied to the material property density, and assuming that there are not sources or sinks of mass, leads to the mass conservation equation describing volumetric changes,

$$-\frac{1}{\rho}\frac{D\rho}{Dt} = \frac{\partial v_i}{\partial x_i}, \tag{2.17}$$

that, in terms of pressure (P), temperature (T), and plastic volumetric strain rate ($\dot{\varepsilon}_v^p$), can be expressed as

$$-\frac{1}{K}\frac{DP}{Dt} + \alpha_T \frac{DT}{Dt} + \dot{\varepsilon}_v^p = \frac{\partial v_i}{\partial x_i}, \tag{2.18}$$

where K is the bulk modulus and α_T is the thermal expansion coefficient.

Please note that, as defined above, P is the effective pressure acting on the solid matrix causing volumetric deformation and it is not equal to P_{eff} as soon as $\alpha \neq 1$.

In the same way, if q_i represents the liquid velocity vector determined by the Darcy's law as

$$q_i = -\frac{k}{\mu}\left(\frac{\partial P_l}{\partial x_i} - \rho_l g_i\right), \tag{2.19}$$

where k is the permeability, μ is the liquid viscosity, ρ_l is the liquid density and g_i is the gravity acceleration vector, the continuity equation for the pore liquid can be expressed as

$$S_s \frac{DP_l}{Dt} = -\frac{\partial q_i}{\partial x_i} + H_l, \tag{2.20}$$

being S_s the specific storage defined as

$$S_s = \alpha_l + \phi_l \beta_l, \tag{2.21}$$

where ϕ_l is the effective porosity and α_l and β_l are the matrix and liquid compressibility, respectively, and H_l is a possible liquid source.

Momentum conservation equation

From the continuity equation applied to the vector quantity momentum, arises the momentum conservation equation giving the balance of forces that act in the system

$$\frac{\partial \sigma_{ij}}{\partial x_j} + f_i = \rho \frac{Dv_i}{Dt} \tag{2.22}$$

which, combined with the equation 2.10 and 2.12, it can be expressed as

$$\frac{\partial \tau_{ij}}{\partial x_j} - \frac{\partial (P + \alpha P_l)}{\partial x_i} + f_i = \rho \frac{Dv_i}{Dt}, \tag{2.23}$$

representing the coupling equation between the skeleton and the pore liquid.

The term on the right in the equation represents inertial forces, which are important for wave propagation but negligible when modelling quasi static deformation. In the left, f_i represents body forces such as due to gravity acceleration or seismic sources (S),

$$f_i = \rho g_i + S_i. \tag{2.24}$$

Energy conservation equation

The thermal equation is also derived from applying the continuity equation 2.16 to the energy, resulting in

$$\frac{\partial}{\partial x_i}\left(\lambda_T \frac{\partial T}{\partial x_i}\right) + H = \rho C_p \frac{DT}{Dt}, \tag{2.25}$$

where T is the temperature, λ_T is the thermal conductivity, C_p is the specific heat and H is a volumetric heat source that includes the shear heating controlled by efficiency parameter $0 \leq \xi \leq 1$ and the radiogenic heat (A)

$$H = \xi \tau_{ij}(\dot{\varepsilon}_{ij} - \dot{\varepsilon}_{ij}^{el}) + \rho A. \tag{2.26}$$

2.2.3 Constitutive relations - Deviatoric deformation

The relation between strain and stress determines the state of the system and is a characteristic of the properties of the medium. The volumetric constitutive stress-strain relation is already described in last section and is manifested by equation 2.18. The constitutive effective stress-strain relation describing deviatoric changes can be expressed by

$$\tau_{ij} = 2\eta^* \dot{\varepsilon}_{ij}^{'}, \tag{2.27}$$

where η^* denotes the effective viscosity of the system.

As we said before, the deviatoric strain rate can be decomposed into a poroelastic, a viscous and a plastic component as

$$\dot{\varepsilon}_{ij}^{'} = \dot{\varepsilon}_{ij}^{pe} + \dot{\varepsilon}_{ij}^{vs} + \dot{\varepsilon}_{ij}^{pl}, \tag{2.28}$$

therefore, a stress-strain relationship for each component must be defined.

For elastic media, the effective stress-strain relationship is given from a generalization of Hooke's law as

$$\frac{\hat{D}\sigma_{ij}^{eff}}{Dt} = \lambda \delta_{ij} \dot{\varepsilon}_{kk}^{pe} + 2G\dot{\varepsilon}_{ij}^{pe}, \tag{2.29}$$

where λ and G are the Lame's constants related with the bulk modulus by

$$\lambda = K - \frac{2}{3}G \tag{2.30}$$

and $\hat{D}/Dt$ stands for the objective time derivative of the stress tensor.

The normal part of equation 2.29 is already contemplated in equation 2.18 and the deviatoric part gives the poro-elastic component of the deviatoric strain rate

$$\dot{\varepsilon}_{ij}^{pe} = \frac{1}{2G}\frac{\hat{D}\tau_{ij}}{Dt}. \tag{2.31}$$

In this equation $\hat{D}/Dt$ denotes the Jaumann specific implementation of the objective stress rate, given by

$$\frac{\hat{D}\tau_{ij}}{Dt} = \frac{\partial \tau_{ij}}{\partial t} + \tau_{ij}\omega_{kj} - \omega_{ik}\tau_{kj}, \tag{2.32}$$

where

$$\omega_{ij} = \frac{1}{2}\left(\frac{\partial v_i}{\partial x_j} - \frac{\partial v_j}{\partial x_i}\right) \tag{2.33}$$

is the spin tensor.

The viscous component of the deviatoric strain rate is coming from the Newtonian law of viscous friction and is defined as

$$\dot{\varepsilon}_{ij}^{vs} = (\dot{\varepsilon}_l + \dot{\varepsilon}_n)\frac{\tau_{ij}}{\tau_{II}}, \tag{2.34}$$

where

$$\dot{\varepsilon}_l = A_l \tau_{II} \tag{2.35}$$

and

$$\dot{\varepsilon}_n = A_n (\tau_{II})^n \tag{2.36}$$

are the diffusion and the dislocation components of the viscous creep strain rate, respectively, being n the stress exponent of the dislocation creep and A_l and A_n the exponential factors for each creep mechanism,

$$A_l = B_l \exp\left[-\frac{E_l + PV_l}{RT}\right] \tag{2.37}$$

and

$$A_n = B_n \exp\left[-\frac{E_n + PV_n}{RT}\right] \tag{2.38}$$

and B, E and V denote the creep constant, the activation energy and the activation volume for the corresponding mechanism and R the gas constant. Its second invariant is defined as

$$\dot{\varepsilon}_{II}^{vs} = \left(\frac{1}{2}\dot{\varepsilon}_{ij}^{vs}\dot{\varepsilon}_{ij}^{vs}\right)^{\frac{1}{2}}. \tag{2.39}$$

The poro-plastic component of the deviatoric strain rate comes up from the assumption that a limit for rock stresses exists (τ_{yield}) and, once is reached, a plastic failure occurs defined by a plastic flow potential Q as

$$\dot{\varepsilon}_{ij}^{pl} = \dot{\gamma}\frac{\partial Q}{\partial \sigma_{ij}^{eff}}, \tag{2.40}$$

where $\dot{\gamma}$ is the plastic multiplier satisfying the yield condition

$$\tau_{II} = \tau_{yield}. \tag{2.41}$$

As yield criteria, we adopt a combination between the yield criteria for shear failure proposed by Paterson & Wong (2005) and the yield criteria for tensile failure proposed by Murrell (1964),

$$\tau_{yield} = \min\left(P_{eff}\sin\phi + C\cos(\phi), P_{eff} + \sigma_T\right), \tag{2.42}$$

where C is the cohesion, ϕ is the friction angle, σ_T is the tensile strength and P_{eff} is the mean effective stress or effective pressure defined in equation 3.2. This criteria is graphically expressed in figure 2.1.

Defining the plastic potential function as follow

$$Q \;=\; \tau_{II} - P_{eff}\sin(\psi) \tag{2.43}$$

(Vermeer & De Borst (1984), Moresi et al. (2007)), where ψ is the dilation angle of the material, the relation between the plastic volumetric strain rate

and the rate of plastic distortion (Vermeer & De Borst (1984)) can be expressed as

$$\dot{\varepsilon}_v^{pl} = 2\sin(\psi)\dot{\varepsilon}_{II}^{pl}, \tag{2.44}$$

where

$$\dot{\varepsilon}_v^{pl} = \dot{\varepsilon}_{kk}^{pl} \tag{2.45}$$

and

$$\dot{\varepsilon}_{II}^{pl} = \left(\frac{1}{2}\dot{\varepsilon}_{ij}^{pl}\dot{\varepsilon}_{ij}^{pl}\right)^{\frac{1}{2}} \tag{2.46}$$

are the first and second invariant of the plastic strain rate, respectively.

2.3 LaMEM

We aim to build a software tool to model fluid injection and crack propagation in a poro-visco-elasto-plastic medium defined by the properties density (ρ), bulk modulus (K), shear modulus (G), cohesion (C), friction (ϕ) and dilation (ψ) angles, thermal conductivity (λ_T), specific heat (C_p), thermal expansion coefficient (α_T), Biot-Willis coefficient (α), permeability (k), liquid viscosity (μ), liquid density (ρ_l) and specific storage (S_s).

From equations presented in previous section, the governing equations of this system can be summarized as

$$-\frac{1}{K}\frac{DP}{Dt} + \alpha_T\frac{DT}{Dt} + 2\sin(\psi)\dot{\varepsilon}_{II}^{pl} = \frac{\partial v_i}{\partial x_i}, \tag{2.47}$$

$$\frac{\partial \tau_{ij}}{\partial x_j} - \frac{\partial(P+\alpha P_l)}{\partial x_i} + \rho g_i = 0, \tag{2.48}$$

$$\frac{\partial}{\partial x_i}\left(\lambda_T\frac{\partial T}{\partial x_i}\right) + H = \rho C_p\frac{DT}{Dt}, \tag{2.49}$$

$$\frac{\partial}{\partial x_i}\left(\frac{k}{\mu}\left(\frac{\partial P_l}{\partial x_i} - \rho_l g_i\right)\right) + H_l = S_s\frac{DP_l}{Dt}, \tag{2.50}$$

$$\dot{\varepsilon}_{ij}^{'} = \frac{1}{2G}\frac{\hat{D}\tau_{ij}}{Dt} + \dot{\varepsilon}_{II}^{vs}\frac{\tau_{ij}}{\tau_{II}} + \dot{\varepsilon}_{II}^{pl}\frac{\tau_{ij}}{\tau_{II}}, \tag{2.51}$$

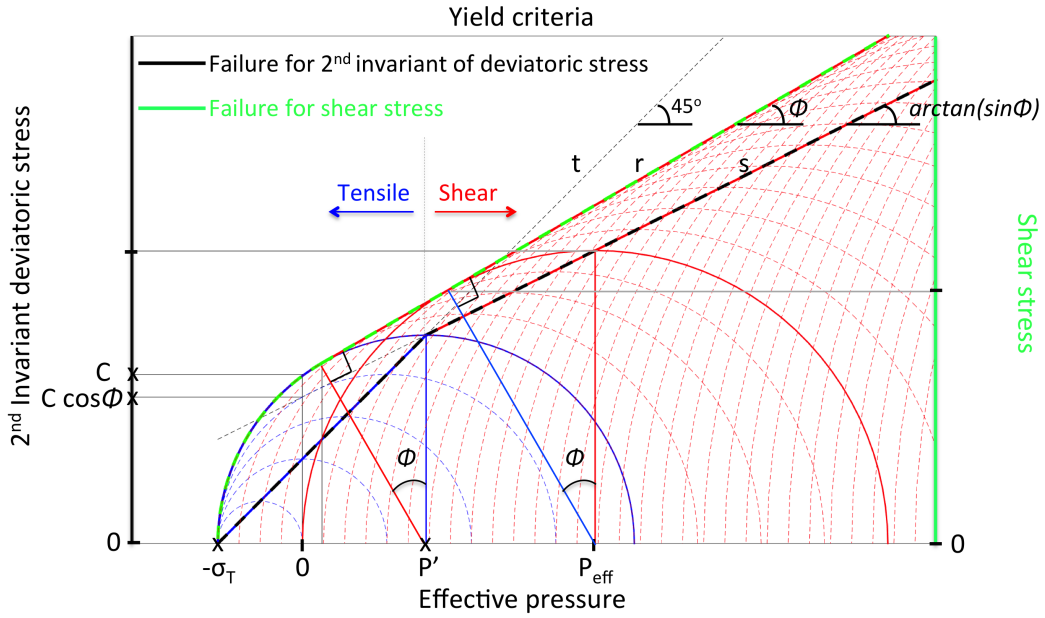

Figure 2.1: The yield criteria for the second invariant of the deviatoric stress considered for plastic failure in equation 3.3 is plotted as dashed black line. $P^{'}$ indicates the effective pressure corresponding to the intersection between the line $t : P_{eff} + \sigma_T$, that forms an angle of 45^o with respect to the horizontal axis, and the line $s : P_{eff} \sin\phi + C\cos(\phi)$, with an angle of $\arctan(\sin(\phi))$. Its analytical value is $P^{'} = (\sigma_T - C\cos\phi)/(\sin\phi - 1)$. On the other hand, the set of all the semicircles with center P_{eff} and radius $\tau_{yield}(P_{eff})$, plotted in blue for tensile and in read for shear, defines the yield criteria for shear stress and is given by a combination between the semicircle corresponding to $P^{'}$ (in red) and the line $r : P_{eff}\tan\phi + C$ with angle ϕ. Such envelope is plotted as a dashed green line.

where v_i is the velocity, τ_{ij} and $\dot{\varepsilon}^{'}_{ij}$ are the deviatoric stress and strain rate, respectively, P is the pressure, P_l is the liquid pressure, T is the temperature, g_i is the gravity acceleration vector, H is a heat source from shear and radiogenic heating (equation 2.26), H_l is a liquid source from injection, τ_{II}, $\dot{\epsilon}^{vs}_{II}$ and $\dot{\epsilon}^{pl}_{II}$ are the second invariant of the deviatoric stress (2.13), deviatoric viscous strain (2.39) and deviatoric plastic strain rate (2.46), respectively, and D/Dt and $\hat{D}/Dt$ are the material and the Jaumann (equation 2.32) derivative with respect to time, respectively.

Equation 2.47 are the mass conservation equation and arises by substituting equation 2.44 in equation 2.18, while equation 2.48 describes the conservation

of momentum and is coming by neglecting inertial and non-gravity terms in equation 2.23. The energy conservation equation 2.49 comes up directly from expression 2.25. The mass conservation equation for liquids (equation 2.20) combined with the Darcy's law (equation 2.19) gives the formula 2.50.

Finally, equation 2.51 describes the poro-visco-elasto-plastic constitutive relation and arises from equations 2.54, 2.31, 2.34, and 2.40 and 2.44.

LaMEM[1] (Lithosphere and Mantle Evolution Model) (Kaus et al. (2016)) is a scalable 3D parallel code which, initially, was developed to simulate geological processes such as lithosphere deformation (e.g. Schmeling et al. (2008), Lechmann et al. (2014), Pusok & Kaus (2015), Collignon et al. (2016)).

As explained by Kaus et al. (2016), the conservation equations are discretized in space by using the staggered grid finite difference method (Harlow & Welch (1965)) and, to achieve scalability on massively parallel machines, LaMEM uses the distributed arrays (DMDA) and iterative solvers (KSP, SNES) from the PETSc library (Balay et al. (2018)). The free surface is implemented using a so-called sticky air approach, which assigns a relative low but nonzero viscosity to the air phase, together with an appropriate stabilization method to allow for sufficient large time steps (Kaus et al. (2010), Duretz et al. (2011)). The topography of the free surface is explicitly tracked by an internal 2D grid that covers the entire domain.

A Marker and Cell method (Harlow & Welch (1965)) is employed to track material properties, which are advected in an Eulerian kinematic framework. During advection, the elastic history stresses from previous time step (τ_{ij}^n) are corrected on the markers to account for the rigid-body rotation, and then interpolated on the edge and cell control volumes (figure 2.2) using the distance-based averaging (Duretz et al. (2011))

$$\tau_{ij}^* = \tau_{ij}^n + \triangle t(\omega_{ik}\tau_{kj}^n - \tau_{ik}^n\omega_{kj}), \tag{2.52}$$

[1]Package is available at https://bitbucket.org/bkaus/lamem

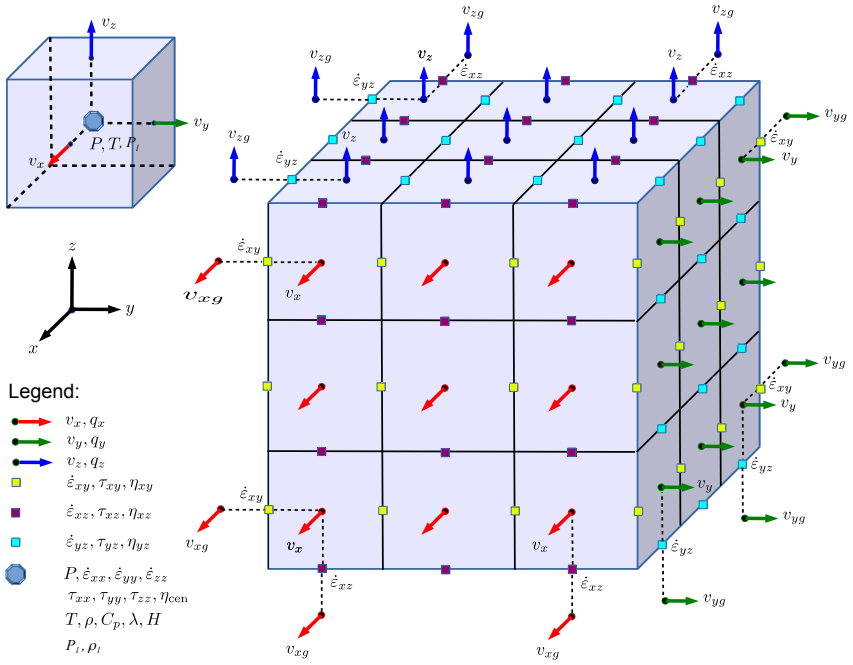

Figure 2.2: Staggered grid finite difference spatial discretization, illustrating how the variables are ordered. To implement Darcy's flow, liquid pressure (P_l) and density (ρ_l) has been included in the center of the cells.

to obtain the effective strain rates by

$$\dot{\varepsilon}^*_{ij} = \dot{\varepsilon}'_{ij} + \frac{\tau^*_{ij}}{2G\triangle t}. \tag{2.53}$$

The effective viscosity, giving the relation

$$\tau_{ij} = 2\eta^* \dot{\varepsilon}^*_{ij} \tag{2.54}$$

is computed by using the standard quasi-viscous expression,

$$\eta^* = \min\left[\left(\frac{1}{G\triangle t} + \frac{1}{\eta_l} + \frac{1}{\eta_n}\right)^{-1}, \frac{\tau_Y}{2\dot{\varepsilon}^*_{II}}\right], \tag{2.55}$$

where the individual creep viscosities are defined from the exponential factors for each creep mechanism (A_l and A_n) (equations 2.37 and 2.38) as

$$\eta_l = \frac{1}{2}(A_l)^{-1}, \eta_n = \frac{1}{2}(A_n)^{-\frac{1}{n}}(\dot{\varepsilon}^*_{II})^{\frac{1}{n}-1}. \tag{2.56}$$

2.3.1 Updates

We take advantage of LaMEM and follow the same methodology to implement Darcy flow and poro-elasto-plasticity.

Darcy flow

To describe the behaviour of the pressure arising from the liquid in porous materials we solve the equation 2.50. We do that, with a staggered grid finite differences discretization (Harlow & Welch (1965)) and iterative solvers (KSP) from PETSc library (Balay et al. (2018)).

Then, in order to coupled it with the stress of the structure, we use the resulting pore-pressure (P_l) on the momentum conservation equation 2.48.

Poro-elasto-plasticity

Volumetric deformation is improved by taking into account the volumetric plastic strain in the mass conservation equation 2.47, determined by the angle ψ (equation 2.44), which is the dilation angle of materials for shear failure (figure 2.3.1) or 90^o in case of tensile failure.

Furthermore, we complement plasticity by using the full yield criteria defined in expression 3.3 (figure 2.1), which includes tensile failure, one of the possible failure modes due to local pore-liquid increase and/or extensional forces (Vermeer & De Borst (1984), Gerya (2009)).

Effective-pressure dependency of material properties

To account for the effective-pressure dependency for permeability, porosity and Poison's ratio, we implemented the possibility to use drained values of such properties if the liquid pressure is hydrostatic, undrained values when effective pressure reaches the tensile strength and a linear function for intermediate values (David et al. (1994), Galvan & Miller (2013)).

On the other hand, while the deviatoric stresses are updated, in case of reaching the yield limit, by using the standard quasi-viscous expression (equation 2.55), an excess of effective pressure must be relieved by a change in the hydraulic properties of the materials (figure 2.4).

To account for that, we implemented as well the possibility to change, during the advection, the phase of materials if tensile and/or shear failure occur.

Mode in which failure occurs

In particular, this new code allows tracking areas where failure occurs and the type of mode, shear or tensile, by which this occurs.

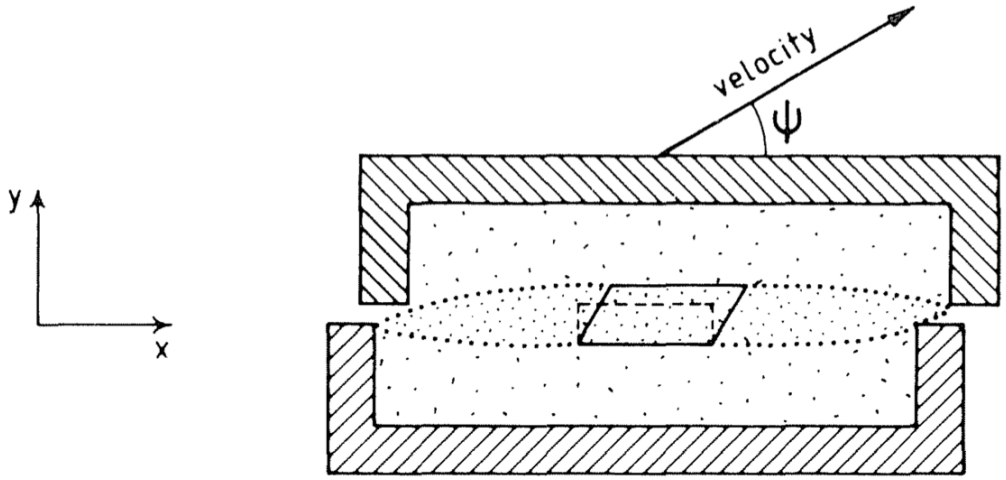

Figure 2.3: The model accounts for the dilation angle of shear bands (picture from Vermeer & De Borst (1984)).

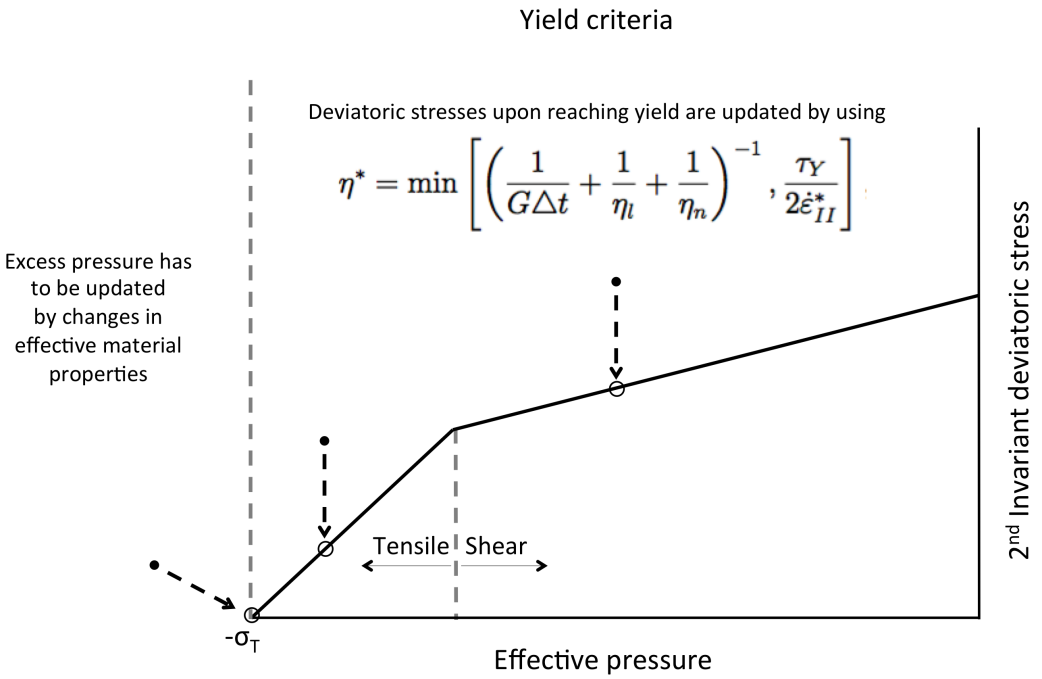

Figure 2.4: Scheme of the update of the deviatoric stresses and the effective pressure if yield stress is reached and the trial stress is outside the yield envelope.

2.3.2 Examples

Liquid pressure around a high permeability fault

As an example of Darcy's flow implementation, we reproduce the scenario proposed in Simpson (2017), where a 2D simulation of the influence of a high permeability fault zone into the crust is performed. For that, we used the model setup described in Figure 2.5 with a numerical resolution of $100 \times 2 \times 50$ and a time step of 0.1 years. The material parameters considered are $k_{crust} = 10^{-16}\ m^2$, $k_{fault} = 10^{-12}\ m^2$, $\mu_l = 1.33 \times 10^{-4}\ Pa$, $\beta_l = 10^{-10}\ Pa^{-1}$ and $\phi_l = 0.1$. Figure 2.3.2 shows the result 10 years after the fault was introduced, where colors are the liquid pressure and arrows shows the liquid flow directions.

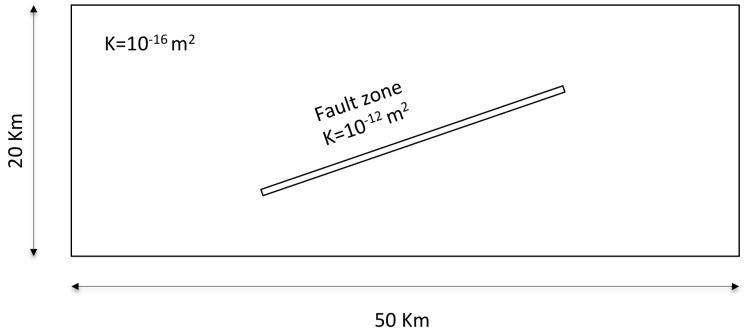

Figure 2.5: Setup for model of fluid flow around a high permeability fault zone.

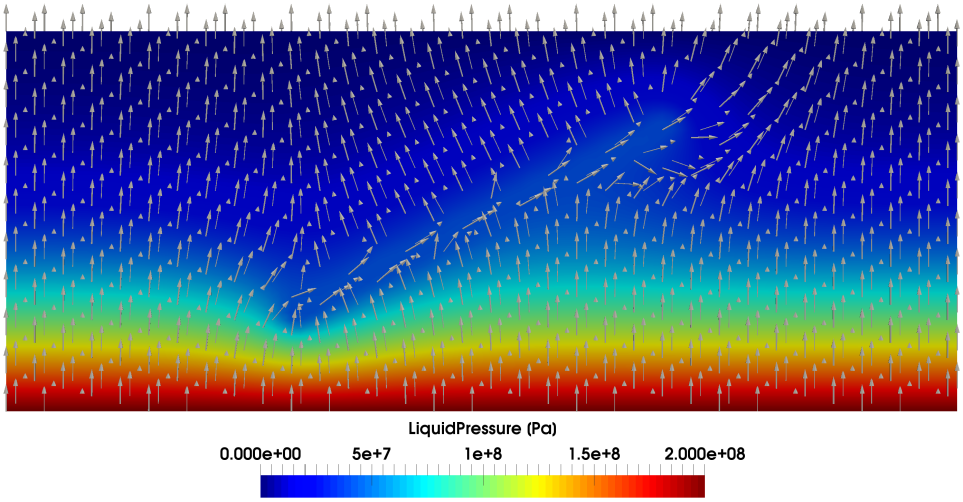

Figure 2.6: Simulation with LaMEM of liquid pressure change due to a high permeability fault zone.

Fluid injection and crack propagation

As a 3D example of fluid injection and crack propagation, we perform a simulation in a heterogeneous 3D setup defined by Figure 2.7 and Table 2.1. The model considered is 9 km long, 4 km wide and 3 km high and is composed by five layers and sectioned by a normal fault. We impose free surface at the top and free slip at the bottom and lateral boundaries, and, to simulate an extensional regime, we apply a constant background strain rate of 10^{-15} s^{-1} in the x direction. To simulate an injection/production system

of water heating we consider a positive fluid source in the point indicated by blue arrow and a negative source in the point indicated by red arrow in figure 2.8. To simulate hydrofracturing we apply in the three points marked by yellow arrows bigger source magnitudes to increase stress and produce fractures. Figure 2.8 shows the result of the simulation after 10000 seconds of simulation. On the left, we can observe the influence of the low-pressure fluid injection/extraction on the direction of flow, which, since fluids flows from high pressure to low pressure zones, is expected to be pointing upwards due to the extensional regime. On the right side, blue color indicates where yield stress is reached either by tensile or shear mode. The input file of this simulation is in Appendix 2.5.1.

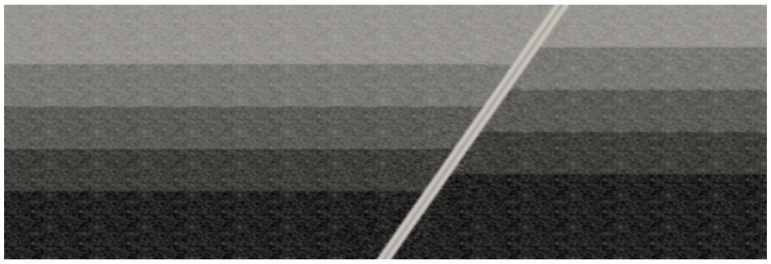

Figure 2.7: Section of the model setup used for the simulation.

Table 2.1: Material parameters employed for the simulation. Multiples values of density and permeability belong to layers from bottom to top, inner and external part of the fault, properties after failure and, the last one, corresponds to a random material that was mixed throughout the model. Source magnitude values correspond to those used for low-pressure injection, low-pressure extraction and high-pressure injection.

Variable	Parameter	Value	Units
ρ	Density	[2700,2600,2500,2500,2600,2700,2700,2700,2700]	kg m^{-3}
ρ_l	Liquid density	1000	kg m^{-3}
G	Shear module	$5x10^4$	MPa
ν	Poison's ratio	0.27	
C	Cohesion	40	MPa
ϕ	Friction angle	45	(°)
ψ	Dilation angle	45	(°)
σ_T	Tensile strength	20	MPa
k	Permeability	[10^{-16},10^{-40},10^{-5},10^{-11},10^{-8},10^{-30},10^{-14},10^{-15},10^{-20}]	m^2
S_s	Specific storage	10^{-4}	MPa^{-1}
H_m	Source magnitude	[$5x10^{-4}$,$5x10^{-4}$,10,10,10]	m^3s^{-1}

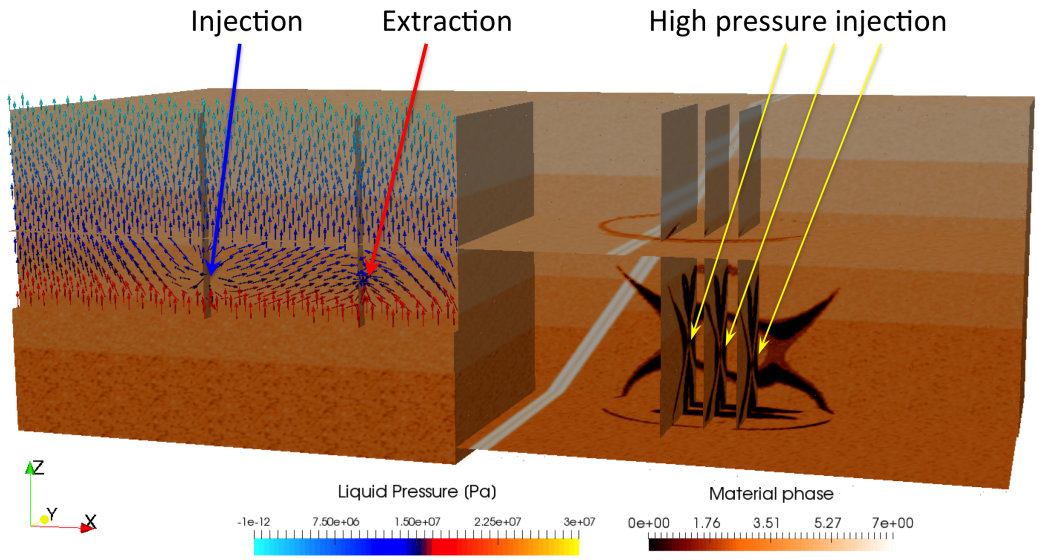

Figure 2.8: Simulation of fluid injection and crack propagation. Different brown colors in the model setup indicate different material properties. On the left side, vectors direction and color show the fluid velocity and fluid pressure, respectively. We can observe the influence of the low-pressure fluid injection/extraction on the direction of flow which is expected to be pointing upwards due to the extensional regime. On the right side, darkest brown color indicates where yield stress is reached by either tensile or shear mode.

2.3.3 Remarks

The resulting software tool[2] is aimed to facilitate the analyses of hydrofracturing projects, the validation or improvement of conceptual hypothesis and the assessment of the potential and the risk during the exploration phase. Nevertheless, it has further application in other fields of geodynamics and volcanology, helping to interpret focal mechanisms during volcanic eruptions, or induced seismicity.

However, a more realistic modelling of the stress dependence of the hydraulic properties as permeability and porosity, as well as a more accurately modelling of plasticity must be implemented.

2.4 SOFI2D

The elastodynamic equations describing seismic wave propagation in isotropic elastic medium are given from expressions 2.3, 2.4, 2.22 and 2.29 by neglecting pore-pressure and temperature changes. They can be summarized as

$$\rho \frac{\partial v_i}{\partial t} = \frac{\partial \sigma_{ij}}{\partial x_j} + f_i \tag{2.57}$$

$$\frac{\partial \sigma_{ij}}{\partial t} = \lambda \frac{\partial \theta}{\partial t} \delta_{ij} + 2\mu \frac{\partial \varepsilon_{ij}}{\partial t}, \tag{2.58}$$

$$\frac{\partial \varepsilon_{ij}}{\partial t} = \frac{1}{2} \left(\frac{\partial v_i}{\partial x_j} + \frac{\partial v_j}{\partial x_i} \right), \tag{2.59}$$

where t is time, v_i is the velocity vector, σ_{ij} and ε_{ij} are the stress and strain tensor, respectively, θ is dilation, ρ is density, λ and μ are the Lamé parameters and f_i are body forces due to gravity or seismic sources.

The software Sofi2D is a viscoelastic forward modelling code that solves these equations by using the finite differences method in a 2-D Cartesian standard staggered grid. Viscoelasticity is implemented by using the so-called rheological model "generalized standard linear solid" (Bohlen (2002), LiU et al.

[2]Package is available at https://bitbucket.org/bkaus/lamem branch "darcy_solver"

(1976)) and uses the message passing interface to distribute the calculations in parallel.

2.5 Appendix

2.5.1 Input file used in the 3D simulation

```
# Example of 3D simulation of fluid injection
# Commit version 'becfe8c' in https://bitbucket.org/bkaus/lamem/branch/darcy_solver

# Grid
nel_x =  512
nel_y =  128
nel_z =  256

# Geometry
W       = 9000    # Width  (x-direction)
H       = 3000    # Height (z-direction)
x_left  = -4500   # Left side of domain
y_front = 0       # Front side of domain
z_bot   = 0       # Bottom of box
L       = 4000    # Length (y-direction)

# Characteristic values
units                       = si
Characteristic.Length       = 1  # [m]
Characteristic.Viscosity    = 1  # [Pa.s]
Characteristic.Temperature  = 1  # [K]
Characteristic.Stress       = 1  # [Pa]

# Model setup
msetup = example3Dsetup

# Time stepping and output
OutputFile                  =   ExampleFluidInjection

save_timesteps              =   5           # save every ? timesteps
time_end                    =   100         # last timestep
CFL                         =   0.5         # CFL, dt-based criterium
dt_max                      =   5e2         # Maximum timestep

# Boundary conditions

BC.LeftBound    =   1   # 0 - free surface, 1-free slip with BG strainrate Eyy,
                        # 2 - no slip, 5 - growthrate 2D, 7 - growthrate 3D
BC.RightBound   =   1   # 0 - free surface, 1-free slip with BG strainrate Eyy,
                        # 2 - no slip, 5 - growthrate 2D, 7 - growthrate 3D
BC.FrontBound   =   1   # 0 - free surface, 1-free slip with BG strainrate Exx,
                        # 2 - no slip, 5 - growthrate 2D, 7 - growthrate 3D
BC.BackBound    =   1   # 0 - free surface, 1-free slip with BG strainrate Exx,
                        # 2 - no slip, 5 - growthrate 2D, 7 - growthrate 3D
BC.LowerBound   =   1   # 0 - free surface, 1-free slip,
                        # 2 - no slip, 5 - growthrate 2D, 7 - growthrate 3D
BC.UpperBound   =   0   # 0 - free surface, 1-free slip,
                        # 2 - no slip, 5 - growthrate 2D, 7 - growthrate 3D

Temp_top        =   0   # Temperature @ top
Temp_bottom     =   0   # Temperature @ bottom; side BC's are flux-free
Gravity         =  -10; # [m/s2] - gravitational acceleration
```

```
Gravity         =  -10; # [m/s2] - gravitational acceleration

# For Darcy's flow
Pl_top          =   0       # Liquid-pressure @ top
Pl_bottom       =   3e7     # Liquid-pressure @ bottom


# Define phase transitions for particles
LowerViscosityCutoff = 1e-30
UpperViscosityCutoff = 1e30
DII_ref              = 1

# Control parameters
#LowerViscosityCutoff   = 1e16
#UpperViscosityCutoff   = 1e27
#DII_ref                = 1e-15
FSSA                    = 1.0
InitViscosity           = 1e20

# Phase distribution
NumPartX                =   3   # Particles/Cell in x-direction
NumPartY                =   3   # Particles/Cell in y-direction
NumPartZ                =   3   # Particles/Cell in z-direction

#===============================================================================
# ............................. PETSc options.............................
#===============================================================================
<PetscOptionsStart>

    # matrix-free closed-form Jacobian if this is uncommented
    #-jac_mat_free
    #-out_jac_test 1
    -skip_press_shift
    -open_top_bound

    # Background strain rate
    -ExxNumPeriods  1
    -ExxStrainRates 1e-15
    #-EyyNumPeriods  1
    #-EyyStrainRates -1e-14

    -stress_min 1e+6   # put 1e0 if GEO
    -stress_sensitivity_for_failure 0   # [Pa if SI]

    #-ExplicitSolver 1

    # Time step (Myr)
    -dt 5e2 #3e-12 #0.0048

    # shear bands setup
    -H_layer                  1000
    -H_bottom                 40
    -Inclusion_use
    -Inclusion_size   80

    #-Inclusion_offset 10
    #-Inclusion_length 10

    # SNES (nonlinear) options
    #-snes_ksp_ew                   # Eisenstat Walker algorithm
    -snes_ksp_ew_rtolmax  1e-1
    -snes_monitor
    #-snes_atol 1e-9
    -snes_atol 1e-7
    -snes_rtol 1e-4
    -snes_stol 1e-16
    -snes_max_it 50
    -snes_max_funcs 500000
    -snes_max_linear_solve_fail 10000

    #-snes_type ksponly

    # Newton/picard options
    -snes_PicardSwitchToNewton_rtol 1e-1  # relative tolerance to switch to Newton (1e-2)
    -snes_NewtonSwitchToPicard_it   20    # number of Newton iterations after which
                                          # we switch back to Picard
    -snes_NewtonSwitchToPicard_rtol 1.1   # relative tolerance compared to first
                                          # iteration step

    # Linesearch options
```

```
-snes_linesearch_monitor
-snes_linesearch_type l2       # Linesearch type (one of) shell basic l2 bt cp
                        #(SNESLineSearchSetType)  [l2 seems to work better with VEP]
-snes_linesearch_maxstep 1.0   # very important to prevent the code from "blowing up"

# Jacobian solver
-js_ksp_type fgmres
-js_ksp_max_it 50
-js_ksp_converged_reason
-js_ksp_rtol 1e-10
-js_ksp_atol 1e-14

## Direct solver
#-pcmat_type mono
#-pcmat_pgamma 1e3
#-jp_type user
#-jp_pc_type lu
#-jp_pc_factor_mat_solver_package mumps

# Additional command-line Petsc Options
#-AddRandomNoiseParticles 0
-restart 0
-save_breakpoints 0
-objects_dump
-restart 0
#-SkipStokesSolver 1
#-SavePartitioning


# ###########################################################################################
#Stokes Preconditioner
-pstokes mg

# Matrix type
-pcmat_type mono                        # monolithic matrix [coupled MG solver]
-jp_type mg                             # multigrid

# Multigrid preconditioner settings
-gmg_pc_type mg
-gmg_pc_mg_levels 4                     # 5 MG levels, gives coarse grid of 32x16x8
-gmg_pc_mg_galerkin                     #
-gmg_pc_mg_type multiplicative
-gmg_pc_mg_cycle_type v
-gmg_pc_mg_log     # monitors time spend in multigrid if using -log_summary @ the end

# RICHARDSON/JACOBI MG Smoothener
-gmg_mg_levels_ksp_type richardson
-gmg_mg_levels_ksp_richardson_scale 0.6
-gmg_mg_levels_pc_type jacobi
-gmg_mg_levels_ksp_max_it 10

# DIRECT, REDUNDANT COARSE SOLVER
-crs_ksp_type preonly
-crs_pc_type redundant
-crs_pc_redundant_number 4     # split domain in 4 pieces so ever direct
solver step is done on 512 cores
-crs_redundant_pc_factor_mat_solver_package superlu_dist     # uses mumps as local
                                #   direct solver     [superlu_dist is another option]
###########################################################################################

# output information
-out_pvd 1
-out_phase 1
-out_density 1
-out_bulk 1
-out_viscosity 1
-out_velocity 1
-out_pressure 1
-out_temperature 1#
-out_dev_stress 1
-out_j2_dev_stress 1
-out_strain_rate 1
-out_j2_strain_rate 1
-out_plast_strain 1
-out_plast_strain 1
-out_moment_res 1
-out_cont_res 1
-out_yield 1
-out_shmax 1
# output Darcy parameters
```

```
    -out_Pl 1                       # fluid pressure
    -out_porosity 1                 # porosity
    -out_permeability 1             # permeability
    -out_liquiddensity 1    # liquid density
    -out_liquidvelocity 1   # liquid flow
    -out_failureT 1          # type of failure tensile
    -out_failureS 1          # type of failure shear
    -out_failureTS 1         # if pressure arrived to tensile strength

    -AVDPhaseViewer 0

    -actPorePres
     -biot 0.8
    # For Darcy's solver: ######################################################
    -act_darcy     # Activates Darcy solver
    -act_initialguess_hydro # Consider hydrostatic pressure as initial condition
    -darcy_ksp_type fgmres
    #-darcy_pc_type lu
    #-darcy_pc_factor_mat_solver_package mumps
    -darcy_ksp_monitor
    -darcy_ksp_max_it 500
    -darcy_ksp_converged_reason
    #-darcy_ksp_rtol 1e-20
    #-darcy_ksp_atol 1e-20
    ############################################################################

<PetscOptionsEnd>

#===============================================================================
# ........................... Material Parameters ............................
#===============================================================================
# Define properties of matrix -----------------
    <MaterialStart> // Phase after failure
        ID          =   0       # phase id  [-]
        rho0        =   2700    # density - if dimensional [kg/m3]
        shear       =   5e10    # shear modulus (mu, G)
        poison      =   0.27    # Poison's ratio
        dilation    =   45      # dilation angle (o)
        friction    =   45      # friction angle (o)
        cohesion    =   40e+6   # cohesion (Pa)
        # DARCY Parameters:
        rhol            = 1000    # liquid density [kg/m3]
        mul             = 1e-4    # liquid viscosity [Pa.s]
        Kphi            = 1e-15   # permeability [m2]
        TensileS        = -20e+6  # tensile strength [Pa]
        betam           = 1e-10   # matrix compressibility [Pa-1]
        betal           = 1e-12   # liquid compressibility [Pa-1]
        Phi             = 0.1     # porosity
        poisonu         = 0.27    # undrained poison ratio
        Kphiu           = 1e-15   # undrained permeability
        Phiu            = 0.1     # undrained porosity
    <MaterialEnd>
    <MaterialStart>    # Granite
        ID          =   1
        rho0        =   2700
        shear       =   5e10
        poison      =   0.27
        dilation    =   45
        friction    =   45
        cohesion    =   40e+6
        # DARCY Parameters:
        rhol            = 1000
        mul             = 1e-4
        Kphi            = 1e-16
        TensileS        = -20e+6
        betam           = 1e-10
        betal           = 1e-12
        Phi             = 0.03
        poisonu         = 0.27
        Kphiu           = 1e-16
        Phiu            = 0.03
    <MaterialEnd>
    <MaterialStart>  # impermeable sediments
        ID          =   2
        rho0        =   2600
        shear       =   5e10
        poison      =   0.27
        dilation    =   45
        friction    =   45
        cohesion    =   40e+6
```

```
    # DARCY Parameters:
    rhol            = 1000
    mul             = 1e-4
    Kphi            = 1e-40
    TensileS        = -20e+6
    betam           = 1e-10
    betal           = 1e-12
    Phi             = 0.001
    poisonu         = 0.27
    Kphiu           = 1e-40
    Phiu            = 0.001
<MaterialEnd>
<MaterialStart>  # aquifer
    ID          =   3
    rho0        =   2500
    shear       =   5e10
    poison      =   0.27
    dilation    =   45
    friction    =   45
    cohesion    =   40e+6
    # DARCY Parameters:
    rhol            = 1000
    mul             = 1e-4
    Kphi            = 1e-5
    TensileS        = -20e+6
    betam           = 1e-10
    betal           = 1e-12
    Phi             = 0.1
    poisonu         = 0.27
    Kphiu           = 1e-5
    Phiu            = 0.1
<MaterialEnd>
<MaterialStart>  # sandstone
    ID          =   4
    rho0        =   2500
    shear       =   5e10
    poison      =   0.27
    dilation    =   45
    friction    =   45
    cohesion    =   40e+6
    # DARCY Parameters:
    rhol            = 1000
    mul             = 1e-4
    Kphi            = 1e-11
    TensileS        = -20e+6
    betam           = 1e-10
    betal           = 1e-12
    Phi             = 0.08
    poisonu         = 0.27
    Kphiu           = 1e-11
    Phiu            = 0.08
<MaterialEnd>
<MaterialStart>  # sand
    ID          =   5
    rho0        =   2600
    shear       =   5e10
    poison      =   0.27
    dilation    =   35
    friction    =   10
    cohesion    =   20e+6
    # DARCY Parameters:
    rhol            = 1000
    mul             = 1e-4
    Kphi            = 1e-8
    TensileS        = -10e+6
    betam           = 1e-10
    betal           = 1e-12
    Phi             = 0.3
    poisonu         = 0.27
    Kphiu           = 1e-8
    Phiu            = 0.3
<MaterialEnd>
<MaterialStart>  # fault
    ID          =   6
    rho0        =   2700
    shear       =   5e10
    poison      =   0.27
    dilation    =   45
    friction    =   45
    cohesion    =   40e+6
```

```
        # DARCY Parameters:
        rhol            = 1000
        mul             = 1e-4
        Kphi            = 1e-30
        TensileS        = -20e+6
        betam           = 1e-10
        betal           = 1e-12
        Phi             = 0.003
        poisonu         = 0.27
        Kphiu           = 1e-30
        Phiu            = 0.003
    <MaterialEnd>
    <MaterialStart>  # damaged area of the fault
        ID          =   7
        rho0        =   2700
        shear       =   5e10
        poison      =   0.27
        dilation    =   45
        friction    =   45
        cohesion    =   40e+6
        # DARCY Parameters:
        rhol            = 1000
        mul             = 1e-4
        Kphi            = 1e-14
        TensileS        = -20e+6
        betam           = 1e-10
        betal           = 1e-12
        Phi             = 0.05
        poisonu         = 0.27
        Kphiu           = 1e-14
        Phiu            = 0.05
    <MaterialEnd>
    <MaterialStart>  # random phase
        ID          =   8
        rho0        =   2700
        shear       =   5e10
        poison      =   0.27
        dilation    =   45
        friction    =   45
        cohesion    =   40e+6
        # DARCY Parameters:
        rhol            = 1000
        mul             = 1e-4
        Kphi            = 1e-20
        TensileS        = -20e+6
        betam           = 1e-10
        betal           = 1e-12
        Phi             = 0.01
        poisonu         = 0.27
        Kphiu           = 1e-20
        Phiu            = 0.01
    <MaterialEnd>
    <MaterialStart>  # pipe
        ID          =   9
        rho0        =   3000
        shear       =   5e10
        poison      =   0.27
        dilation    =   10
        friction    =   35
        cohesion    =   20e+6
        # DARCY Parameters:
        rhol            = 1000
        mul             = 1e-4
        Kphi            = 1e-40
        TensileS        = -10e+6
        betam           = 1e-10
        betal           = 1e-12
        Phi             = 0.0005
        poisonu         = 0.27
        Kphiu           = 1e-40
        Phiu            = 0.0005
    <MaterialEnd>
# End of defining material properties for all phases -----------------------------------

# Darcy source -------------------------------------------------------------------------
# -------------------------------------------------------------------------------------
# -------------------------------------------------------------------------------------
NumDarcySources     = 5
<DarcySourceStart>
    ID          =   0           # source id
```

```
    x           =   1500
    y           =   2000
    z           =   800
    magnitude   =   1e1
    increment   =   0e-5
    tini        =   2001
    tfin        =   1610000000
<DarcySourceEnd>
<DarcySourceStart>
    ID          =   1           # source id
    x           =   1800
    y           =   2000
    z           =   700
    magnitude   =   1e1
    increment   =   0e-5
    tini        =   2001
    tfin        =   1610000000
<DarcySourceEnd>
<DarcySourceStart>
    ID          =   2           # source id
    x           =   2100
    y           =   2000
    z           =   600
    magnitude   =   1e1
    increment   =   0e-5
    tini        =   2001
    tfin        =   1610000000
<DarcySourceEnd>
<DarcySourceStart>
    ID          =   3           # source id
    x           =   -2500
    y           =   100
    z           =   1550
    magnitude   =   5e-4
    increment   =   0e-5
    tini        =   1501
    tfin        =   1610000000
<DarcySourceEnd>
<DarcySourceStart>
    ID          =   4           # source id
    x           =   -1000
    y           =   100
    z           =   1550
    magnitude   =   -5e-4
    increment   =   0e-5
    tini        =   1501
    tfin        =   1610000000
<DarcySourceEnd>
<DarcySourceStart>
    ID          =   5           # source id
    x           =   -1000
    y           =   250
    z           =   2000
    magnitude   =   -1e-3
    increment   =   0e-5
    tini        =   1001
    tfin        =   16100000
<DarcySourceEnd>
<DarcySourceStart>
    ID          =   6           # source id
    x           =   -1000
    y           =   250
    z           =   2500
    magnitude   =   -0.5e1
    increment   =   0e-5
    tini        =   301
    tfin        =   161000
<DarcySourceEnd>
<DarcySourceStart>
    ID          =   7           # source id
    x           =   -1000
    y           =   1500
    z           =   2950
    magnitude   =   -0.5e1
    increment   =   0e-5
    tini        =   301
    tfin        =   161000
<DarcySourceEnd>
# ------------------------------------------------------------------------------
```

Chapter 3

3D numerical simulation of fluid injection and crack propagation in geological media with complex rheologies[1]

Abstract

Stimulation of geothermal systems by injection of water into wells at high pressures to create fractures and increase permeability of rocks is a widely employed technique. Therefore, increasing our understanding about how such actions influence and are affected by the local stress state of the reservoir and how fractures propagate through it is necessary to efficiently develop extraction projects and, hopefully, to avoid undesired side effects. Advances in numerical modelling of hydraulic fracturing are thus required. To that end,

[1]This chapter will be submitted for publication as: Beatriz Martínez Montesinos, Boris J.P. Kaus and Anton A. Popov, Institute of Geosciences, Johannes Gutenberg University of Mainz, '3D numerical simulation of fluid injection in complex rheologies. Butterfly-like fractures emerging in high stressed reservoirs'

we improved the software LaMEM by adding plasticity, poro-elasticity and Darcy flow in order to simulate dilatant materials and reproduce shear/tensile failures due to local pore pressure increase. This offers a new and efficient computational massively-parallel 3D code to model fluid injection and crack propagation in poro-visco-elasto-plastic rheologies. We reproduce existing 2D benchmarks and give some examples of 3D cases. The results show the importance of the initial stress conditions on the development of failure zones and give a generalization of failure patterns generated from a local increase of pore pressure.

3.1 Introduction

Although geothermal energy has been harnessed since ancient times, such energy appears to be a viable resource to supply humanity needs today due to recent technological advances. Yet, in most cases the natural permeability is insufficient for industrial applications and thus needs to be enhanced by the injection of water into wells at high pressures to create fractures and increase permeability of rocks. As the development of these projects is expensive (drilling and exploitation) and undesired side effects can occur (earthquakes or contamination of aquifers), they must be carried out in an optimal and safe way (e.g., Lukawski et al. (2014), Majer et al. (2007), Nur (1971), Cesca et al. (2014), Mignan et al. (2015)).

The main geological factors acting in these processes are the stress conditions of the reservoir, the rheology and permeability of rocks and the characteristics of the injection source (e.g., Nur (1971), Miller & Nur (2000), Rozhko et al. (2007), failureMoeck (2014)). The physics involving these factors, describing how they are related to each other, are given by the constitutive relations of materials and the conservation laws of physics. These relations can be approximately expressed, in a mathematical way as a system of partial differential equations that is not amenable to analytical solutions. Furthermore, the rheology of rocks is complex and non-linear and the range of time

scales needed to track the evolution of these processes is large. Therefore, efficient numerical methods and software are required to simulate realistic problems.

LaMEM (Lithosphere and Mantle Evolution Model)[2] (Lithosphere and Mantle Evolution Model) (Kaus et al. (2016)), a scalable 3D parallel code that employs a staggered finite difference discretization combined with a marker and cell approach, was developed to simulate geological processes such as lithospheric deformation (e.g. Schmeling et al. (2008), Lechmann et al. (2014), Pusok & Kaus (2015), Collignon et al. (2016)). This software solves, in an efficient way, the incompressible Stokes equations in rheologies involving rocks that have nonlinear visco-elasto-plastic material properties and, in particular, is able to model the formation of localized shear bands during planar deformation. However, dilation of materials, tensile failure modes and liquid pressure in porous rocks must be considered when modelling deformation and failure, as it is well know that they play an important role in natural and industrial processes such as enhanced geothermal systems (e.g., Vermeer & De Borst (1984), Häring et al. (2008), Shapiro & Dinske (2009)).

We take advantage of LaMEM and follow previous ideas (Rozhko et al. (2007), Galvan & Miller (2013), Simpson (2017)) to implement Darcy flow and couple it with the Stokes equations in order to account for liquid pressure in porous rocks. In addition, we improve deformation and plasticity by adding the dilation angle of materials and by implementing tensile failure, one of the possible failure modes due to local pore-fluid overpressuring and/or extensional forces (Vermeer & De Borst (1984), Gerya (2009)).

Here, we start with describing the physical model used for this purpose and its numerical implementation. Next, in sections 3.3.1 and 3.3.2, we benchmark the code for 2D cases and, finally, we perform 3D poro-visco-elasto-plastic simulations of high-pressure injection of water into a borehole to create fractures and understand how stress conditions influence their propagation.

[2]See https://bitbucket.org/bkaus/lamem

3.2 Physical and numerical approach

We consider a continuous media under the effect of gravity (g) composed by poro-visco-elasto-plastic rocks with properties density (ρ), shear modulus (G), bulk modulus (K) and viscosity (μ). To describe the main factors acting in the medium we use temperature (T), pressure (P), the Cauchy (σ_{ij}) and the deviatoric ($\tau_{ij} = \sigma_{ij} + P\delta_{ij}$) stress tensors and, to describe deformation, the velocity vector (v_i), the strain rate tensor ($\dot{\varepsilon}_{ij}$) and its poro-elastic, viscous and plastic decomposition

$$\dot{\varepsilon}_{ij} = \dot{\varepsilon}^{pe}_{ij} + \dot{\varepsilon}^{v}_{ij} + \dot{\varepsilon}^{p}_{ij}. \tag{3.1}$$

Here i, j refers to coordinate indexes and, hereinafter, we will use Einstein summation convention.

We assume that pores are connected and filled, in a measure given by the permeability (k) and the specific storage (S_s) properties, by a liquid of density ρ_l exerting pressure (P_l) on rocks. We define, then, the effective pressure of the system as

$$P_{eff} = P_{total} - P_l. \tag{3.2}$$

In addition, we assume the existence of a limit for rock stresses, the scope of which produces plastic failure and is defined by cohesion (C), friction angle (ϕ) and tensile strength (σ_T). The combined yield criteria for shear (Paterson & Wong (2005)) and tensile failure (Murrell (1964)) that we use is given by (Figure 3.1)

$$\tau_{yield} = \min\left(P_{eff}\sin\phi + C\cos(\phi), P_{eff} + \sigma_T\right), \tag{3.3}$$

and the plastic behaviour is defined by the plastic flow potential (Vermeer & De Borst (1984), Moresi et al. (2007))

$$Q \;=\; \tau_{II} - P_{eff}\sin(\psi), \tag{3.4}$$

being ψ the dilation angle indicating the relation between the plastic volumetric strain rate and the rate of plastic distortion (Vermeer & De Borst

(1984))

$$\dot{\varepsilon}_v^p = 2\sin(\psi)\dot{\varepsilon}_{II}^p, \tag{3.5}$$

with $\psi = 90^o$ for tensile failure, and denoting $\tau_{II} = \left(\frac{1}{2}\tau_{ij}\tau_{ij}\right)^{\frac{1}{2}}$ and $\dot{\varepsilon}_{II} = \left(\frac{1}{2}\dot{\varepsilon}_{ij}\dot{\varepsilon}_{ij}\right)^{\frac{1}{2}}$ the second invariant of the deviatoric stress and the plastic strain rate, respectively.

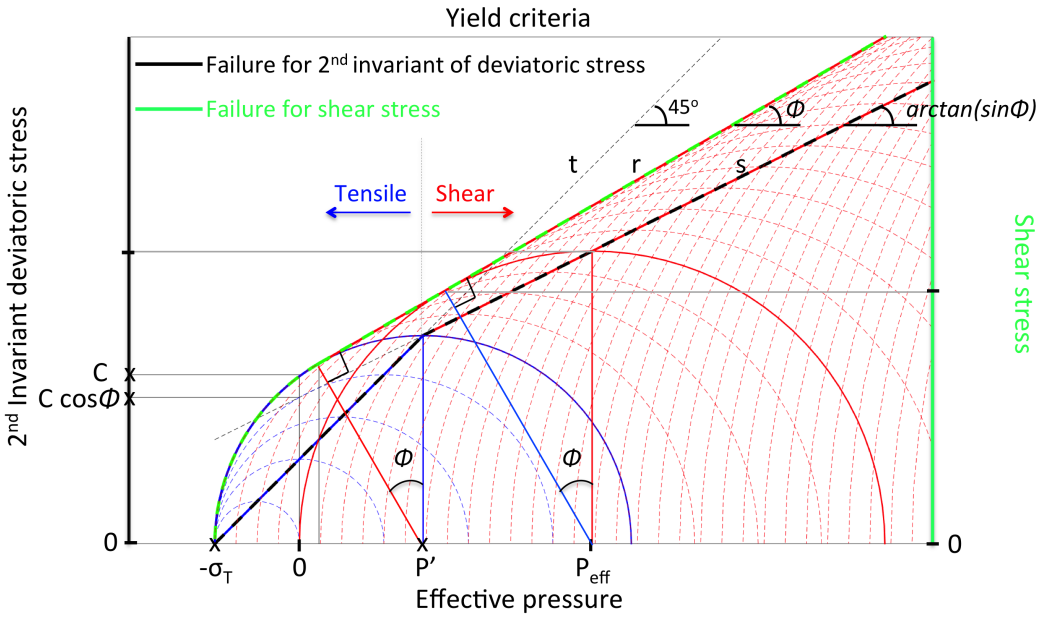

Figure 3.1: The yield criteria for the second invariant of the deviatoric stress considered for plastic failure in equation 3.3 is plotted as dashed black line. $P^{'}$ indicates the effective pressure corresponding to the intersection between the line $t : P_{eff} + \sigma_T$, that forms an angle of 45^o with respect to the horizontal axis, and the line $s : P_{eff}\sin\phi + C\cos(\phi)$, with an angle of $\arctan(\sin(\phi))$. Its analytical value is $P^{'} = (\sigma_T - C\cos\phi)/(\sin\phi - 1)$. On the other hand, the set of all the semicircles with center P_{eff} and radius $\tau_{yield}(P_{eff})$, plotted in blue for tensile and in read for shear, defines the yield criteria for shear stress and is given by a combination between the semicircle corresponding to $P^{'}$ (in red) and the line $r : P_{eff}\tan\phi + C$ with angle ϕ. Such envelope is plotted as a dashed green line.

If yield is reached, the plastic strain rates are given by

$$\dot{\varepsilon}_{ij}^p = \chi\,\frac{\partial Q}{\partial \sigma_{ij}}, \tag{3.6}$$

where χ are multipliers satisfying the yield condition

$$\tau_{II} = \tau_{yield}. \tag{3.7}$$

We solve the mass, momentum and energy conservation equations for the solid skeleton affected by the liquid pressure,

$$\alpha_T \frac{DT}{Dt} - \frac{1}{K}\frac{DP}{Dt} + 2\sin(\psi)\dot{\varepsilon}^p_{II} = \frac{\partial v_i}{\partial x_i}, \tag{3.8}$$

$$\frac{\partial \tau_{ij}}{\partial x_j} - \frac{\partial (P + \alpha P_l)}{\partial x_i} + \rho g_i = 0, \tag{3.9}$$

$$\rho C_p \frac{DT}{Dt} = \frac{\partial}{\partial x_i}\left(\lambda \frac{\partial T}{\partial x_i}\right) + H, \tag{3.10}$$

where D/Dt is the material time derivative, α_T is the thermal expansion coefficient, α is the Biot-Willis constant and H a possible heat source, and we consider the poro-visco-elasto-plastic constitutive relation

$$\dot{\varepsilon}_{ij} = \frac{1}{2G}\frac{\hat{D}\tau_{ij}}{Dt} + \dot{\varepsilon}^{vs}_{II}\frac{\tau_{ij}}{\tau_{II}} + \dot{\varepsilon}^{p}_{II}\frac{\tau_{ij}}{\tau_{II}}, \tag{3.11}$$

being $\hat{D}/Dt$ the Jaumann derivative giving an expression for the objective stress rate

$$\frac{\hat{D}\tau_{ij}}{Dt} = \frac{\partial \tau_{ij}}{\partial t} + \tau_{ij}\omega_{kj} - \omega_{ik}\tau_{kj}, \tag{3.12}$$

where $\omega_{ij} = \frac{1}{2}\left(\frac{\partial v_i}{\partial x_j} - \frac{\partial v_j}{\partial x_i}\right)$ is the spin tensor, and the viscous part of the deviatoric strain rate is defined as

$$\dot{\varepsilon}^{vs}_{II} = \dot{\varepsilon}_l + \dot{\varepsilon}_n, \tag{3.13}$$

where $\dot{\varepsilon}_l = B_l \exp\left[-\frac{E_l + PV_l}{RT}\right]\tau_{II}$ and $\dot{\varepsilon}_n = B_n \exp\left[-\frac{E_n + PV_n}{RT}\right](\tau_{II})^n$ are diffusion and dislocation components, respectively, and B, E and V denote the creep constant, the activation energy and the activation volume for the corresponding mechanism, n is the stress exponent of the dislocation creep and R the gas constant.

Pore pressure (P_l), is calculated through the mass conservation equation combined with the Darcy's law for liquids

$$\frac{\partial}{\partial x_i}\left(\frac{k}{\mu}\left(\frac{\partial P_l}{\partial x_i} - \rho_l g e_3\right)\right) + H_l = S_s \frac{DP_l}{Dt}, \tag{3.14}$$

being e_3 a unit vertical vector, k the permeability, μ the liquid viscosity and S_s the specific storage defined as

$$S_s = \alpha_l + \phi_l \beta_l, \tag{3.15}$$

where ϕ_l is the effective porosity, α_l and β_l are the matrix and liquid compressibility, respectively, and H_l is a possible liquid source.

We discretize the conservation equations 3.8, 3.9, 3.10 and 3.14 in space by using the staggered grid finite difference method. To achieve scalability on massively parallel machines we use the distributed arrays (DMDA) and iterative solvers (KSP, SNES) from the PETSc library (Balay et al. (2018)). A Marker and Cell method is employed to track material properties, which are advected in an Eulerian kinematical framework.

To account for the effective-pressure dependency for permeability, porosity and Poison's ratio, we use drained values of such properties if the liquid pressure is hydrostatic, undrained values when effective pressure reaches the tensile strength and a linear function for intermediate values (Galvan & Miller (2013)). During the advection, the phase of materials can be changed, upon reaching yield.

3.3 Results

3.3.1 Elasto-plastic bechmark - Shear band angle

Among others, shear band formation of elasto-plastic soil samples, where friction and cohesion control planar deformation, was theoretically studied in Vermeer (1990). The author reviewed existing theories about preferred orientation of shear bands (e.g., Coulomb (1773), Roscoe (1970), Arthur et al. (1977)) and concludes, by means of analytical and experimental data, that shear bands for a material with friction angle ϕ and dilation angle ψ are oriented, with respect to the direction of the minor principal stress, at an angle that varies, depending of the particle size and elastic unloading,

between the Roscoe angle $45^o + \psi/2$ (Roscoe (1970)) and the Coulomb angle $45^o + \phi/2$ (Coulomb (1773)). This range includes the Arthur or intermediate angle $45^o + (\phi + \psi)/4$ proposed in Arthur et al. (1977).

Numerical experiments done by Poliakov et al. (1994), Popov & Sobolev (2008), Lemiale et al. (2008), Kaus et al. (2010), Le Pourhiet (2013), Galvan & Miller (2013), have similar results for non associated incompressible flow ($\psi = 0$) while Choi & Petersen (2015) demonstrated, as previously suggested other authors (e.g. Gerya & Yuen (2007), Buiter (2012)), that the Coulomb angle is the preferred orientation of shear bands if an associated plastic flow rule is considered, where the plastic potential function and the yield function coincide since in such case $\phi = \psi$.

Here, we test the influence of the implemented dilation angle on the preferred orientation of shear bands by performing uniaxial compressional and extensional simulations in a model setup consisting of an elasto-plastic domain with 40 km length, 0.625 km width and 10 km height. A viscous heterogeneity 0.8 km long, 0.625 km wide and 0.4 km high is introduced at the bottom to initiate the shear bands. We impose a free surface at the top and zero normal velocity and free slip at the bottom. Properties of the materials, numerical parameters and sketch of the model setup are given in Tables 3.1 and 3.3 and Figure 3.2, respectively.

First, we run simulations considering a fixed friction angle $\phi = 30^o$ and varying dilation angles to $\psi = 0^o$, $\psi = 10^o$ and $\psi = 30^o$ and with lateral compression by imposing a constant background strain rate of $10^{-15} s^{-1}$ until bands clearly localize. In all simulations, we measure the angle between the shear band and the horizontal axis, therefore, as in the case of compression the minimum principal stress is vertical, the theoretical Roscoe, Coulomb and Arthur angles with respect to the horizontal axis are $45^o - \psi/2$, $45^o - \phi/2$ and $45^o - (\phi + \psi)/4$, respectively. Figure 3.3 shows the second invariant of the strain rate tensor for the different dilation angles and Table 3.2 gives a summary of the expected and resulted shear angles for each case.

We observe that dilation decreases the angle of shear bands significantly,

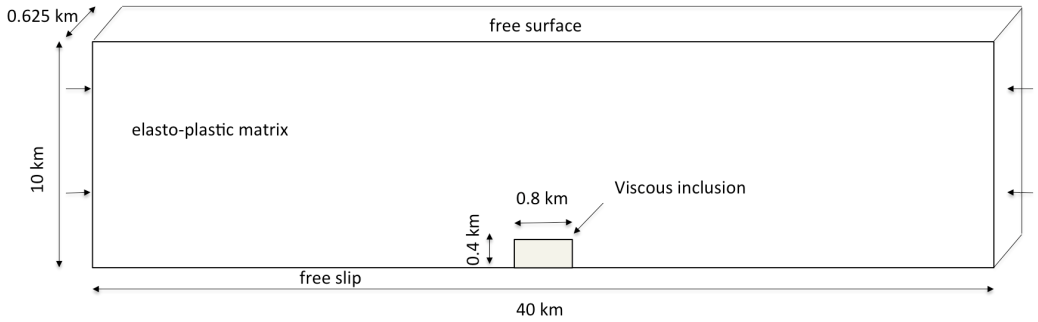

Figure 3.2: Quasi-2D model setup used for the shear bands benchmark.

Table 3.1: Material parameters employed in the shear bands benchmark.

Variable	Parameter	Value	Units
ρ	Density	2700	kg m^{-3}
G	Shear module	$5{\times}10^4$	MPa
ν	Poison's ratio	0.3	
C	Cohesion	40	MPa
ϕ	Friction angle	30	(°)
ψ	Dilation angle	[0,10,30]	(°)
σ_T	Tensile strength	20	MPa
μ	Viscosity of weak inclusion	10^{20}	Pa s

moving it towards the Roscoe and the Arthur angles. Furthermore, Figure 3.4 shows that, a larger numerical resolution further move the resulted shear band angle closer to the Coulomb angle, as Lemiale et al. (2008) and Kaus (2010) demonstrated.

Next, we subject the same model to extension by means of a constant background strain rate of $10^{-15}s^{-1}$ for the case $\phi = 30^o$, $\psi = 10^o$. In order to compare the initiation of bands close to the surface, for the compressional and extensional case, we plot in Figure 3.5 the second invariant of the strain rate tensor and Mohr-Coulomb circles for some specific points resulting of the simulations. We can appreciate that for the compressional case (first row) only shear bands form whereas vertical tensile fractures appear in the extensional one (second row). If extension is maintained for longer shear localization occurs forming an angle of 55^o with respect to the horizontal

axis.

In all cases, results are as expected from the physical formulation and the position in the yield criteria.

Table 3.2: Theoretical and calculated angles for shear bands in Figures 3.3, 3.4 and 3.5.

	Friction ϕ (°)	Dilation ψ (°)	Roscoe $\left(45 \mp \frac{\psi}{2}\right)^o$	Arthur $\left(45 \mp \frac{\psi+\phi}{4}\right)^o$	Coulomb $\left(45 \mp \frac{\phi}{2}\right)^o$	Results ^{o}
Compression	30	0	45	37.5	30	42/37
	30	10	40	35	30	39
	30	30	30	30	30	31
Extension	30	10	50	55	60	55

Table 3.3: Numerical resolution and PETSc options employed in the simulations. For all of them we use a direct solver, Eisenstat Walker algorithm for SNES solver and FGMRES for Jacobian.

	Parameter	Figure 3.3	Figures 3.4 and 3.5
Numerical resolution		200x2x50	400x2x100
Absolute convergence tolerance	-snes_atol	$1x10^{-7}$	$1x10^{-15}$
Relative convergence tolerance	-snes_rtol	$1x10^{-4}$	$1x10^{-15}$
Maximum number of iterations	-snes_max_it	100	500
Absolute convergence tolerance	-js_ksp_atol	$1x10^{-14}$	$1x10^{-14}$
Relative convergence tolerance	-js_ksp_rtol	$1x10^{-10}$	$1x10^{-10}$
Maximum number of iterations	-ksp_max_it	100	500

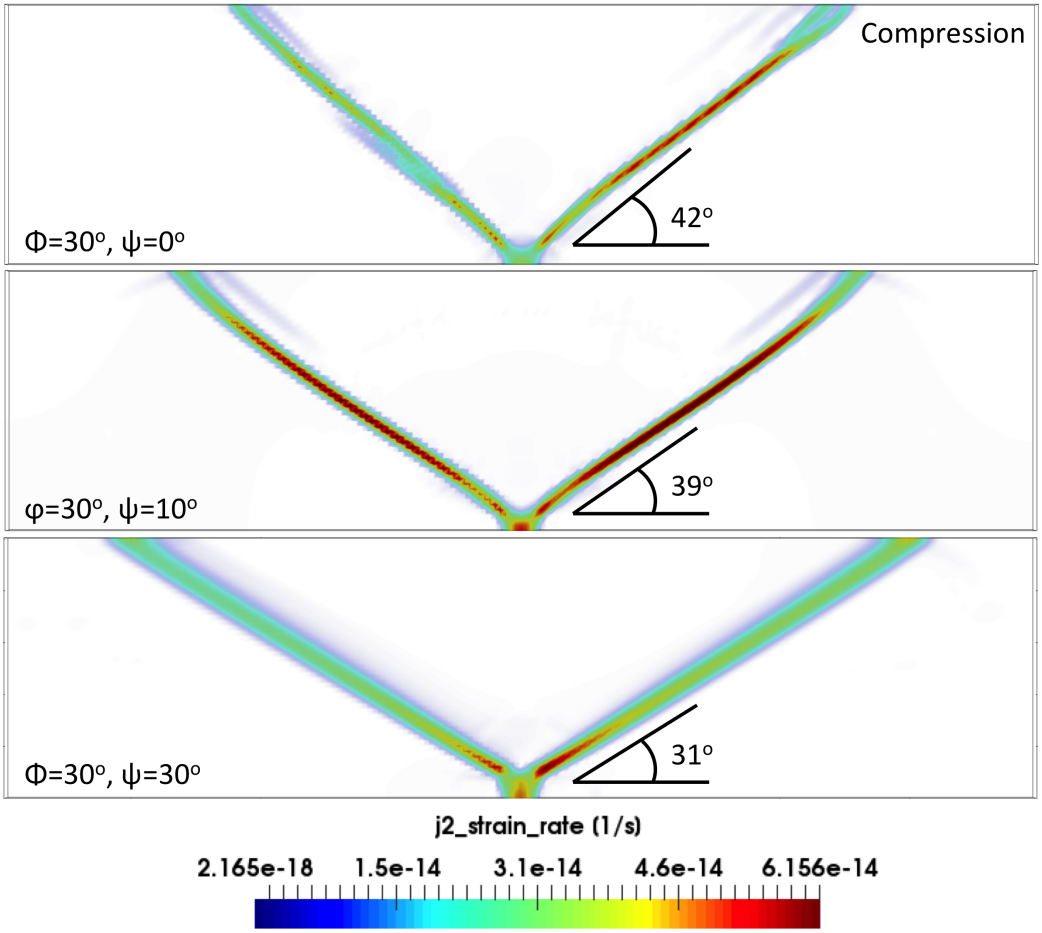

Figure 3.3: Simulations of shear band localization due for a lateral uniaxial compression of a medium described in Table 3.2 and Figure 3.1 using a numerical resolution of 200x2x50, and other solver parameters indicated in Table 3.3. We plot in first, second and third rows the second invariant of the strain rate tensor resulting of considering dilation angles $\psi = 0^o$, $\psi = 10^o$ and $\psi = 30^o$, respectively, and a fixed friction angle $\phi = 30^o$. We measured the angles of shear bands by looking for the maximum strain rate on the horizontal line at 0.6 km and 2.6 km from the centre of the domain. Comparison with theoretical results are showed in Table 3.2.

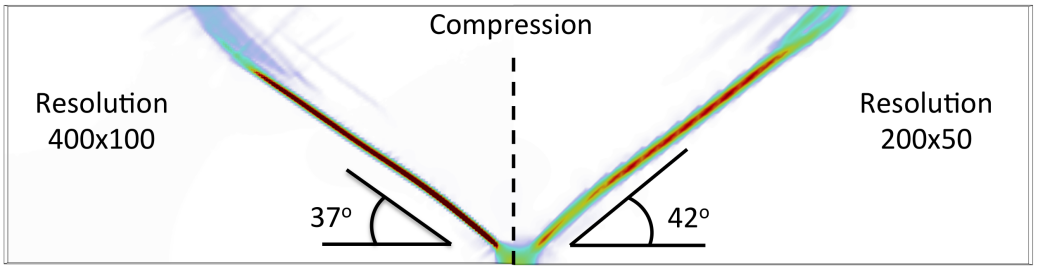

Figure 3.4: Effect of the numerical resolution on the angle of shear bands. Right area shows the first simulation in Figure 3.3, corresponding to a model setup with $\phi = 30^o$ and $\psi = 0^o$ using a numerical resolution of 200x2x50. Left part shows the same simulation using a numerical resolution of 400x2x100.

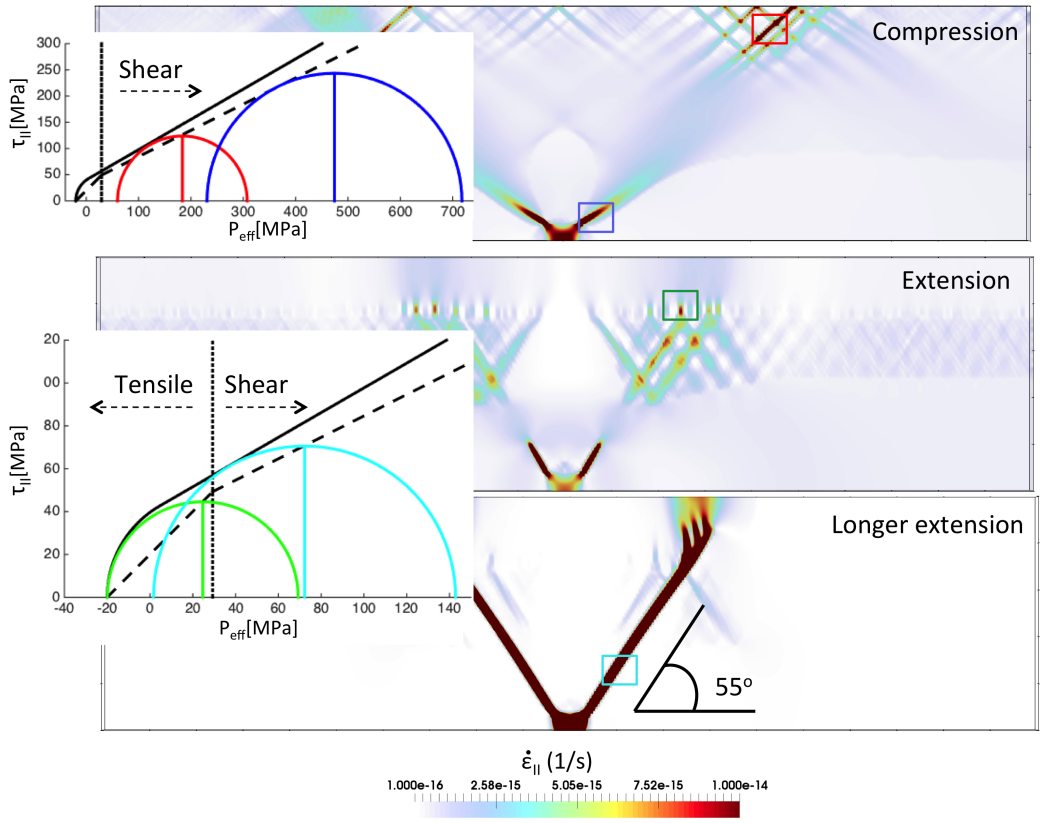

Figure 3.5: Second invariant of the strain rate tensor, yield criteria and pressure-deviatoric stress state resulting of simulating lateral uniaxial compression/extension of a medium described in Table 3.1 and Figure 3.2 using a numerical resolution of 400x2x100, and other solver parameters indicated in Table 3.3. For all simulations we employ a friction angle $\phi = 30^o$ and dilation angle $\psi = 10^o$. First row shows the initiation of shear bands for the case of compression and pressure-stress state at the central point of the squares superposed in the domain. Squares and semicircles on the graphic are related each other by colour and show the locally measured stress state together with the yield stress envelop. Second and third rows show the results for the case of extension at two different time stages of the simulation. Tensile fractures appear in these cases and shear localization is produced as in the case of compression. We measured the angle and compared results in the same way as in Figure 3.3.

3.3.2 Poro-elasto-plastic benchmark - 2D Failure patterns

It is well know that liquid pressure in porous rocks plays an important role in processes such as enhanced geothermal systems as it influences the state of stress of the reservoir (e.g. Häring et al. (2008), Shapiro & Dinske (2009)). Rozhko et al. (2007) studied how a local increase in pore pressure affects the mode in which poro-elasto-plastic rocks fail. Furthermore, they derive an analytical solution for the value of the pre-failure pore pressure and perform systematic simulations in a poro-elasto-plastic 2D-model in order to understand the interaction between the local pore pressure increase and the developing of failure patterns. Results show the existence of five different failure patterns depending on initial stress conditions, material properties and geometry.

We benchmark our code by performing five numerical simulations to reproduce such failure patterns considering the same parameters and initial conditions used in Rozhko et al. (2007). To that end, we consider a 4000 m length, 62.5 m width, 1000 m height quasi-2D poro-elasto-plastic domain where a 50 m low permeability boundary layer is imposed at the bottom and lateral boundaries (Figure 3.6).

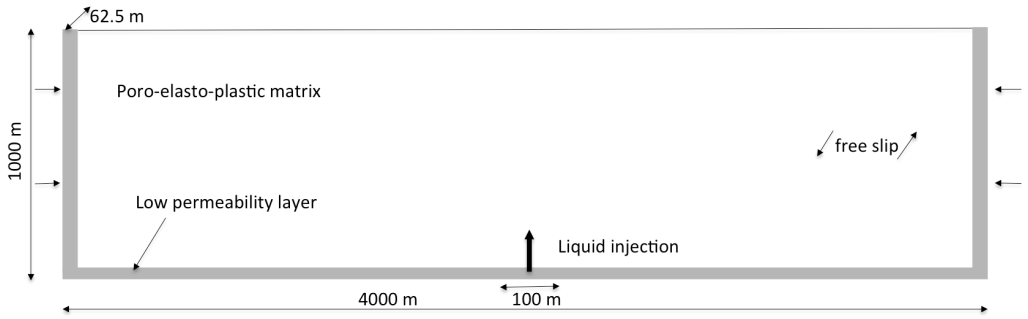

Figure 3.6: Model setup used for the 2D-poro-elasto-plastic benchmark.

We subject the model to uniaxial compression or extension, to create the

required stress conditions, at the time that liquid is injected at the centre of the bottom boundary in order to modify effective pressure in that area. The properties of the materials and the stress conditions used for each case are given in Tables 3.4 and 3.5. As we can see in these tables the only differences between the five media are the tensile and the cohesion values and the principal stresses σ_V (vertical) and σ_H (horizontal) acting in the medium.

To understand how such factors influence in the mode in which failure nucleates we can take a look to Figure 3.1 to observe that high normal stresses take the center of the Mohr circle towards the right in the graphic, differences between stresses $(\sigma_H - \sigma_V)$ affect its ratio and low cohesion expands the possibility to fail in shear mode while low tensile strength increases the possibility to fail in tensile mode. Also, Rozhko et al. (2007) provide a phase diagram of failure-onset patterns for a two dimensional setup showing the influence of cohesion and stress initial conditions on the mode in which failure occurs due to localized pore-pressure increase. Approximately, if the magnitude of difference between principal stresses normalized by cohesion $\left|\frac{\sigma_V - \sigma_H}{C}\right|$ is small, tensile failure can occur (Patterns III and IV in Figure 3.7) while shear failure prevails if this quantity is higher (Patterns I and II), whereas high value of $\frac{\sigma_V}{C}$ helps to start failure at the surface (Patterns V).

Figure 3.7 shows the resulting failure modes. In the case of patterns I and III, both correspond to a medium in extensional regime $(\sigma_H < \sigma_V)$. Pattern I corresponds to a shear localization starting in the injection point resulting in a normal fault. Instead, considering a slight lower horizontal stress and a significantly higher and lower cohesion and tensile values, respectively, than for the pattern I, a band localization in tensile mode occurs producing pattern III. On this case, the direction of localization correspond to the direction of the maximum stress, σ_V. In the case of patterns II and IV, both correspond to a medium in compressional regime $(\sigma_H > \sigma_V)$. Pattern II corresponds to a shear localization starting in the injection point resulting in a reverse fault.

Table 3.4: Material parameters employed in the 2D-poro-elasto-plastic benchmark.

Variable	Parameter	Value	Units
ρ	Density	3000	kg m^{-3}
ρ_l	Liquid density	1000	kg m^{-3}
G	Shear module	2.85×10^{8}	MPa
ν	Poison's ratio	0.30	
C	Cohesion	[2.85,2.85,23.04,115.2,23.04]	MPa
ϕ	Friction angle	33	(^{o})
ψ	Dilation angle	0	(^{o})
σ_T	Tensile strength	[28.5,2.85,7.6608,7.6608,2.88×10^{-8}]	MPa
k	Permeability	10^{-15}	m^2
S_s	Specific storage	10^{-4}	MPa^{-1}
H_m	Source magnitude	[1.65, 5.5, 0.15, 0.8,0.01]	m^{3}s^{-1}
α	Biot-Willis constant	1	
$\dot{\varepsilon}_{xx}$	Background strain rate	$[0.38,-1,0.43,-1.95,0.43]\times10^{-13}$	s^{-1}

Instead, considering a higher horizontal stress and a significantly higher cohesion value than for the pattern II, a band localization in tensile mode occurs representing the pattern IV. On this last case, the direction of localization correspond to the direction of the maximum stress, σ_H. Pattern V forms by subjecting the model to extension and considering a very low tensile strength producing nucleation of fracture on the free surface. All the resulting patters are in agreement with the patterns presented in Rozhko et al. (2007).

Table 3.5: Non dimensional parameters used in Rozhko et al. (2007).

Pattern	I	II	III	IV	V
σ_H	$\sigma_V \times 0.2$	$\sigma_V \times 3$	$\sigma_V \times 0.1$	$\sigma_V \times 5$	$\sigma_V \times 0.1$
G	$\sigma_V \times 10^7$	$\sigma_V \times 10^7$	$\sigma_V \times 10^7$	$\sigma_V \times 10^7$	$\sigma_V \times 10^7$
C	$\sigma_V \times 0.1$	$\sigma_V \times 0.1$	$\sigma_V \times 0.8$	$\sigma_V \times 4$	$\sigma_V \times 0.8$
σ_T	$\sigma_V \times 1$	$\sigma_V \times 0.1$	$\sigma_V \times 0.266$	$\sigma_V \times 0.266$	$\sigma_V \times 10^{-8}$
ϕ	33^o	33^o	33^o	33^o	33^o
ψ	0^o	0^o	0^o	0^o	0^o
ν	0.3	0.3	0.3	0.3	0.3
α	1	1	1	1	1

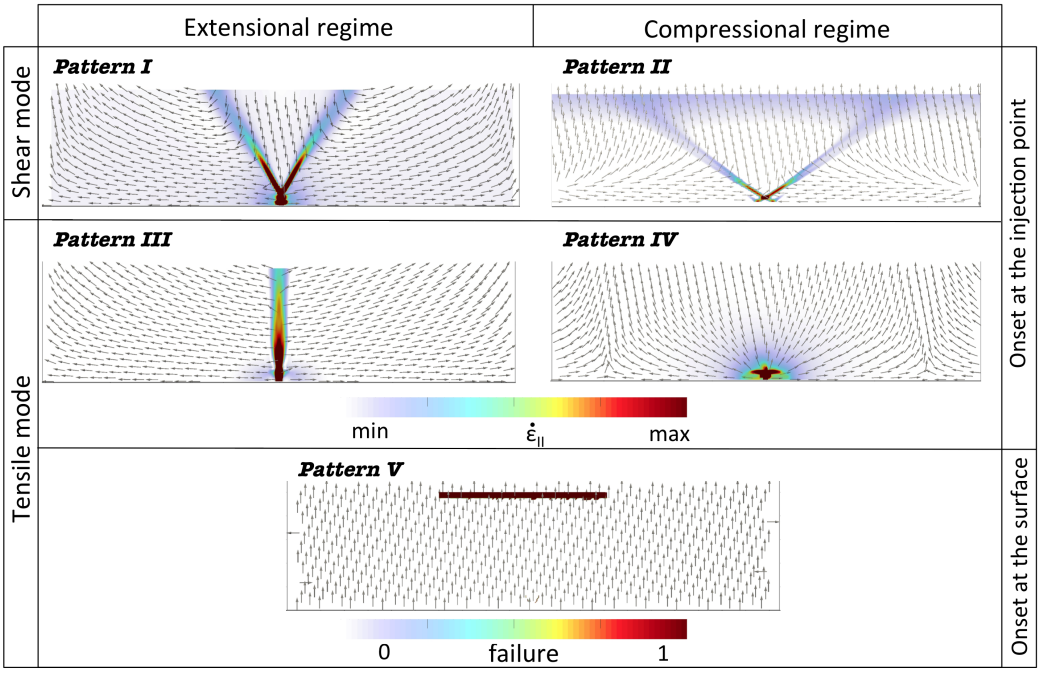

Figure 3.7: Reproduction with LaMEM of the five failure patterns obtained by Rozhko et al. (2007) using the same parameters as there (Tables 3.4 and 3.5). Arrows indicate the velocity field and colors show the second invariant of the strain rate tensor for patterns I to IV, where failure initiates on the injection point, and the area where failure occurs for pattern V, when failure initiates at the surface. Patterns I, III and V result from extension while pattern II and IV are given by compression. Although Pattern V emerge here in an extensional regime, it can also be produced in a compressional one.

3.3.3 Influence of stress conditions - 3D failure patterns

As explained in the previous section, Rozhko et al. (2007) provide a phase diagram of failure-onset patterns for a two dimensional setup showing the influence of material parameters and stress initial conditions on the mode in which failure occurs due to localized pore-pressure increase. For a given medium, if the regime is such that vertical stress, σ_V, and maximum horizon-

tal stress, σ_H, are relatively close to each other failure can nucleate in tensile mode, while shear failure is the preferred mode of initiation if the stress difference, $\sigma_V - \sigma_H$, is high, this, conditioned by the properties of medium. Here, in order to study the three dimensional case, we simulate localized pore-pressure increase in a 3D-poro-visco-elasto-plastic homogeneous setup subjected to uni/bi-axial lateral compression/extension and study how such different stress conditions affect the propagation of plastic failure zones. In this section we focus on the areas where yield stress is reached, rather than on the strain localization bands.

To that end, we use LaMEM to perform numerical simulations of fluid injection at a point 2250 meters depth in a 4000 m length, 2000 m width, 4000 m height domain on which different lateral constant background strain rate were applied to obtain different stress conditions. Model setup and parameters used for the simulations are given in Figure 3.8 and Table 3.6, respectively. In this case impermeable boundaries are not applied whence liquid can circulate in all directions. Furthermore, as formerly we had a single plane and the resulting failure pattern was conditioned by σ_V, σ_H and $\sigma_V - \sigma_H$, now we study the three planes passing through the point of injection defined by every combination of principal stresses, therefore, also the minimum horizontal stress, σ_h, and the stress differences, $\sigma_V - \sigma_h$ and $\sigma_H - \sigma_h$, may play a role.

We first perform a simulation in a medium where no extensional or compressional forces are applied and observe that fracture propagate equally in all directions around the injection point producing a spherical shape as expected for a non stressed medium (Figure 3.9).

Next, we perform the same simulation but with a lower horizontal stress magnitude to get a normal fault high stress regime. Figure 3.10 shows that failure initiates in tensile mode, propagates horizontally in the direction of the medium principal stress (σ_H), generating the pattern IV described in section 3.3.2, and bifurcates in the plane defined by the minimum and maximum principal stresses (σ_h and σ_V), producing the pattern I of such section. 3D

plots of the failure area, exhibited in Figure 3.11, reveal a butterfly-like shape oriented in the direction of the intermediate principal stress, σ_H. Figure 3.12 corresponds to the particular case where both principal horizontal stresses are almost equal, whereby, failure occurs horizontally in both σ_H and σ_h direction, producing pattern III and IV with respect to the horizontal plane, respectively, and bifurcates in both $\sigma_V\sigma_h$ and $\sigma_V\sigma_H$ planes, developing a conic shape with central axis in the maximum principal stress, σ_V. Considering a larger horizontal stresses (Figure 3.13), we can observe, in addition to pattern IV and pattern I, pattern V corresponding to failure developing on the surface.

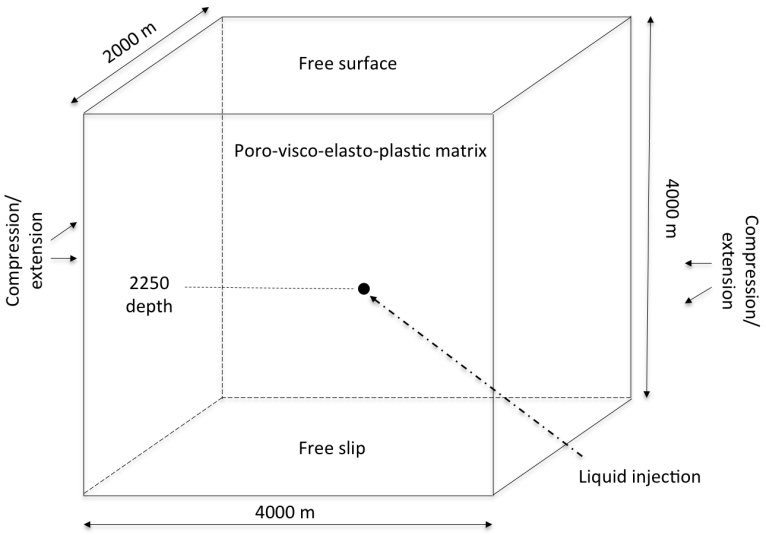

Figure 3.8: Model setup used for the 3D simulations. Fluid is injected at a point 2250 meters depth. Parameters considered are given in Table 3.6.

Figure 3.14 shows examples for each of the three main tectonic stress regimes plotting in first column the results for low stressed media and in second column the same for higher ones. For the low stress cases, failure propagates around the injection point creating spheroidal shape with a predominant plane of propagation defined by the two maximum principal stresses that are

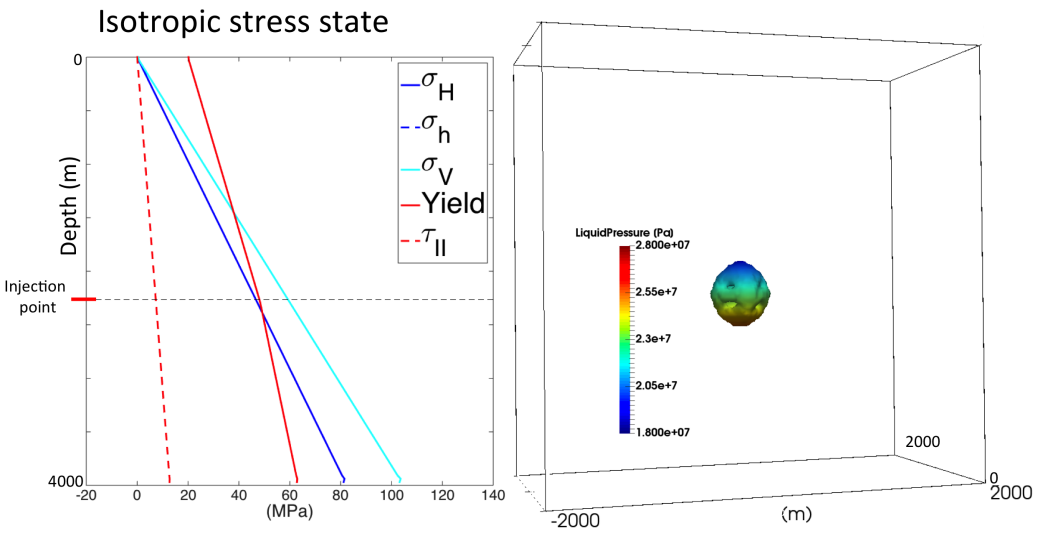

Figure 3.9: Left part shows the stress-state conditions of the medium without lateral forces applied on it and right part the failure area after 1000 seconds of fluid injection. We observe that fracture propagate around the injection point producing a spherical shape.

$\sigma_V\sigma_h$, $\sigma_H\sigma_h$, $\sigma_H\sigma_V$ for first, second and third rows, respectively, and reproducing patterns patterns III and IV in every of the principal planes. Results in the high stressed setups show propagation of failure in the intermediate principal stress that, in the case of first and second rows, are σ_H and σ_h, respectively, producing pattern IV, and, in the case of third row, is σ_V and produces failure pattern III. In addition, bifurcation is done in the plane defined by the higher stress difference $\sigma_V\sigma_h$, $\sigma_H\sigma_V$, $\sigma_H\sigma_h$ for first, second and third rows, respectively, producing patterns I and II and generating, all together, a butterfly-like shape oriented to the intermediate principal stress. Failure can nucleates also in the more stressed areas of the medium and in the surface originating pattern V.

These results suggest that the study of the development of failure zones in 3D can by understand by considering each of the planes defined by pairs of principal stresses and applying similar 2D criteria to each of them. In general,

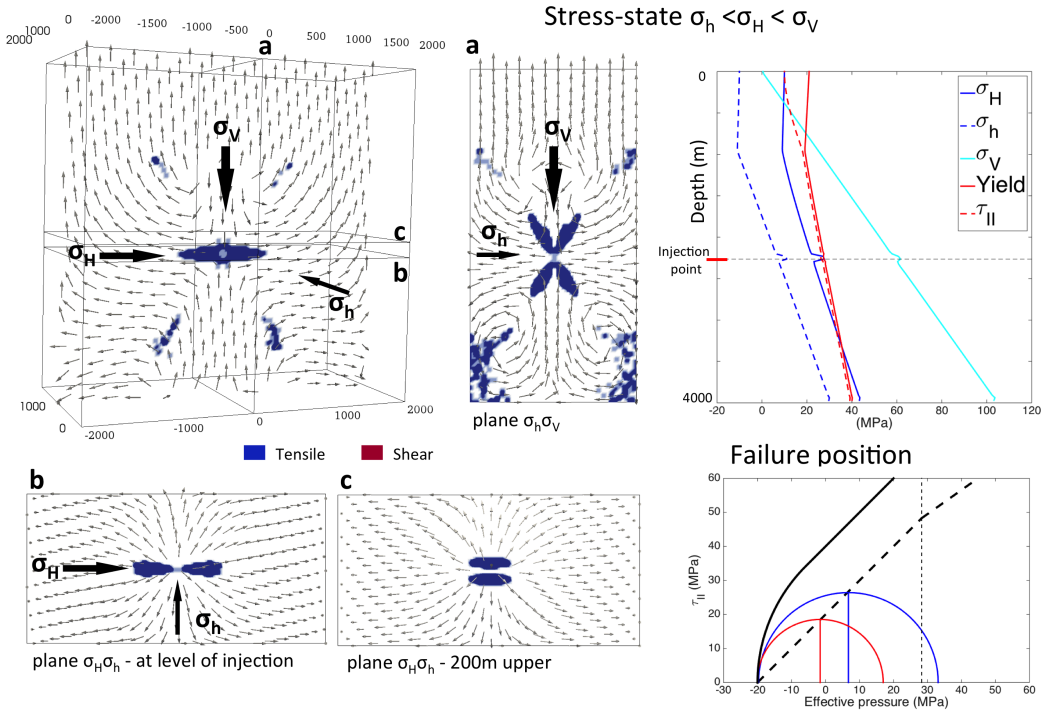

Figure 3.10: Normal faulting stress regime. Left part shows results after 100 seconds of fluid injection in the model defined by Figure 3.8 with stress conditions indicated in the top right of the figure. Arrows represent the velocity field and colors the points where failure is reached. Bottom right part indicates the failure position of the injection point with respect to the yield criteria before injection starts (blue) and when failure is reached (red) showing that failure starts in tensile mode. Plane b shows that fracture propagates horizontally in the direction of the intermediate principal stress, σ_H, which is the maximum principal stress if we focus on this plane. Highest stress difference is given by $\sigma_V - \sigma_h$ producing the bifurcation of failure in the plane $\sigma_V\sigma_h$ (plane a).

we observe that the magnitude of the principal stresses and the difference between them greatly influences the mode in which failure occurs, while the directions of propagation depend on how they are sorted. We observe that, in high stress media, failure escapes quickly while failure remains around the injection point if stresses are low. The predominant propagation direction is the maximum principal stress followed by the intermediate principal stress. If medium is sufficiently stressed fracture bifurcates, being the predominant plane of bifurcation the plane defined by the minimum and the maximum principal stresses. Figure 3.15 is a summary of the main 3D possible failure

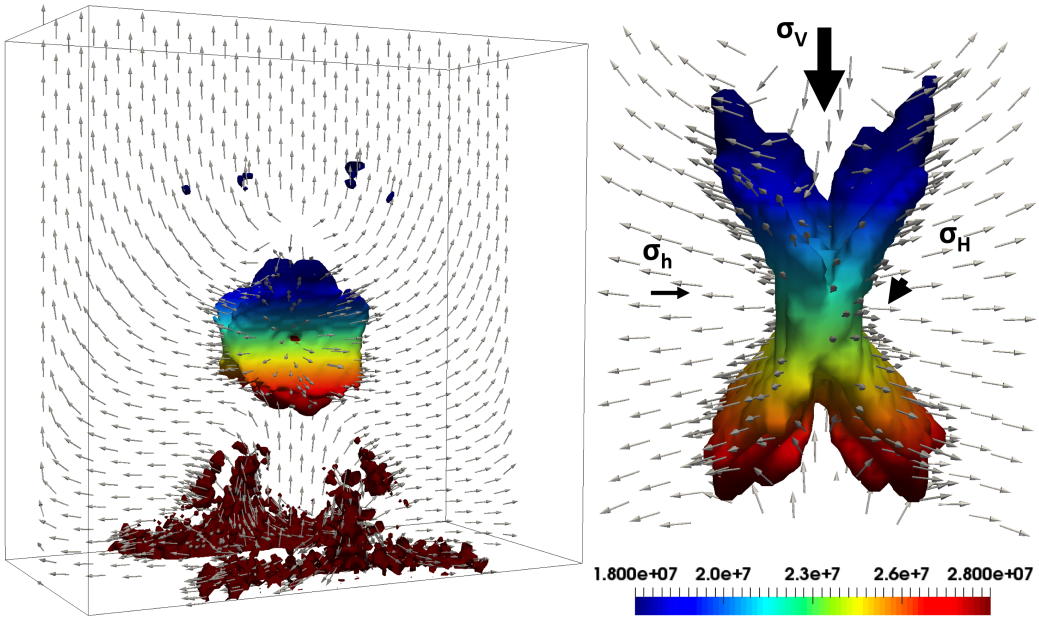

Figure 3.11: 3D plot of failure points corresponding to Figure 3.10. Colors represent liquid pressure and arrows indicate the velocity field. Left part corresponds to the total model setup while right part shows a zooming view of the injection point seen from a different angle. We observe a butterfly-like shape oriented towards the intermediate principal stress, σ_H. Failure occurs also in the bottom part of the model, due to the large stress conditions of the medium which are reflected by the proximity between τ_{II} and yield lines in the stress-state (Figure 3.10).

patterns due to localized pore pressure increase showing that, in low stress conditions, fractures produce dikes, spheres or spheroids, while, in high stress conditions, fractures bifurcate, producing butterfly-like shapes oriented in the direction of the intermediate principal stress.

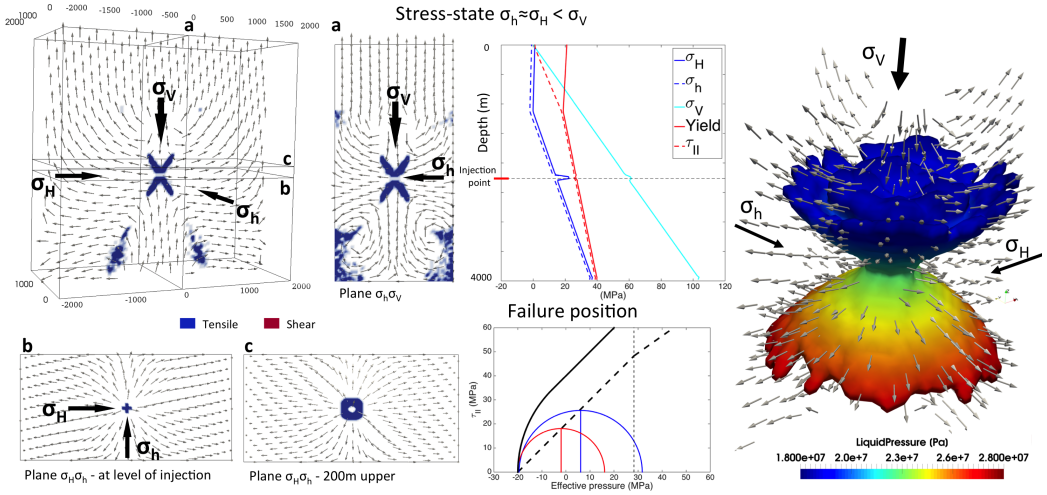

Figure 3.12: Normal faulting stress regime. Figure shows the same than Figures 3.10 and 3.11 but, in this case, both principal horizontal stresses are almost equal. Then, highest stress difference is given by both $\sigma_V - \sigma_h$ and $\sigma_V - \sigma_H$ producing the same propagation pattern in the planes $\sigma_V\sigma_h$ and by $\sigma_V\sigma_H$. Plane b shows that fracture propagates horizontally in σ_H direction and σ_h direction which correspond to the intermediate and lowest principal stresses, respectively. 3D plot shows fracture developing in conic shape with central axis the maximum principal stress, σ_V.

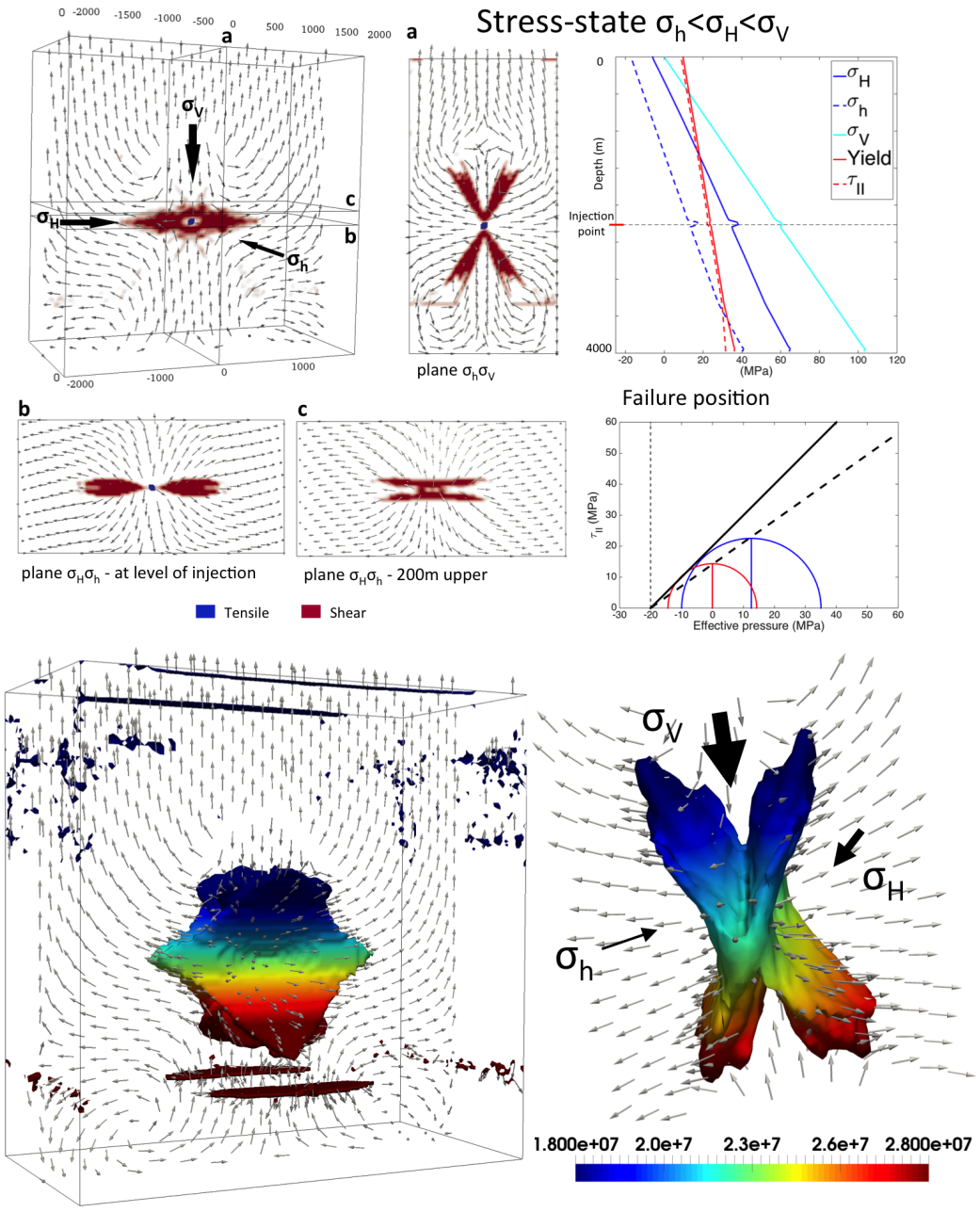

Figure 3.13: Normal faulting stress regime. Figure shows the same than Figures 3.10 and 3.11 but, in this case, even being of the same type of stress regime, stress conditions are different, specially on the surface and bottom part of the model as indicated in the stress-state graphic. Failure starts in shear mode, due to the lower cohesion considered in this simulation. In this case, failure occurs also at the surface, but not in the deeper part of the model. 3D plot shows failure producing a butterfly-like shape, oriented towards the intermediate principal stress, σ_H.

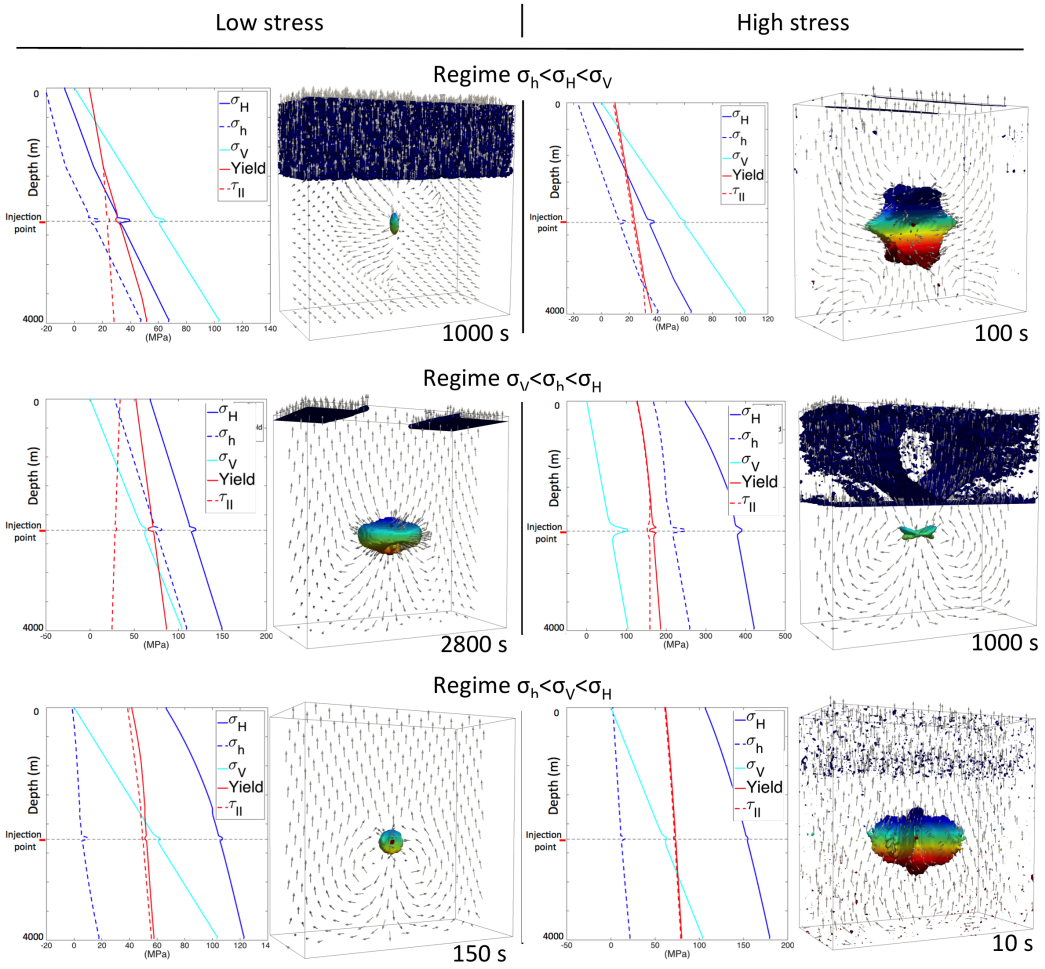

Figure 3.14: Each row shows simulations in different tectonic regimes while first and second columns correspond to lower and higher stressed setups, respectively. In left part, failure develops around the injection point predominantly in the plane defined by the two higher principal stresses and in the right part failure zones bifurcate, developing butterfly-like shapes in the direction of the intermediate principal stress.

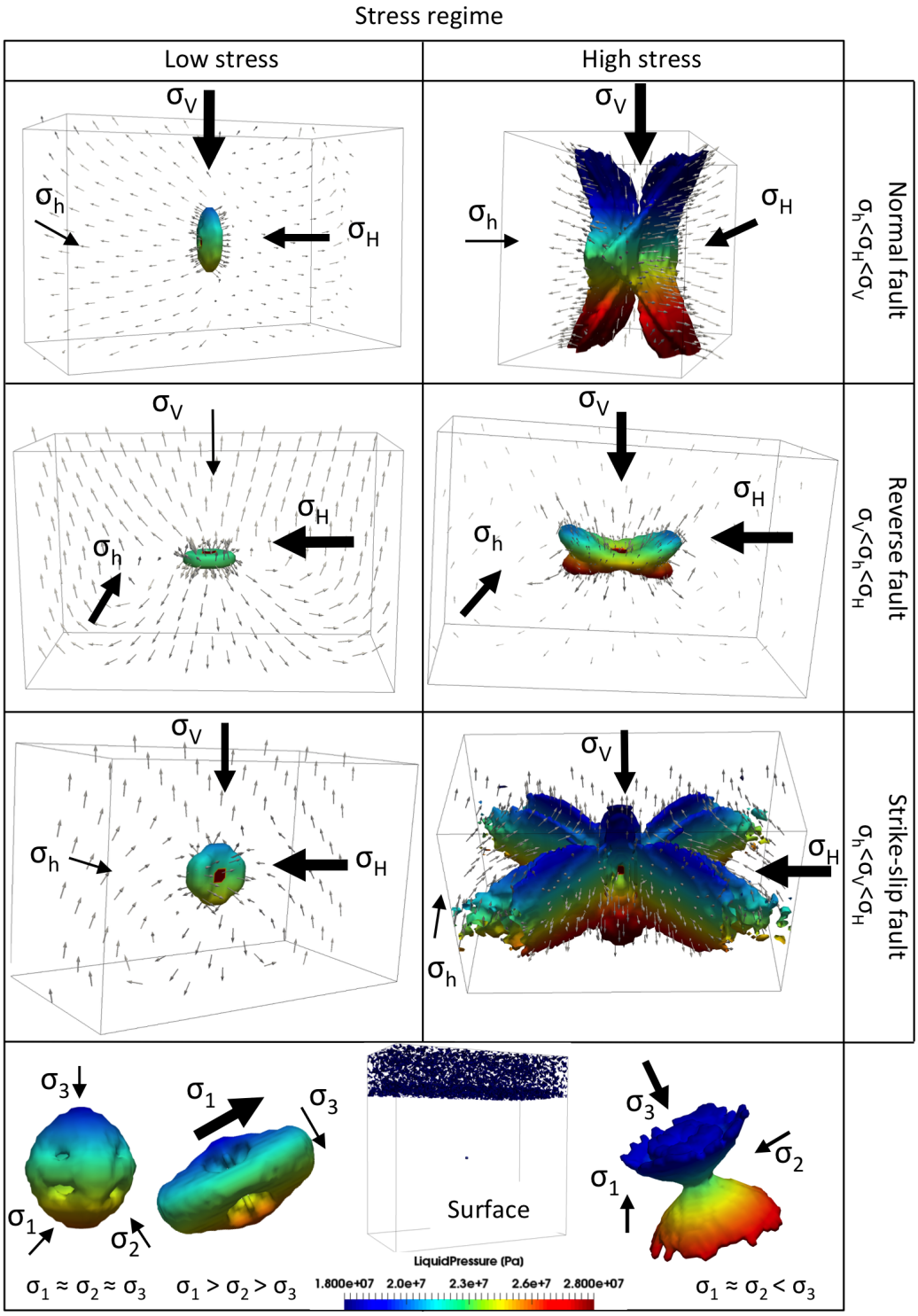

Figure 3.15: Main 3D failure patterns caused by fluid injection. Failure can occur either from the injection point developing on the direction of the dominant principal stresses or bifurcating on the planes defined by the maximum stress differences or nucleating on the surface. In low stress conditions, fractures produce dikes, spheres or spheroids, while, under high stress conditions, fracture bifurcates, producing butterfly-like shapes oriented in the direction of the intermediate principal stress.

Table 3.6: Physical parameters employed in the 3D simulations.

Variable	Parameter	Value [fig.3.9,3.10,3.12,3.13, 3.14 1.1,2.1,2.2,3.1,3.2]	Units
ρ	Density	2600	kg m^{-3}
ρ_l	Liquid density	1000	kg m^{-3}
G	Shear module	2.66×10^{4}	MPa
η	Viscosity	10^{25}	Pa s
ν	Poison's ratio	0.28	
C	Cohesion	[40,40,40,20,40,40,20,40,50]	MPa
ϕ	Friction angle	45	(°)
ψ	Dilation angle	45	(°)
σ_T	Tensile strength	[20,20,20,20,20,20,20,20,30]	MPa
k	Permeability	10^{-16}	m^2
S_s	Specific storage	1.0003×10^{-10}	Pa^{-1}
H_m	Source magnitude	10	m^{3}s^{-1}
α	Biot-Willis constant	0.9	
$\dot{\varepsilon}_{xx}$	Background strain rate in lateral boundaries	$[0,-1,-0.1,0,1,-5,-8,-10,-20]\times10^{-13}$	s^{-1}
$\dot{\varepsilon}_{yy}$	Background strain rate in front boundaries	$[0,0,0,1.2,0,0,0.1,0,0]\times10^{-13}$	s^{-1}
	Time of compression/extension before injection	$[10^{10},2\times10^{3},2\times10^{3},10^{10}$ $10^{10},10^{10},2\times10^{3},2\times10^{3},2\times10^{3}]$	s

Table 3.7: Numerical parameters and PETSc options employed in the simulations. For all of them we use line shear algorithm for SNES solver and FGMRES for KSP.

	Parameter	Value
Numerical resolution		128x64x128
Absolute convergence tolerance	-snes_atol	1x10^{-7}
Relative convergence tolerance	-snes_rtol	1x10^{-4}
Maximum number of iterations	-snes_max_it	100
Absolute convergence tolerance	-js_ksp_atol	1x10^{-14}
Relative convergence tolerance	-js_ksp_rtol	1x10^{-10}
Maximum number of iterations	-ksp_max_it	100
Multigrid preconditioner	–gmg_pc_levels	4

3.4 Discussion and conclusions

We presented a new 3D massively parallel software to model fluid injection and crack propagation in poro-visco-elasto-plastic rocks.

We benchmarked the code showing its ability to simulate the formation of localized shear and tensile zones in agreement with theoretical and experimental results, and its ability to reproduce the 2D failure patterns due to localized liquid overpressure proposed by other authors.

We study the influence of reservoir initial stress conditions on the propagation of failure zones and give a generalization for the 3D case of possible failure patterns generated by fluid injection.

In low stress conditions, failure zones develop in spheroidal shape propagating predominantly in the direction of the maximum and intermediate principal stresses, while, in high stress conditions, failures bifurcate in the plane defined by the minimum and the maximum principal stresses producing buttery-like shape oriented in the direction of the intermediate principal stress.

The aim of this work is to help with the interpretation and inference of geothermal project results, but the approach taken here has further application in other fields of geodynamics and volcanology as well, as the methodology has the potential to further increase the understanding of induced seismicity or aid in the interpretation of focal mechanisms during volcanic eruptions.

3.5 Acknowledgements

This project has received funding from the European Union's Horizon 2020 research and innovation program under the Marie Sklodowska-Curie grant agreement No 642029, CREEP.

We acknowledge J.M. Kendall and J. Verdon (University of Bristol) and T.S. Baumann (Johannes Gutenberg University of Mainz) for useful scientific

discussions.

The authors gratefully acknowledge the computing time granted on the supercomputer Mogon at Johannes Gutenberg University Mainz (hpc.uni-mainz.de).

Chapter 4

Numerical simulation of the hydraulic fracture for Well KM-8[1]

Abstract

To assess commercial potential, hydraulic fracturing is often used to stimulate flow in gas reservoirs. In order to guarantee the safe development of the projects, such actions require an accurate study of the geological structure of the reservoir in terms of stress conditions, hydraulic and mechanical properties and localization of faults and, furthermore, a good knowledge of the behavior of rocks under an increase of pore-pressure.

Here, to better understand the influence of the material permeability on the development of failure zones, we use the software LaMEM to simulate

[1]This chapter has been developed under the supervision of Michael Kendall[2], James Verdon[2] and Boris J.P. Kaus[3]

[2]School of Earth Sciences, University of Bristol, United Kingdom

[3]Institute of Geosciences, Johannes Gutenberg University of Mainz, Germany

the hydraulic stimulation of Well KM-8, located in PL080, North Yorkshire, UK. To do that, we use a model setup based on the Hydraulic Fracture Plan developed by the Company Third Energy and we perform numerical simulations considering different pre- and post-failure permeability values showing the importance of these parameters on the fracture geometry and growth.

4.1 Introduction

Hydraulic fracturing will be used to stimulate gas flow in Well KM-8, North Yorkshire, UK. To guarantee the safety development of the project, the company Third Energy developed a plan (Third Energy (2017)) with information about the techniques being used to monitor fracture propagation and to ensure that no fractures will extend beyond the permitted boundary. In this report, existing faults location derived from reflection seismic monitoring, a 1D geomechanical model along the KM8 well bore based on wireline log data, petrophysical analysis and borehole breakout, as well the expected fracture sizes and shapes from hydraulic fracture models are described.

In chapter 2 we presented the software tool LaMEM[2] (Lithosphere and Mantle Evolution Model), a scalable 3D parallel code to simulate geological processes such as fluid injection and crack propagation in poro-visco-elasto-plastic rheologies. In chapter 3 we used this code to study the strong influence of stress conditions on the propagation of failure zones generated by fluid injection. There, a fixed value for material permeability was used to perform the simulations and no change in material properties was considered after failure occurred.

In this chapter, with the aim to understand how permeability of materials, and its change after failure occurs, influences the propagation of fractures,

[2]See https://bitbucket.org/bkaus/lamem

we use LaMEM to perform the simulation of the hydraulic stimulation of Well KM-8.

First, we summarize the part of the hydraulic fracture plan for Well KM-8 presented in Third Energy (2017) used for our purpose. Next, we describe the numerical model setup used to reproduce the real setup afterwards we compare numerical simulations of fluid injection for different values of material permeability. Finally, we run a simulation considered an more extensive area around the Well KM-8.

4.2 Hydraulic fracture plan for Well KM-8[3]

Well KM-8 is located in PL080, North Yorkshire, UK and the company Third Energy seeks to study the risks associated with seismic events, monitor fracture height growth and fracture geometry and ensure that groundwater will be protected and that no fractures will extend beyond the permitted boundary due to developing the hydraulic fractures in the well. A map of the fault structure at 3040 meters depth is shown in Figure 4.1 and a seismic section of the area is shown in Figure 4.2.

In June 2013 the well was drilled as a vertical wellbore to a total measured depth of 10210 feets (3112 meters approximately). To investigate the stress regime of the area an analysis of borehole breakouts was performed and a 1D geomechanical model was generated based on wireline log data, petrophysical analysis and borehole breakout data. Figure 4.3 a) shows the stress conditions measured along the borehole.

Third Energy planned to conduct hydraulic stimulation at 5 different levels within the KM-8 well namely, at 3040, 2763, 2655, 2250 and 2126 meters depth injecting a water volume per zone of 424.90, 441.80, 474.90, 700.60 and 1248.90 cubit meters, respectively, with a fluid pumping rate of 4.8 to 8

[3]From Third Energy (2017)

cubic meters per minute. Frac stage levels are marked in figures by A to E where the E is the deepest stage.

Vertically, the fractures should not extend into the overlying Skipton Moor Grit Formation and, horizontally, the permit boundary is 400 meters from the KM-8 well.

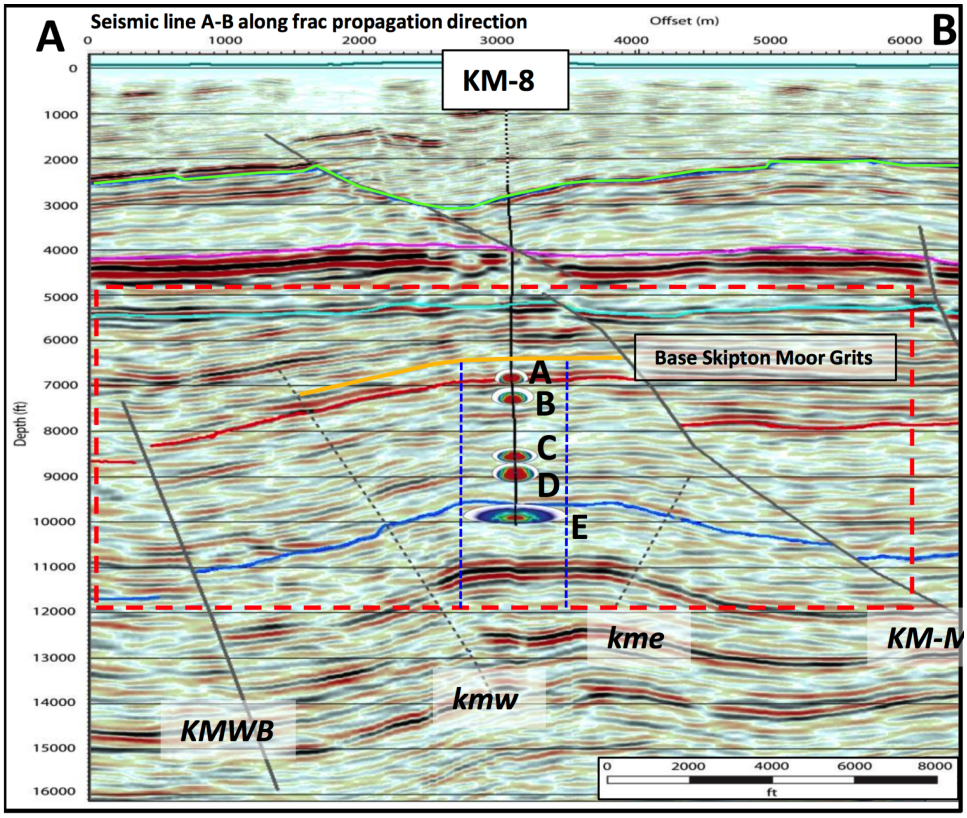

Figure 4.1: Figure 4-5 from Third Energy (2017). Seismic cross section through the KM8 well. The position of the section is marked on Figure 4.2. The NW-SE trend follows the expected fracture growth orientation. Mapped faults are marked with solid black lines, while smaller seismic disturbances are marked with dashed lines. The depth of the base Skipton Moor Grit is marked, as are the expected fracture dimensions for the 5 stages. The expected fracture geometries have been plotted indicating colors the proppant concentration within the fracture.

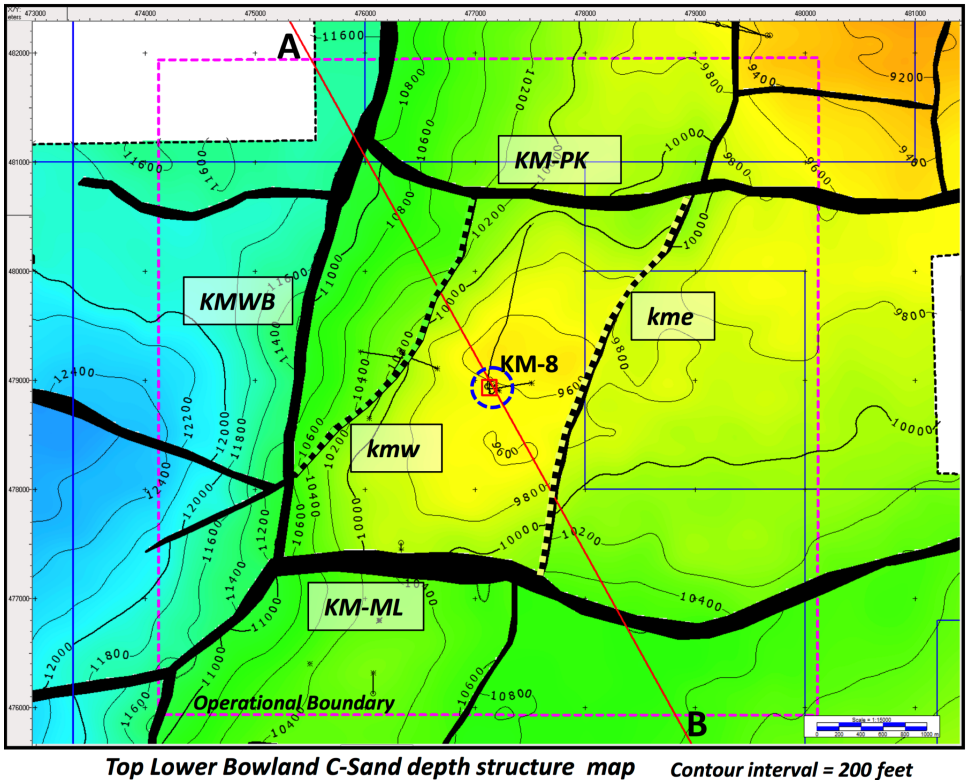

Figure 4.2: Figure from Third Energy (2017). Structural map at the HF stage E interval (deepest stage), derived from reflection seismic imaging. Mapped fault traces are marked in black, while smaller seismic disturbances are marked with black dashed lines. The operational boundary (see Section 5.4) is marked by the magenta dashed square.

4.3 Model Setup

To model the hydraulic stimulation of Well KM-8 we build a numerical setup with 1000 meters length, 50 meters width and 4000 meters height consisting of a homogeneous poro-visco-elasto-plastic domain with material properties and stress conditions based on those provided in Third Energy (2017).

In a following step, we simulate a bigger area that is 6000 meters long, 6000 meters wide and 4000 metres high domain, where four faults has been introduced according to the seismic cross-section and the structural map described in Figures 4.1 and 4.2.

To achieve the stress conditions of the well, as presented in Figure 4.3 a), we submit the model to lateral compression with respect to the x axis and to lateral extension with respect to the y axis by means a background strain rate of -0.97×10^{-13} s^{-1} and 2.8×10^{-14} s^{-1}, respectively. Figure 4.3 b) shows the resulting stress conditions for the numerical setup before injection starts. As studied in Chapter 3, if there is no bifurcation, the expected direction of propagation of fractures is the maximum stress direction followed by the intermediate stress which is the reason for the model size chosen for the more narrow setup. A sketch of the model setup and material properties are summarized in Figure 4.4 and Table 4.1, respectively.

To perform the simulations, we consider different values for material initial permeability $\kappa_0 = 10^{-19}$, 10^{-17} and 10^{-15} m^2 and different values $\kappa_f = 10^{-10}$, 10^{-11}, 10^{-12} and 10^{-13} m^2 for permeability in the areas where failure occurs. The post-failure value is assumed immediately after the failure.

We simulate the hydraulic stimulation of the well at levels A to E by introducing 5 liquid sources in the central vertical axis of the domain at 3040, 2763, 2655, 2250 and 2126 meters depth considering source magnitude 0.2 m^3/s for level A and, to maintain the relationship between the proposed volume per zone described in previous section, we use 0.208, 0.224, 0.33 and 0.588 m^3/s for levels B to E, respectively.

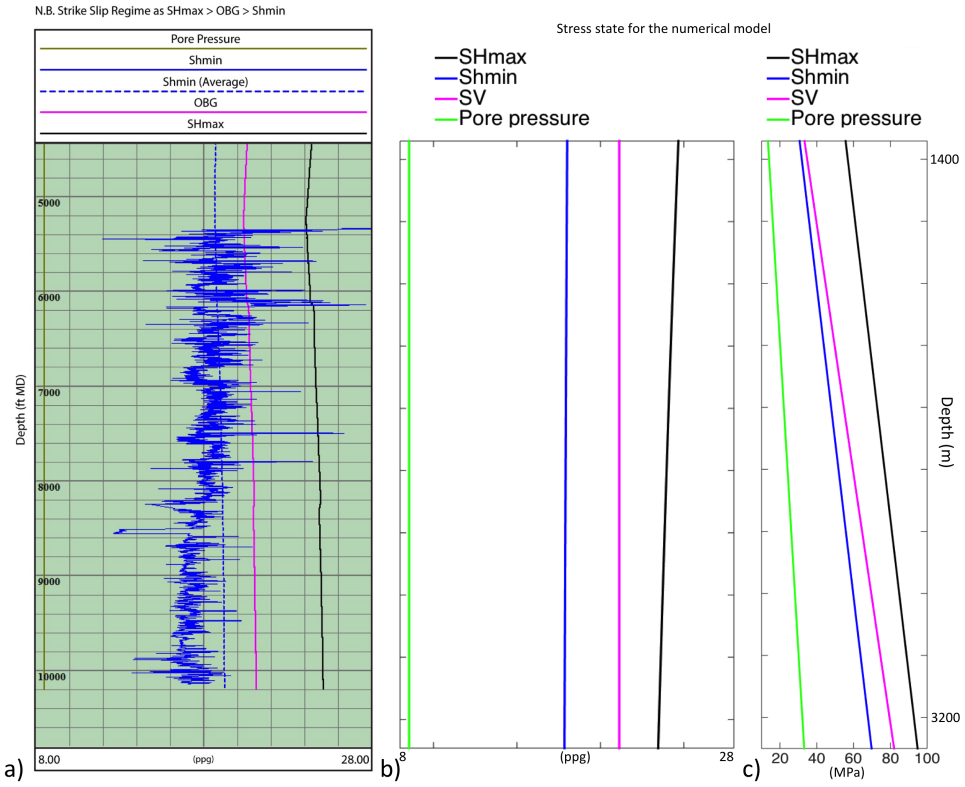

Figure 4.3: a) Figure 4-2 from Third Energy (2017) representing the 1D geomechanical model showing the stress conditions along the KM8 borehole. We show the estimated pore pressure (green), minimum horizontal stress (blue), maximum horizontal stress (black) and the overburden stress (pink). b) and c) show the stress-state of the numerical setup considered for the simulations in pounds per gallon (ppg) and in megapascals (MPa), respectivelly.

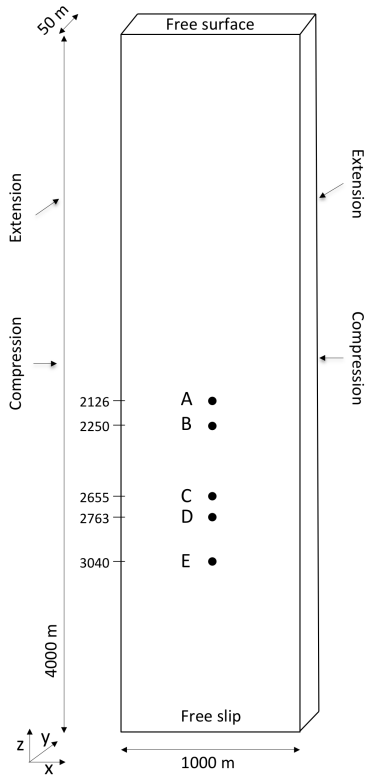

Figure 4.4: Model setup considered for the simulations of Well KM-8. As planned for KM8, we consider injection points at 5 levels (A to E) at 3040, 2763, 2655, 2250 and 2126 m depth, respectively.

Table 4.1: Physical parameters employed for the simulations of Well KM-8.

Variable	Parameter	Value	Units
ρ	Density	2470	kg m^{-3}
ρ_l	Liquid density	1000	kg m^{-3}
G	Shear module	2.66×10^{4}	MPa
ν	Poison's ratio	0.28	
C	Cohesion	40	MPa
ϕ	Friction angle	35	(°)
ψ	Dilation angle	10	(°)
σ_T	Tensile strength	20	MPa
κ_0	Permeability	$[10^{-19},10^{-17},10^{-15}]$	m^2
κ_f	Permeability after failure	$[10^{-10},10^{-11},10^{-12},10^{-13}]$	m^2
α_l	Matrix compressibility	1×10^{-10}	Pa^{-1}
β_l	Liquid compressibility	1×10^{-12}	Pa^{-1}
ϕ_l	Effective porosity	1×10^{-2}	
α	Biot-Willis constant	0.9	
$\dot{\varepsilon}_{xx}$	Background strain rate in lateral boundaries	-0.97×10^{-13}	s^{-1}
$\dot{\varepsilon}_{yy}$	Background strain rate in front boundaries	2.8×10^{-14}	s^{-1}
H_m	Source magnitude A-E	0.2, 0.208, 0.224, 0.33, 0.588	m^3s^{-1}
	Numerical resolution	[50×5×20,128×128×256]	

4.4 Results

First, we perform simulations in the model setup described by Figure 4.4 using the material parameters described in Table 4.1. We start considering initial permeability $\kappa_0 = 10^{-19}$ m^2 and permeability $\kappa_f = 10^{-12}$ m^2 for the areas where the failure occurs.

Figure 4.6 shows the fluid pressure and the second invariant of the deviatoric stress and strain rate after 1 hour of fluid injection and Figure 4.6 the resulting failure areas. To see the evolution of fractures we plot in Figure 4.7 the resulting failure areas after 1, 3 and 5 hours of fluid injection observing that, as expected from the stress conditions, the predominant propagation direction of fractures is the maximum principal stress (x axis) followed by the intermediate principal stress (vertical).

Influence of initial permeability value

To understand the influence of the material permeability on the development of fractures around the injection points we run simulations using initial permeability values $\kappa_0 = 10^{-15}$ and 10^{-17} m^2 and, for comparison, we plot in Figure 4.8, together with the previous result for $\kappa_0 = 10^{-19}$ m^2, the resulting failure areas after 5 hours of simulation.

We can see that the failure areas are smaller for the case of the greater permeability ($\kappa_f = 10^{-15}$ m^2) which can be explained since a higher permeability allows a higher flow of fluid and then a lower local pore-pressure and, therefore, a lower failure area. For the case of $\kappa_0 = 10^{-17}$ m^2 we observe that fracture length is slightly greater than in the case of $\kappa_0 = 10^{-19}$ m^2 while the height is greater for the lower permeability case, which may be because a very high local pore-pressure causes a more rapid propagation of in the non-preferred direction.

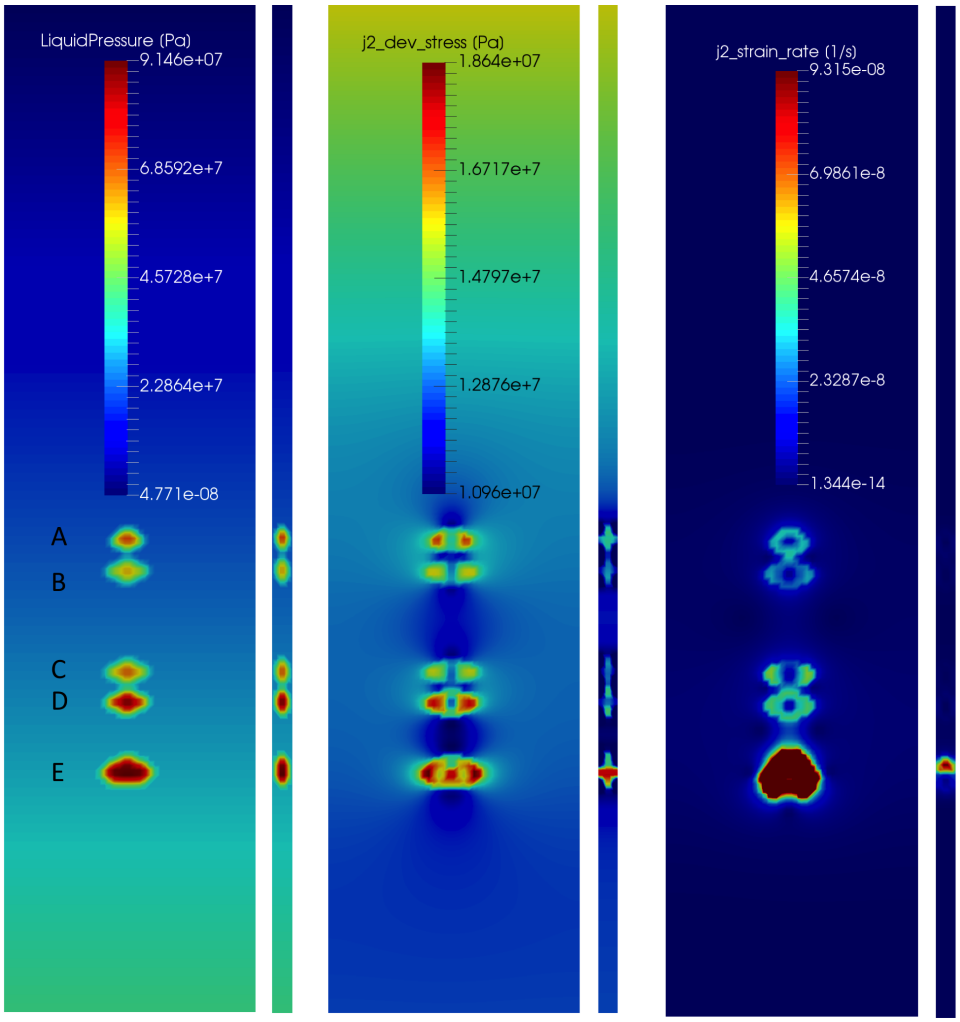

Figure 4.5: Simulation of hydraulic fracturing considering an initial permeability $\kappa_0 = 10^{-19}$ m^2 and post-failure permeability $\kappa_f = 10^{-12}$ m^2 after 1 hour of fluid injection. Figure shows the liquid pressure (left), second invariant of the deviatoric stress (center) and second invariant of the strain rate (right). For every case we plot two vertical slices of the model through the injection points in the x and y direction.

Influence of post-failure permeability value

Here, we perform simulations fixing the initial permeability as $\kappa_0 = 10^{-19}$ m^2 and, for the post-failure stage, different permeabilities $\kappa_f = 10^{-10}$, 10^{-11}, 10^{-12}, 10^{-13} m^2. We can observe in Figure 4.9 the significant influence of the

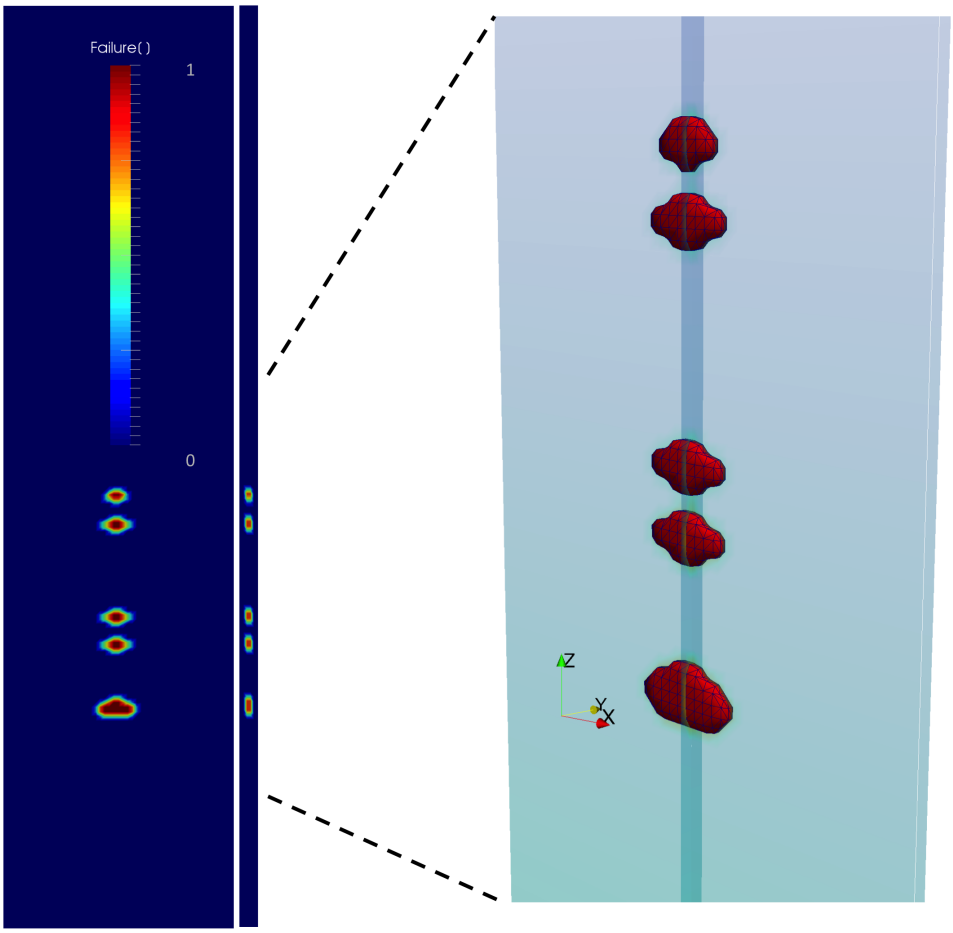

Figure 4.6: Failure areas corresponding to the simulation in Figure . On the left we plot failure areas by means two vertical slices of the model setup through the injection points in the x and y direction and, on the right we show a zoomed 3D view of the resulting fractures.

permeability change of rocks on the fracture shape and propagation. The more the permeability increases after failure, the higher the length and the shorter the height of the failure area.

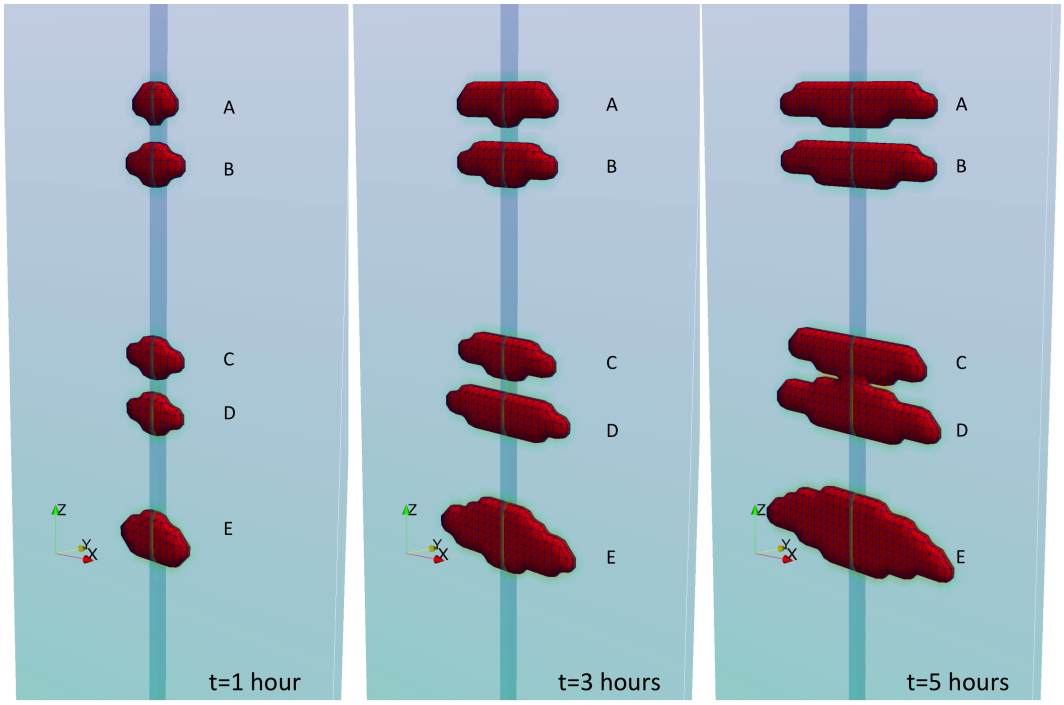

Figure 4.7: Simulation of hydraulic fracturing considering an initial permeability $\kappa_0 = 10^{-19}$ m^2 and post-failure permeability $\kappa_f = 10^{-12}$ m^2, indicating first, second and third columns the resulting failure areas after 1, 3 and 5 hours, respectively, of fluid injection.

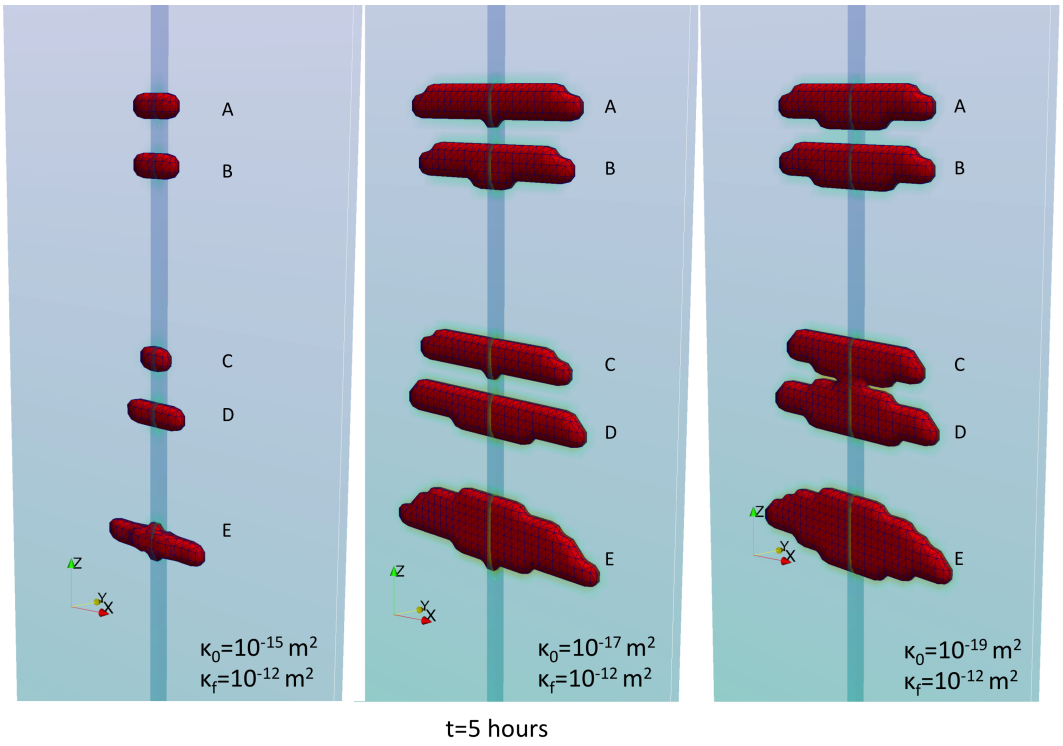

Figure 4.8: Failure areas after 5 hours of fluid injection corresponding to simulations considering initial permeabilities $\kappa_0 = 10^{-15}$ (column 1), 10^{-17} (column 2) and 10^{-19} (column 3) m^2 and post-failure permeability $\kappa_f = 10^{-12}$ m^2.

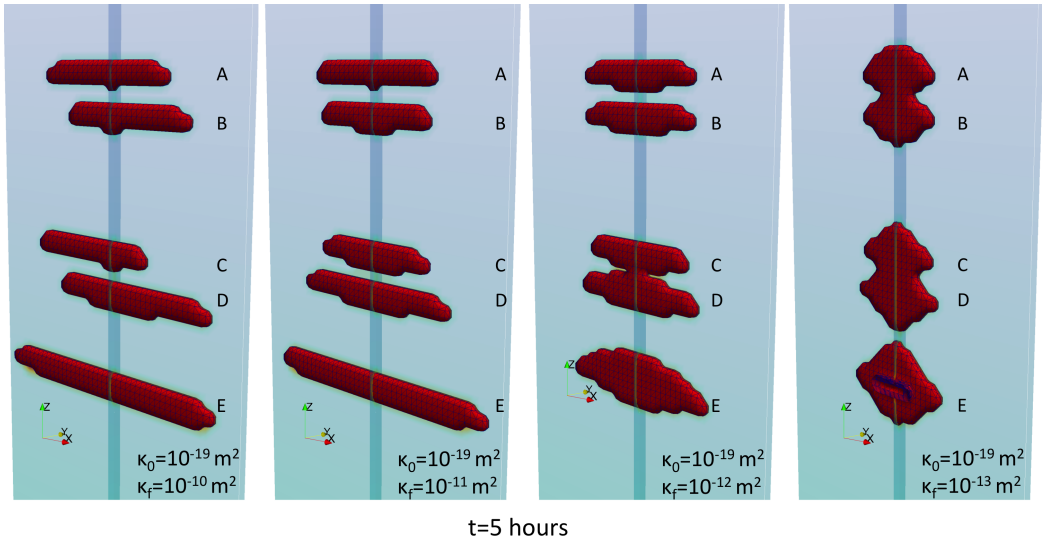

Figure 4.9: Failure areas after 5 hours of fluid injection corresponding to simulations considering initial permeability $\kappa_0 = 10^{-19}$ and permeabilities $\kappa_f = 10^{-10}$ (column 1), 10^{-11} (column 2), 10^{-12} (column 3), 10^{-13} (column 4) m^2 for the areas where failure occurs.

Finally, we run a simulation in the model setup with 6000 meters length, 6000 meters width and 4000 meters height with faults as described in Figures 4.1 and 4.2. We consider $\kappa_0 = 10^{-16}$ m^2 for the initial permeability of rocks and $\kappa_f = 10^{-10}$ m^2 for post-failure permeability. For the faults, we use higher permeability $\kappa_0 = 10^{-11}$ m^2 and lower values for the cohesion and tensile strength of 5 MPa and 2 MPa, respectively. We inject fluid at the 5 levels with source magnitudes 0.5 m^3/s for A to D and 1 m^3/s for level E.

Figure 4.10 shows the results after 9000 seconds of fluid injection. The colours indicate the value of the permeability and the arrows the direction and velocity of the fluid. We observe that the general trend is to flow downward, as expected by the stress conditions, and to flow through the faults, since there the permeability is greater. Also, the fluid flow points out around the 5 injection points due to high pressure injection.

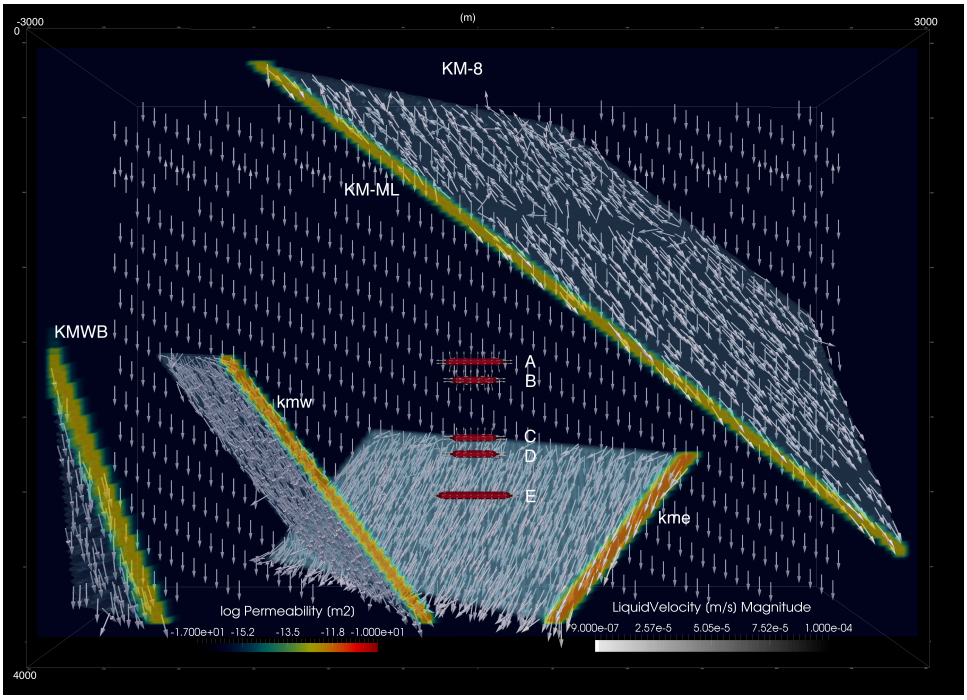

Figure 4.10: Simulation of the hydraulic stimulation of Well KM-8 after 9000 seconds of fluid injection in a model setup where faults have been including based on the fault structure map described in Figure 4.1 and the seismic section in Figure 4.2.

4.5 Conclusions

We used the software LaMEM to perform numerical simulations of fluid injection by reproducing the hydraulic stimulation for Well KM-8 presented in Third Energy (2017). We presented results using different values for initial material permeability and considering different values for permeability in areas where failure occurred. We observe a considerable influence of these parameters on the development of failure areas concluding that the knowledge of the permeability of rocks and how it changes after fracturing is crucial for the correct development of hydrofracturing projects.

4.6 Acknowledgements

This project has received funding from the European Union's Horizon 2020 research and innovation program under the Marie Sklodowska-Curie grant agreement No 642029, CREEP.

We acknowledge J.M. Kendall and J. Verdon (University of Bristol) for the feedback received during the secondments in University of Bristol.

The authors gratefully acknowledge the computing time granted on the supercomputer Mogon at Johannes Gutenberg University Mainz (hpc.uni-mainz.de).

Chapter 5

Numerical simulation of non-invasive seismic monitoring of a radioactive waste repository[1]

Abstract

A deep circular tunnel whose backfill changes over time due to temperature, water saturation, pressurization and compaction could be a possible scenario to house a nuclear waste deposit. To obtain information about the internal estate of the repository after backfilling and closing is finalized, in a non invasive way, remote active seismic methods are used to try to un-

[1]This chapter has been developed under the supervision of Katrin Plenkers[2], Boris J. P. Kaus[3] and Thomas Spillmann[4] and will be part of a future publication together with the analysis of the real waveforms

[2]Gesellschaft für Materialprüfung und Geophysik, Germany

[3]Institute of Geosciences, Johannes Gutenberg University of Mainz, Germany

[4]NAGRA, Nationale Genossenschaft für die Lagerung radioaktiver Abfälle , Switzerland

derstand how the above elements are reflected in the signals recorded at the seismic network. These signals hold information on the material properties and, therefore, on changes in the intrinsic properties of the backfill. Here we performed numerical simulations of wave propagation with the aim of increasing our ability to understand path effects and, therefore, to understand the situation inside the repository over time. We apply our results on the Full-Scale Emplacement Experiment at the Mont Terri underground rock laboratory. This experiment is being developed by the National Cooperative for the Disposal of Radioactive Waste Switzerland (NAGRA) and the Society for Materials Testing and Geophysics (GMuG) has been hired to perform active seismic transmission monitoring.

5.1 Introduction

In the mid-20th century nuclear industries started to be developed generating since then thousands of tones of highly radioactive wastes. Some of such wastes remain a danger to living organisms during millions of years. Therefore, radioactive waste management and save disposal is a concern that must be scientifically investigated as thoroughly as possible. One of the widely accepted solutions currently under investigation is placing nuclear waste in repositories below the surface to minimize releases of the contained radioactivity into the environment. For this purpose, full-scale emplacements tests are being conducted to simulate the construction, waste emplacement, backfilling and early post-closure evolution of disposal tunnels for high-level radioactive waste. Numerous investigations about the physical and chemical properties of the materials involved in such experiments have been done (e.g. Gens et al. (2002), Seiphoori (2014), Siegesmund et al. (2014), Bohlen et al. (2015), Biryukov et al. (2016), Apted & Ahn (2017), Bossart (2017)). Nagra implemented the Full-scale Emplacement (FE) Experiment at the Mont Terri underground rock laboratory (URL) (Müller et al. (2018)). This experiment is a full-scale heater test in the clay-rich shale Opalinus Clay. Electrically powered heater elements simulate the heat prodeced by a spent fuel (SF)

high-level waste (HLW) canister disposed in a repository tunnel according to the Swiss disposal concept. In the experimental tunnel about 250 m below surface three heaters, with a heat output and dimensions similar to those of waste canisters, are emplaced on top of pedestals built of bentonite blocks. The surrounding space is backfilled with granular bentonite, a material currently considered to be an option for backfilling due to its favorable hydraulic and chemical properties. After backfilling, the system is heated and monitored for several years to decades.

The monitoring system in a real repository should not be intrusive so as not to compromise the sealing of the site. For this reason, seismic measurements from boreholes surrounding the disposal tunnel have been identified as a useful option to monitor such installations (e.g. E Manukyan (2012)). The requirements for demonstration tests can be less restrictive and allow monitoring devices inside the backfilled volume. In case of the FE, the company GMuG was responsible to develop, install and operate acoustic transmitters and receivers for monitoring elastic properties in the granular bentonite backfill. Sensors from typically passive Acoustic Emission (AE) technology were adapted to the excite or record seismic signals. The sensors were then mounted on steel frames and attached to the tunnel wall before the tunnel was backfilled with granular bentonite.

The signals recorded show a complex wavefield due to the acquisition geometry inside the cylindrical disposal tunnel. Additionally the wavefield varies in time since the elastic properties of the backfill depend on temperature, water saturation, pressurization and compaction, all of which are influenced by the heater. This complexity, as well as a lack of knowledge of the internal processes, makes the interpretation of the collected signals challenging.

Numerical modelling is used in this work in order to help answer questions such as: Which wave types are present in a cylindrical tunnel geometry? Which are the dominating ones? What processes influence waveform amplitude and attenuation? How do the waves and recorded signals vary over time?

Here, we use the software SOFI2D to make numerical simulations to investigate seismic wave propagation inside the FE tunnel considering realistic material properties. We apply this study to the Full-Scale Emplacement (FE) Experiment at the Mont Terri underground rock laboratory (URL), Switzerland.

5.2 Real setup

In September 2012 the construction of the tunnel for the FE experiment was completed. This tunnel is 50 m long and has a diameter of 3 m and is supported at the deep end by steel arches and by shotcrete in the rest of the tunnel. The test section, where the three electrical heaters were emplaced, the tunnel was backfilled with granular bentonite and sealed with a five meter long concrete plug. In order to detect and monitor changes in the backfill density, two seismo-acoustic sensor arrays in the bentonite backfill were installed by GMuG: one permanent array directly inside the bentonite backfill and one temporary array in two observational pipes near the tunnel wall inside the bentonite backfill. The arrays are focused to the area next to heater H3, gallery meter (GM) 17.50 m (figure 5.1), where gradual changes of saturation and temperature are expected.

Each array implements transmitters as well as receivers for the recording of such signals. The acoustic sensors (sources) produce an (ultra-)sonic signal with a maximum voltage of 1200 V and consist of piezoelectric elements inside a housing made of brass designed for the temperatures and pressures expected within the FE experiment. Acoustic receivers have external preamplifiers of over 30dB to compensate for signal attenuation in the cable that connects the receiver with the acquisition unit. The permanent network incorporates five acoustic emission (AE) receivers and three acoustic emission transmitters. The temporary network incorporates one addition transmitter and eight additional receivers. All sensors were developed and manufactured

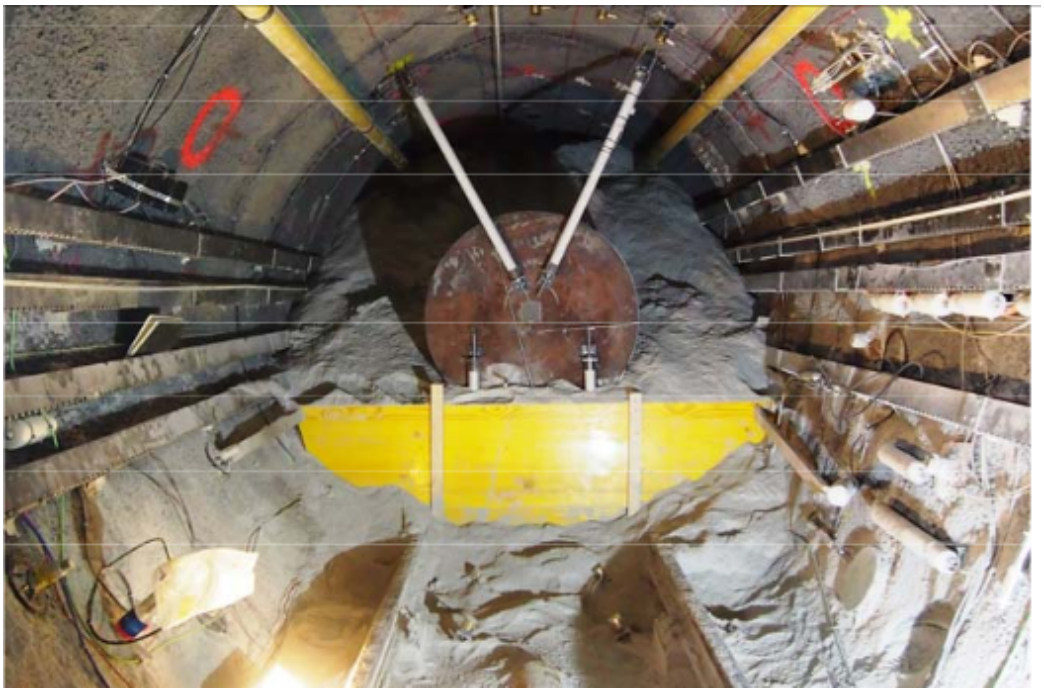

Figure 5.1: Picture from Spillmann & Philipp (2015). Photography of FE tunnel at approximately GM 17.0 m, view onto partly backfilled heater H3. The two seismic arrays are visible at the tunnel floor between the rails and at the roof.

by GMuG Bad Nauheim. Coordinates of source and receivers can be found at Tables A.1 and A.2 (Spillmann & Philipp (2015)) or at figure 5.A1 in Apendix 5.7. More details about the geophysical monitoring and installation of acoustic sensors for the FE Experiment can be found at Spillmann & Philipp (2015) as well.

5.3 Numerical method

The equations that describe waves in isotropic elastic medium, in its stress-velocity formulation, are given as following:

$$\rho \frac{\partial v_i}{\partial t} = \frac{\partial \sigma_{ij}}{\partial x_j} + f_i \tag{5.1}$$

$$\frac{\partial \sigma_{ij}}{\partial t} = \lambda \frac{\partial \theta}{\partial t} \delta_{ij} + 2\mu \frac{\partial \varepsilon_{ij}}{\partial t}, \tag{5.2}$$

$$\frac{\partial \varepsilon_{ij}}{\partial t} = \frac{1}{2} \left(\frac{\partial v_i}{\partial x_j} + \frac{\partial v_j}{\partial x_i} \right), \tag{5.3}$$

where t is time, v_i is the velocity vector, σ_{ij} and ε_{ij} are the stress and strain tensor, respectively, θ is dilation, ρ is density, λ and μ are the Lamé parameters and f_i are body forces. The indices i denote the coordinates in the Cartesian axis.

Viscoelastic effects can be include by implementing an absorption mechanism based on the rheological model GSLS (generalized standard linear solid) (e.g. Bohlen (2002), LiU et al. (1976)). Such as model consists in a spring connected in parallel with L Maxwell bodies composed each of them by a spring and a dashpot connected in series. The elastic moduli and the viscosities of these elements determine the seismic quality factor Q describing the attenuation properties of rocks.

To carry out our simulations we use the software Sofi2D, a viscoelastic forward modelling code that solves these equations by using the finite differences method in a 2-D Cartesian standard staggered grid and uses the message passing interface to distribute the calculations in parallel.

5.3.1 Model

We want to simulate the propagation of the waves inside the cross-section of the FE tunnel at 17.5 m GM. The numerical setup for the simulation has been deducted from Spillmann & Philipp (2015) (Appendix 5.7) producing the model showed in figure 5.2. This model is composed by a circular tunnel of 2.80 meters internal diameter with a wall of shotcrete of 0.20 meters thickness inside the opalinus clay. Coordinates of FE source S1 and FE receivers used in the simulations can be found at Table 5.A1 in Appendix 5.7. For our

simulations we increase the number of synthetic seismic stations adding 24 recorders distributes around the perimeter of the bentonite and located at 1.23 meters from the centre of the tunnel. Stations are pointing towards the centre of the tunnel, therefore, a rotation of the coordinate axis for each receiver is needed in order to get the correct components of the velocity field (more information about the choice and transformation of the coordinates can be found in Appendix 5.7.1).

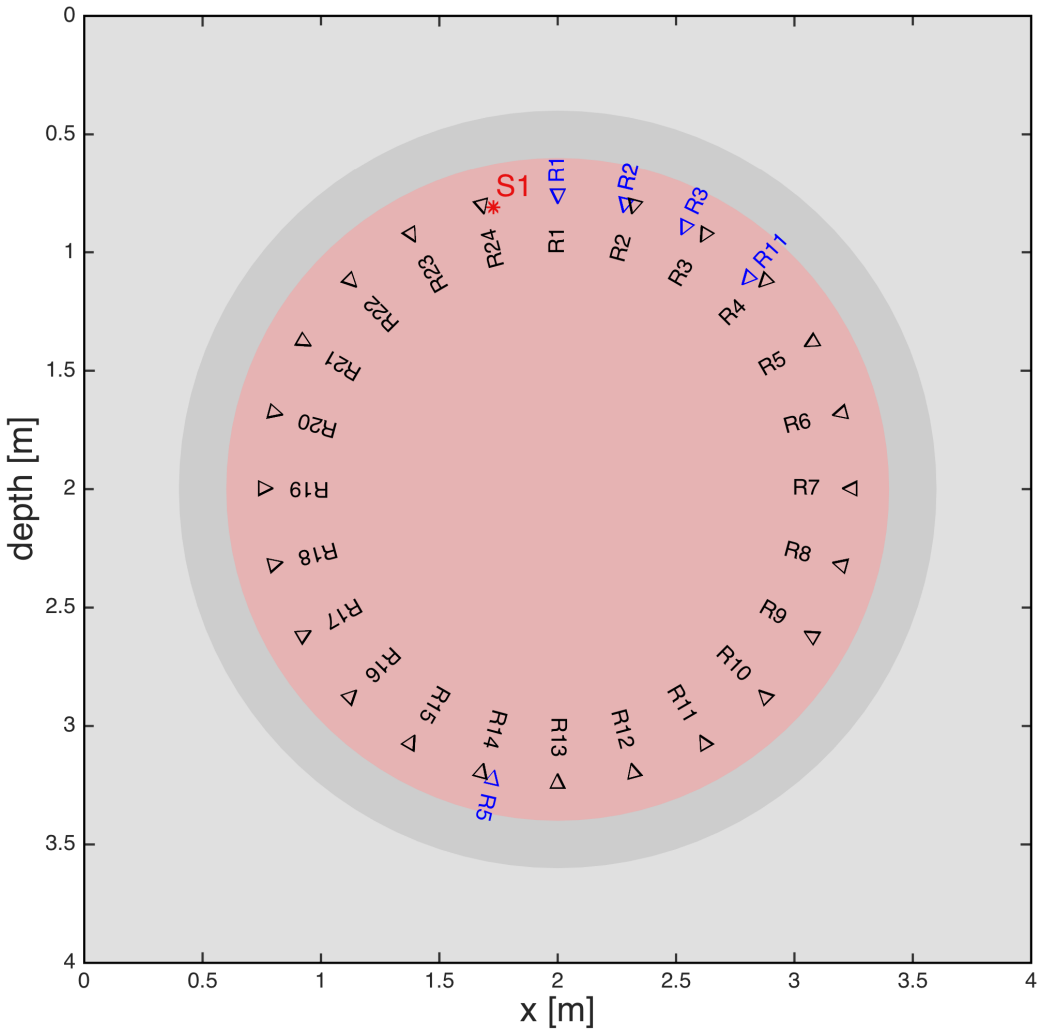

Figure 5.2: Numerical model representing the cross-section of the FE tunnel at 17.5 m GM. This model is composed by a 4x4 meters setup with two concentric circles with ratios 1.40 and 1.60 meters. We consider the properties of the bentonite for the interior of the smaller circle, the properties of shotcrete for the region between circles and the properties of opalinus clay for the exterior area (Table 5.1 shows the numerical properties for each material). The source (S1) is denoted by red asterisk, the synthetic seismic stations simulating the FE-recorders R1, R2, R3 and R11 by blue triangles and the added-stations R1 to R24 by black triangles. Although we observed that the real FE-receivers in the floor are not located in the cross-section under investigation, we show the FE-receiver R5 in the model being that is the closer one but we point that it is behind the cross-section.

In order to represent the AE sensor recording we took into account that, unlike one-component geophones or seismometers, AE sensors are not only sensitive in one direction. The piezoelectric element of AE sensors reacts both to stress changes in vertical direction and horizontal direction. For this reason we join the horizontal and vertical components of the computed seismograms by performing the weighted arithmetic mean giving double importance to the vertical component. The reason for that is because AE sensors are more sensitive to stress changes in the direction orthogonal to the sensors coupling plane, because stress changes leading to changes in the piezoelectic element length give a stronger output than changes in the elements width.

The source that we use to generate the signals is a Gaussian pulse wavelet with frequencies from 0 to 6000 Hertz (figure 5.3), located in the upper part of the bentonite at 0.179 meters distance from the shotcrete. This source, as in the case of receivers, is pointing to the centre of the tunnel, therefore, an angle of 167 degrees with respect to the azimuth has been considered.

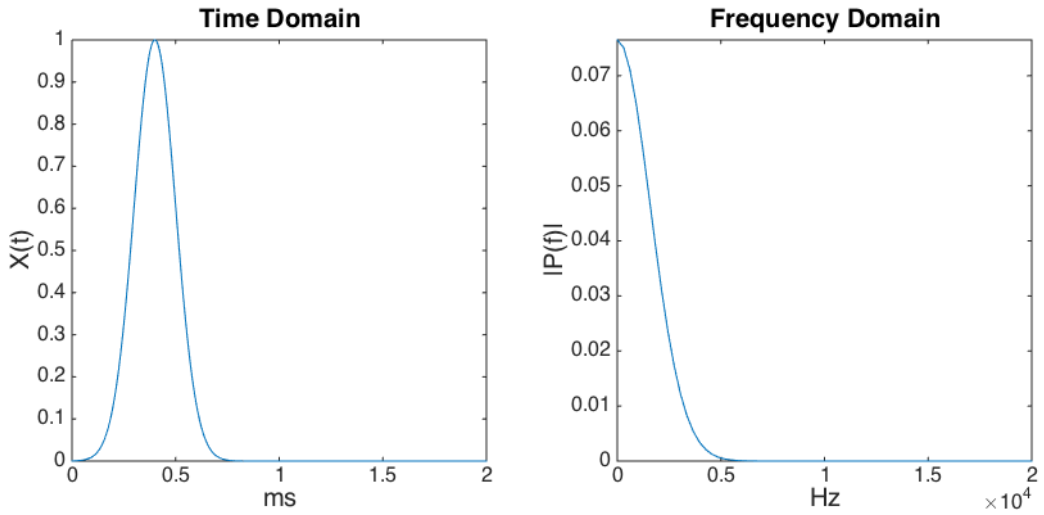

Figure 5.3: Source wavelet in time and frequency domain used in the simulations.

Seismic properties considered for the three faces of our model come from various sources of information (Table 5.1). For the shotcrete, density and seismic velocities have been deduced from Wetzig & Reinhold (2014) and quality fac-

tors for P and S waves were provided by Prof. Dr. Hansruedi Maurer, ETH. Density of opalinus Clay is from Bossart (2017) and velocities and attenuation from advise of Prof. Dr. Hansruedi Maurer, ETH during a meeting in NAGRA. For bentonite, density and attenuation are from Biryukov et al. (2016) and seismic velocities are derived from the observed velocities in the real FE experiment (Plenkers et al. (2017)). These seismic velocities differ from measurements in laboratory (e.g. Biryukov et al. (2016)) probably due to, for instance, different bentonite material, different compaction or different humidity.

Table 5.1: Model parameters.

	Opalinus	Shotcrete	Bentonite
$V_p[m/s]$	2500[1]	2422[3]	290[5]
$V_s[m/s]$	700[1]	1398[3]	148[5]
Density $[g/cm^3]$	2450[2]	2209[3]	1620[4]
Q_p	200[1]	50[1]	19[4]
Q_s	180[1]	40[1]	10[4]

1 Personal communication with Prof. Dr. Hansruedi Maurer, ETH.

2 Bossart (2017)

3 Wetzig & Reinhold (2014)

4 Biryukov et al. (2016)

5 Plenkers et al. (2017)

To avoid grid dispersion and numerical instabilities the grid space is set to 10^{-3} m and the time step to 10^{-7} seconds. For the viscoelastic simulation we use one relaxation mechanism with a relaxation frequency of $FL1 = 3000Hz$ and $\tau = 0.1$ (Bohlen (2002)).

5.3.2 Results

With the aim to understand the relative effect of each of the elements of the model on the synthetic signals, elastic and viscoelastic simulations, for

homogeneous and tunnel models are carried out. Finally, a viscoelastic simulation considering depth-dependent seismic velocities for bentonite backfill has been done.

Elastic simulation in homogeneous model

We start performing a simulation in an elastic isotropic homogeneous model with the properties of bentonite to understand the basic behaviour of a seismic wave. As is known, after a source is applied in the interior of a material, two types of waves start travelling through it. The P-wave, that moves in the direction of the wave propagation, and the S-wave, that moves slower and perpendicularly to the direction of propagation. Sofi2D calculates the divergence and the curl of the particle velocity field to plot separated snapshots for P- and S-waves. Figure 5.4 clearly describes, as expected, the symmetry of P-wave and the polarity of S-wave with respect to the direction of propagation. This direction is the defined by the location of the source and the center of the tunnel since the source is a force pointing to the center of the tunnel. We show in Figure 5.5 seismograms recorded at synthetic stations during the first 25 microseconds of simulation where we recognize easily the signals corresponding to the arrivals of the direct P- and S-waves. These P- and S- arrivals, calculated analytically, are marked by the letters P and S, respectively, in the figure.

Elastic simulation in tunnel model

Following, we perform a simulation in the tunnel model. Figure 5.6 shows the comparison between seismograms for this simulation and the corresponding seismogram in the homogeneous case. We can observe that the arrivals of P- and S- waves coincide in both cases but in the case of the tunnel model more signals appear in the seismograms due to the distortions of waves by the new setup. Snapshots corresponding to every 24 milliseconds of simulation can be found in Appendix 5.7 (Figure 5.A6 to 5.A14). Plotting some of the snap-

shots highlighting low velocity values (Figure 5.7) we can observe that, when the waves reach the shotcrete, most of its energy returns to the bentonite generating the reflected waves. The energy that enters in the shotcrete produces the transmitted waves and the energy that travels along the interface produces the head wave that propagates around the interface between the two materials with the velocity of the shotcrete. Each phenomena of reflection and transmission of a P- or a S-wave generate its corresponding converted S- or P-wave, respectively. In order to analyze the recorded signals globally and localize which of the above elements are the most influential on them we plot the seismograms normalized by the maximum velocity amplitude of all the signals (Figure 5.8). Nomenclature to refer to each of the waves can be found at Table 5.2. In Figure 5.8 we localize, surrounded by colors, the different waves. For instance, recorded by station R24, the closest to the source, we can see, after the direct waves, the pcP in yellow, the pcS in purple and the scS in green and, towards the end, some traces due to the waves reflected in the ground and going back up (orange). For the other stations, in between the direct arrivals, we observe the pcP (yellow) and the scP (grey), and, for the stations closest to the ground, the interaction between P-waves coming down and P-waves coming up (dark orange). Signals with the bigger amplitude are due by scS (green) for the upper recorders. As the waves propagate downwards new waves appear generating 2 and 3 in Figure 5.9 and producing the signals with the highest amplitude for receivers R6 to R11 and R14 to R18 (blue and red). In the sensors furthest from the source, signals due to the crossing between S-waves that descend and the S waves that return (pink) can be observed in the last milliseconds.

Table 5.2: Nomenclature used to define the different waves.

p	direct P-wave coming up from the source
P	direct P-wave coming down from the source
s	direct S-wave coming up from the source
S	direct S-wave coming down from the source
pPr	transmitted p in the shotcrete
pSr	transmitted p in the shotcrete converted to S-wave
pcP	p reflected in the shotcrete (P-wave)
scS	s reflected in the shotcrete (S-wave)
scP	s reflected in the shotcrete converted to P-wave
pcS	p reflected in the shotcrete converted to S-wave
HP	head waves in general (P-waves)
HS	head waves in general (S-waves)
Pcp	P reflected in the shotcrete going back to the source

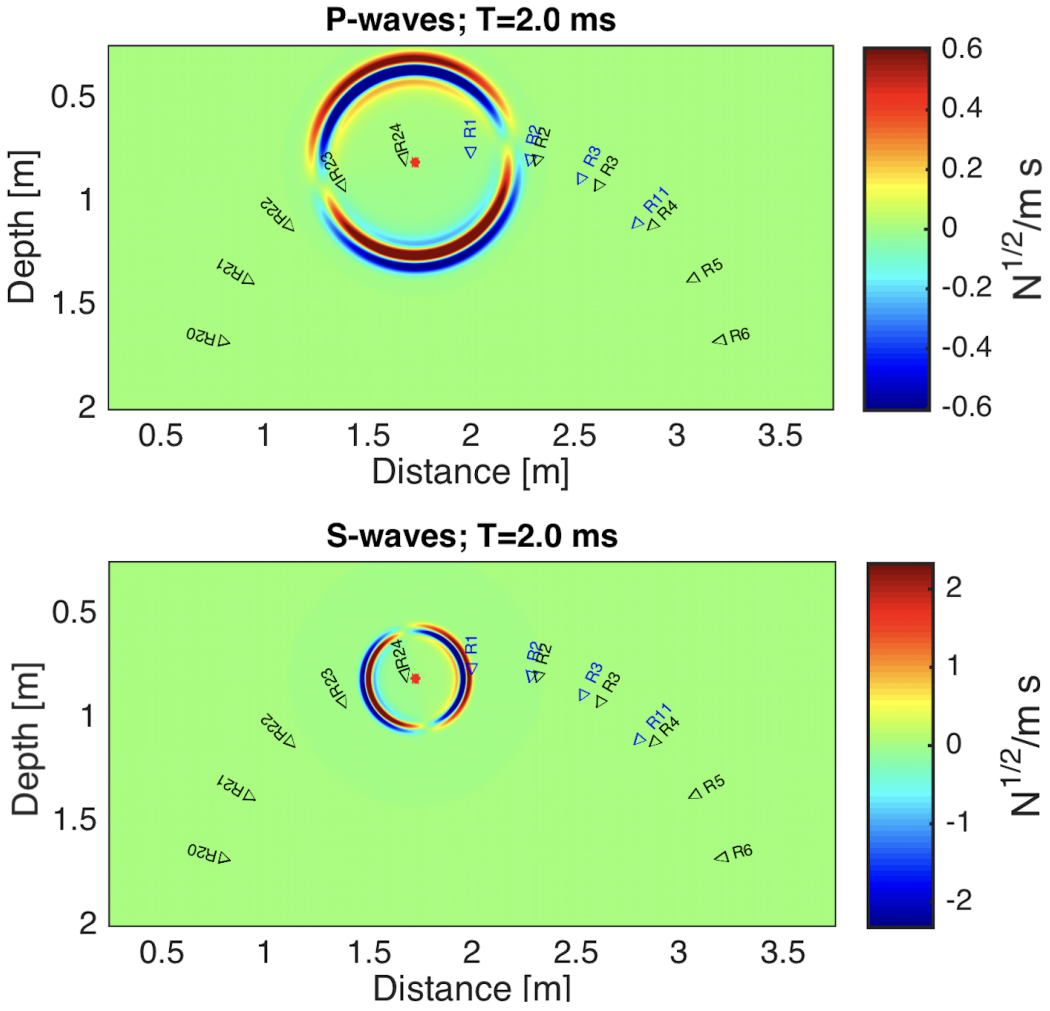

Figure 5.4: Snapshots at 2 milliseconds of the elastic simulation in homogeneous model with the properties of bentonite. Plots are proportional to the magnitudes of the P- and S- particle velocities and signs are those of divergence and curl, respectively.

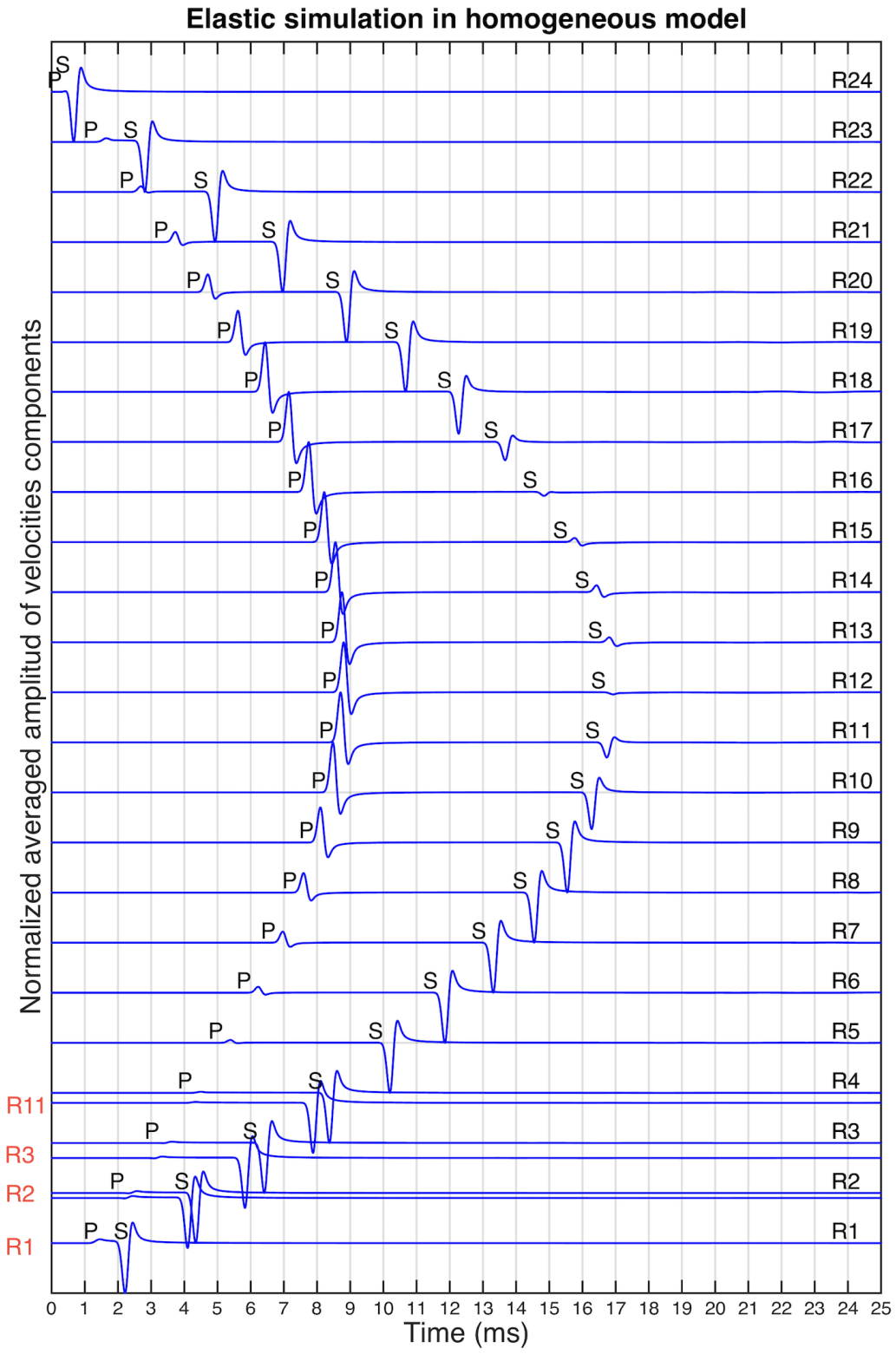

Figure 5.5: Velocity seismograms collected by FE- (red) and added- (black) recording stations corresponding to an elastic simulation in a homogeneous model with the properties of bentonite. Signals represent the weighted arithmetic mean of the horizontal and vertical velocity components considering weights of 1 and 2, respectively. Signals waveforms are individually normalized. Letters P and S represent the analytically calculated time arrivals to each station of the P- and S- waves, respectively, travelling through bentonite.

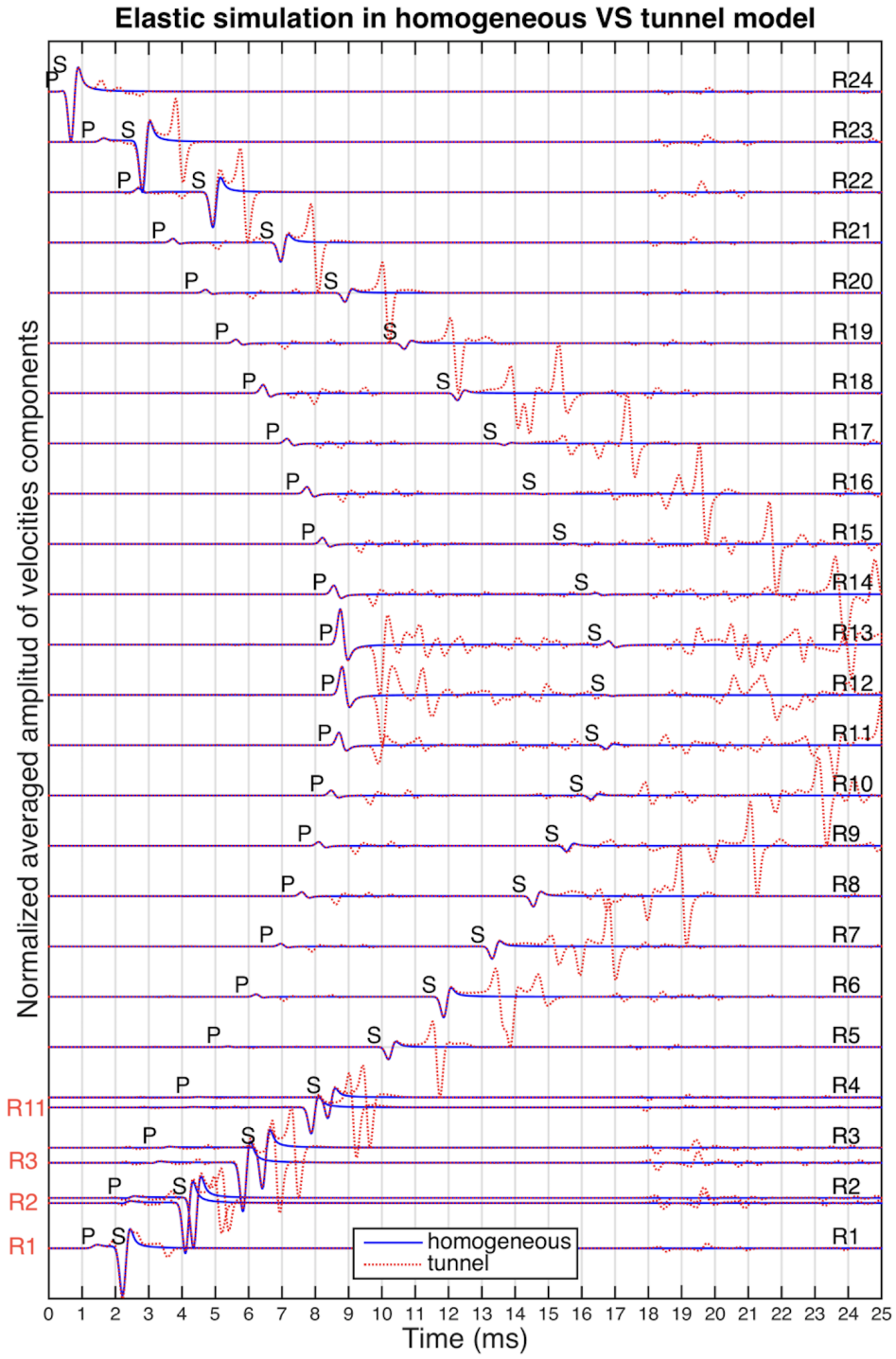

Figure 5.6: Velocity seismograms collected by FE- (red) and added- (black) recording stations corresponding to both, an elastic simulation in a homogeneous model with the properties of bentonite (blue traces) and an elastic simulation in a tunnel model (red traces) as Figure 5.2. Signals represent the weighted arithmetic mean of the horizontal and vertical velocity components considering weights of 1 and 2, respectively. Both signals for every station are normalized together. Letters P and S represent the analytically calculated time arrivals to each station of the P- and S- waves, respectively, travelling through bentonite.

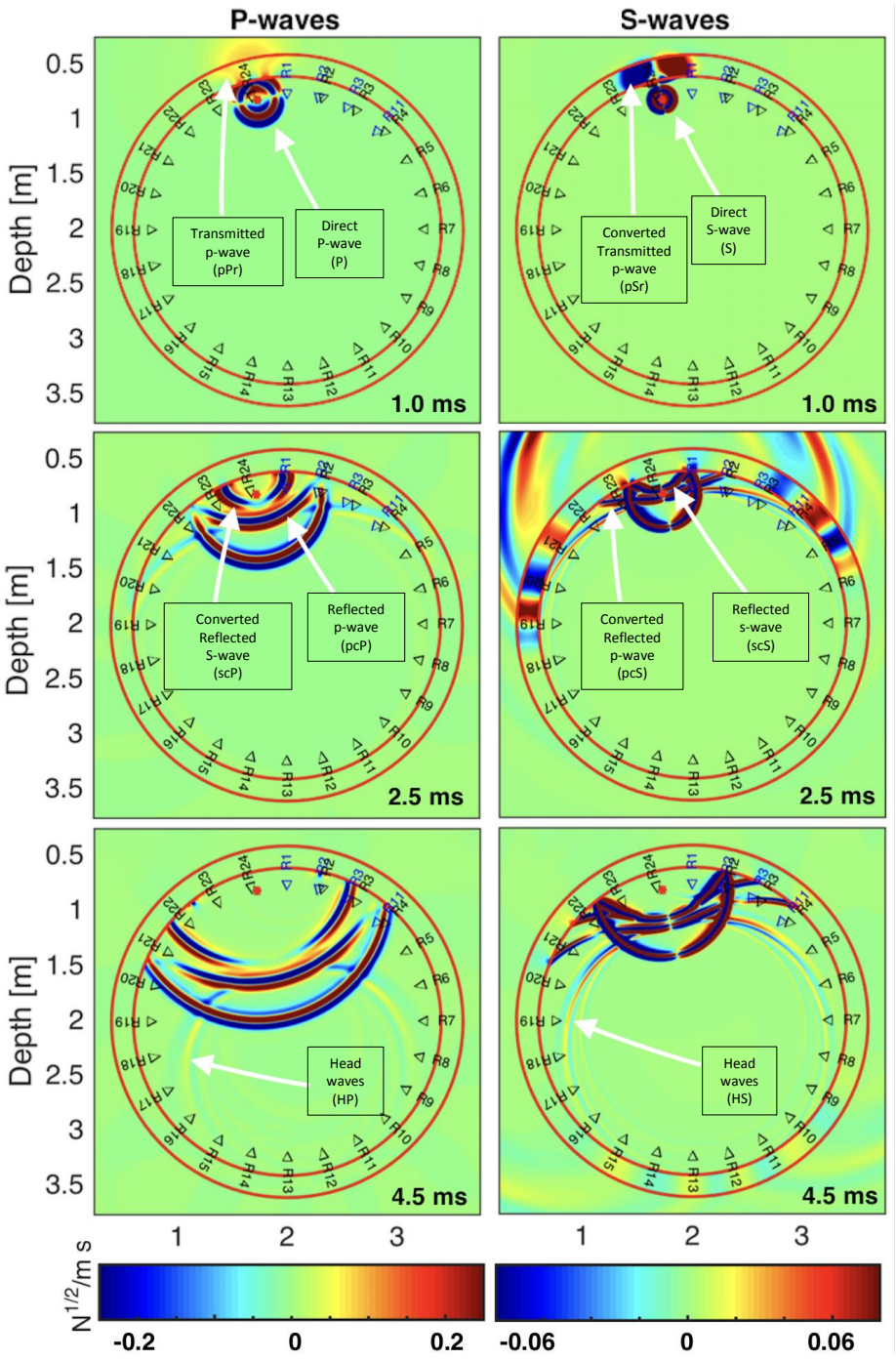

Figure 5.7: Snapshots at 1, 2.5 and 4.5 milliseconds of the elastic simulation in the tunnel model. Plots are proportional to the magnitudes of the P- and S- particle velocities representing signs the divergence and curl sign information, respectively.

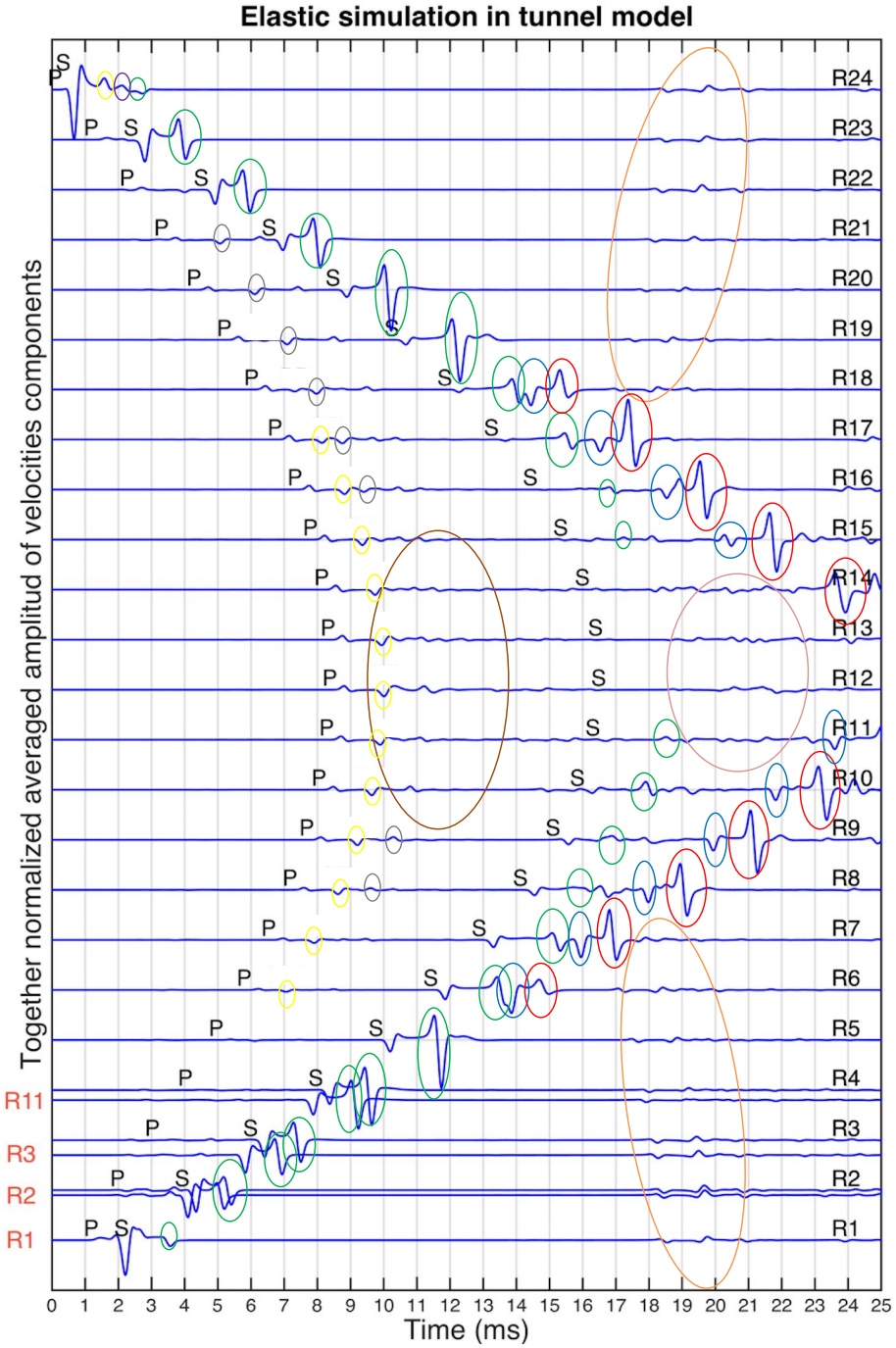

Figure 5.8: Velocity seismograms collected by FE- (red) and added- (black) recording stations corresponding to an elastic simulation in a tunnel model as Figure 5.2. Signals represent the weighted arithmetic mean of the horizontal and vertical velocity components considering weights of 1 and 2, respectively. Signals are jointly normalized. Letters P and S represent the analytically calculated time arrivals to each station of the P- and S- waves, respectively, travelling through bentonite. Superposed ovals indicate recognized wave sets. Yellow, purple, green and grey mark pcP, pcS, scS and scP waves, respectively. Orange indicates waves reflected in the ground and going back up and dark orange the interaction between P-waves coming down and P-waves coming up. Signals with bigger amplitude are marked by green ovals.

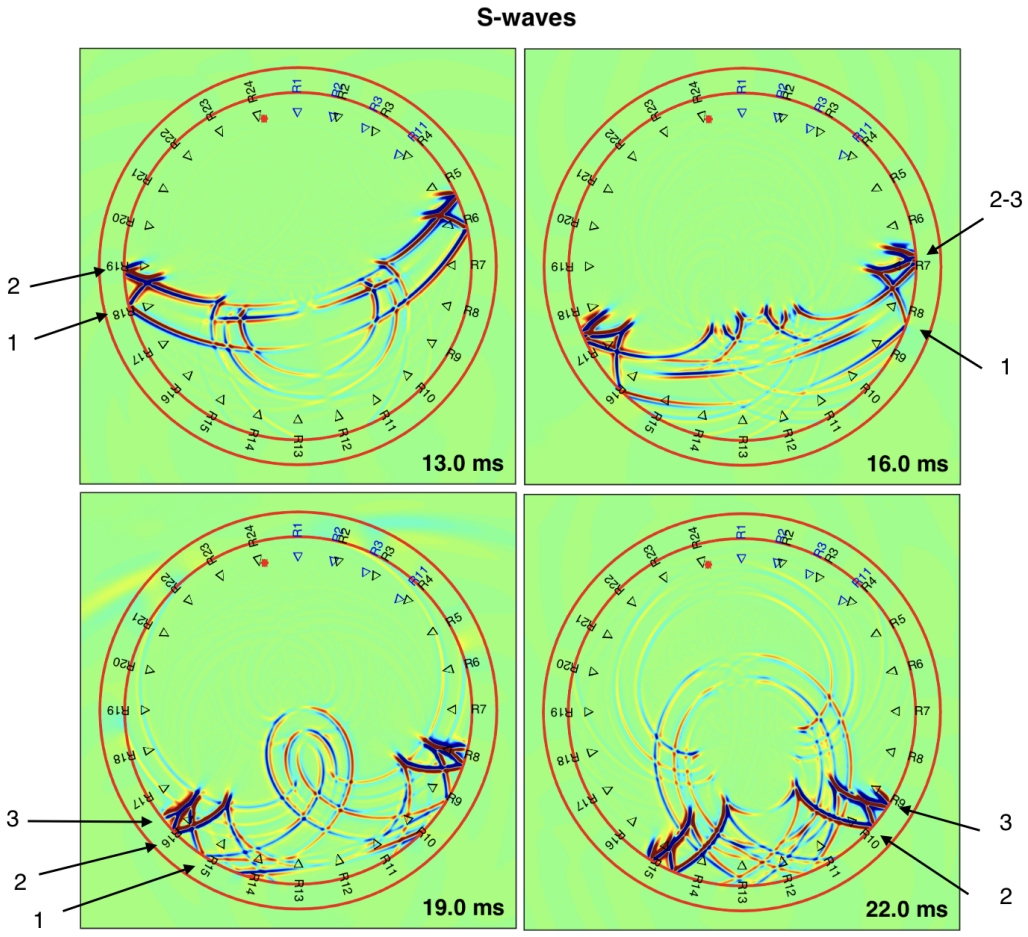

Figure 5.9: Snapshots for S-waves at 13, 16, 19 and 22 milliseconds of the elastic simulation in the tunnel model. Arrows point to new S-waves appearing in the simulation.

Viscoelastic simulation

Next, we add seismic attenuation to our simulation considering values for quality factors as indicated in Table 5.1. Comparing results with the obtained in the elastic case (Figure 5.10 and 5.11) we observe the strong influence of attenuation in the signals. Nonetheless, the most important signals can be still recognized in the seismograms.

Depth-depending simulation

In order to simulate changes in the seismic properties of bentonite due by changes in water saturation and compaction we do a viscoelastic simulation in the tunnel model with a constant gradient for P- and S-waves velocities for bentonite, considering a P-wave velocity of 250 m/s in the roof and 500 m/s in the bottom and a relationship of $v_s = 0.52v_p$, where v_p and v_s are P- and S-wave velocities, respectively. Figure 5.12 show seismograms for this simulations where we can appreciate that the signals are similar to the case of constant velocities but arriving faster and, especially for the stations farthest to the source more complex signals appear.

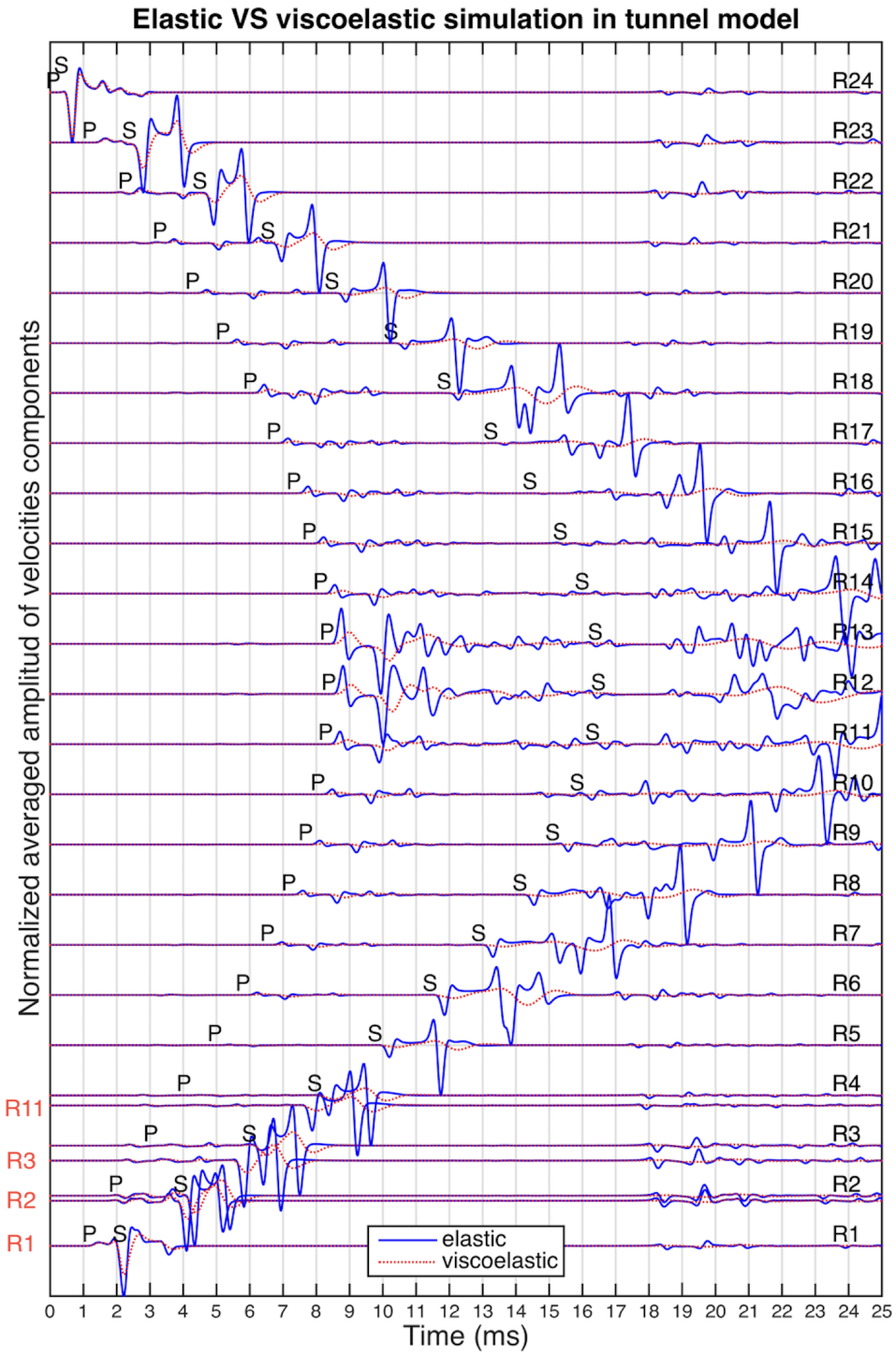

Figure 5.10: Velocity seismograms collected by FE- (red) and added- (black) recording stations corresponding to both, an elastic simulation (blue traces) and a viscoelastic simulation (red traces) in the tunnel model. Signals represent the weighted arithmetic mean of the horizontal and vertical velocity components considering weights of 1 and 2, respectively. Both signals for every station are normalized together. Letters P and S represent the analytically calculated time arrivals to each station of the P- and S- waves, respectively, travelling through bentonite.

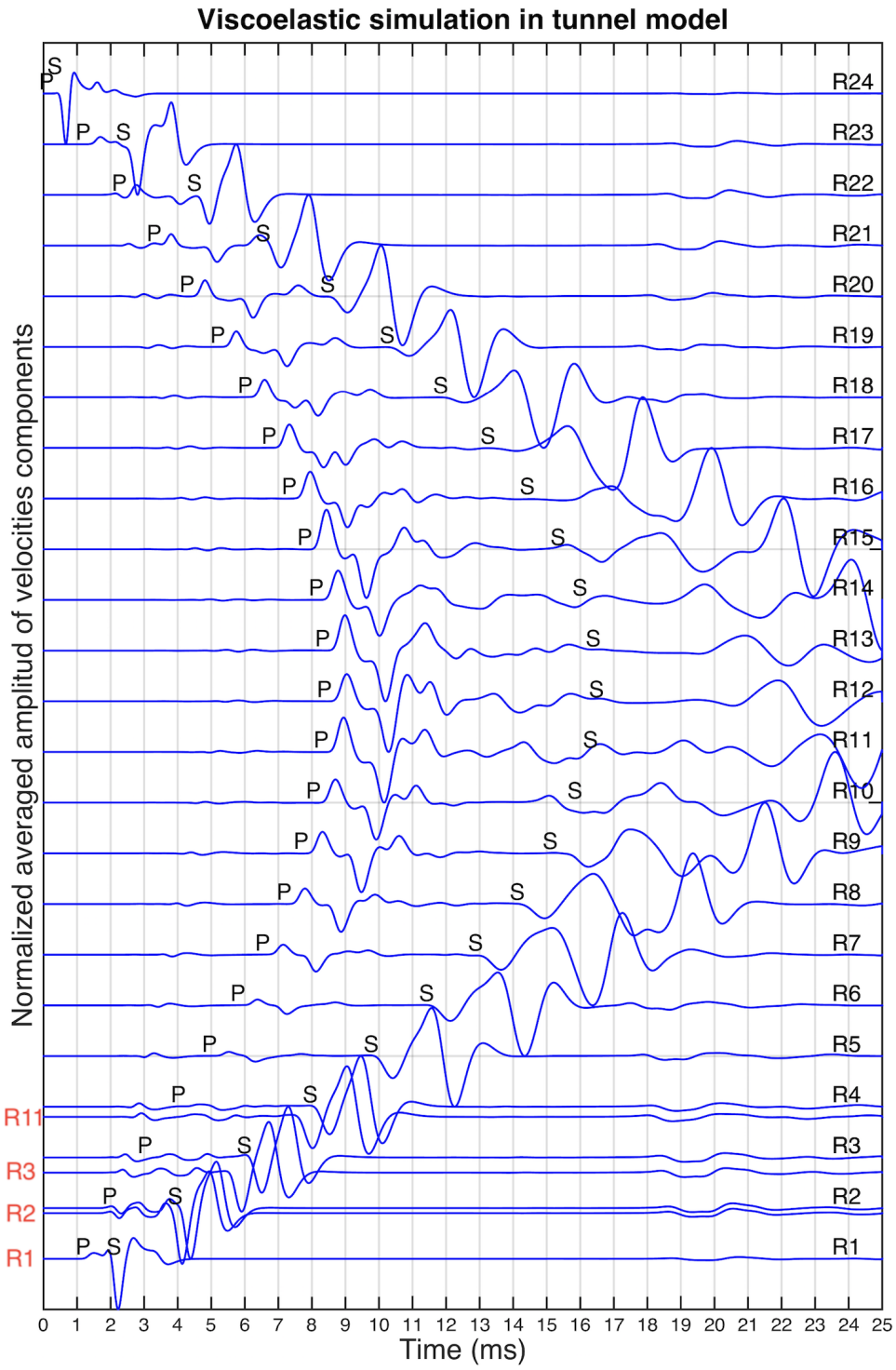

Figure 5.11: Velocity seismograms corresponding to the viscoelastic signals of Figure 5.10 but in this case seismograms are individually normalized.

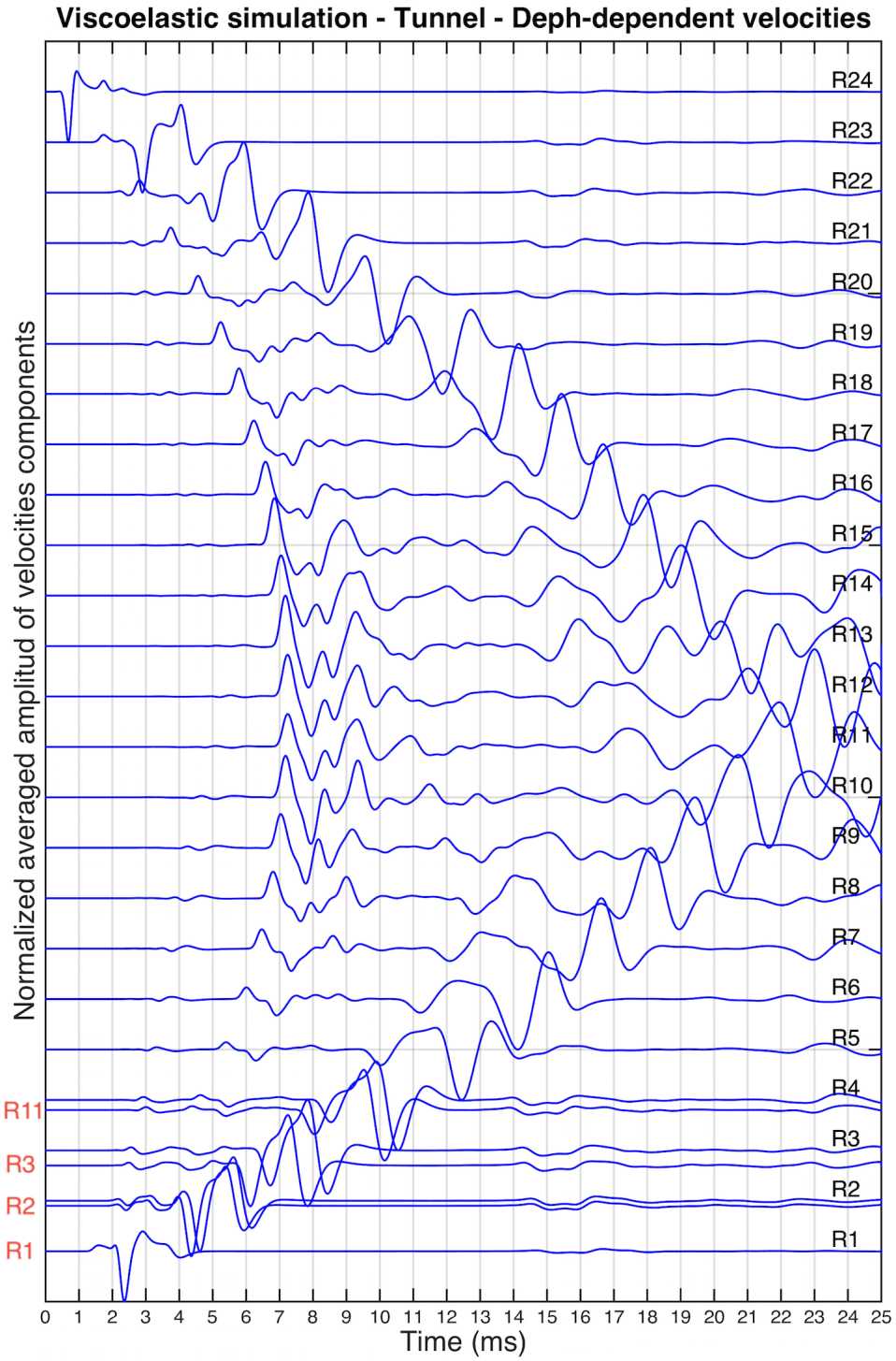

Figure 5.12: Velocity seismograms collected by FE- (red) and added- (black) recording stations corresponding to a viscoelastic simulation in the tunnel model with depth depending seismic velocities for bentonite. Signals represent the weighted arithmetic mean of the horizontal and vertical velocity components considering weights of 1 and 2, respectively. Signals are individually normalized.

5.4 Outcome

Through numerical simulations of wave propagation we analyzed the large variety of signals that is expected to be collected for each one of the receivers in the Full-Scale Emplacement Experiment at the Mont Terri underground rock laboratory. Due to the complexity of the real scenario which material properties are not completely known and change over time, it is not possible to make an exact comparison between the synthetic signals and the real ones. Nevertheless, the knowledge gained with this study was key for the understanding of the real waveforms.

Since most of the different waves have been identified, we can understand, for instance, from which transmitter-receiver pair the direct waves are more reliable to observe, as well as to more easily pick onsets of dominant wave packages visible over time helping with the estimation of the seismic velocities.

As an example, Figure 5.13 shows the synthetic signals for different sensor pairs suggesting that P-waves are better observed at short distances while S-waves are more observable at short and medium distances.

Based on the results of the numerical modelling the real data were analyzed and interpreted by Plenkers et al. (2019). A sample of the resulting outcome is presented here in Figure 5.14 showing plotted stacked waveforms from real signals and in Figure 5.15 representing the resulted estimated averaged velocities for P- and S-waves. For more details please look in Plenkers et al. (2019).

This analysis is crucial for estimation of seismic velocities of P- and S-waves in backfill of the full-scale emplacement experiment and results will be presented in future publications.

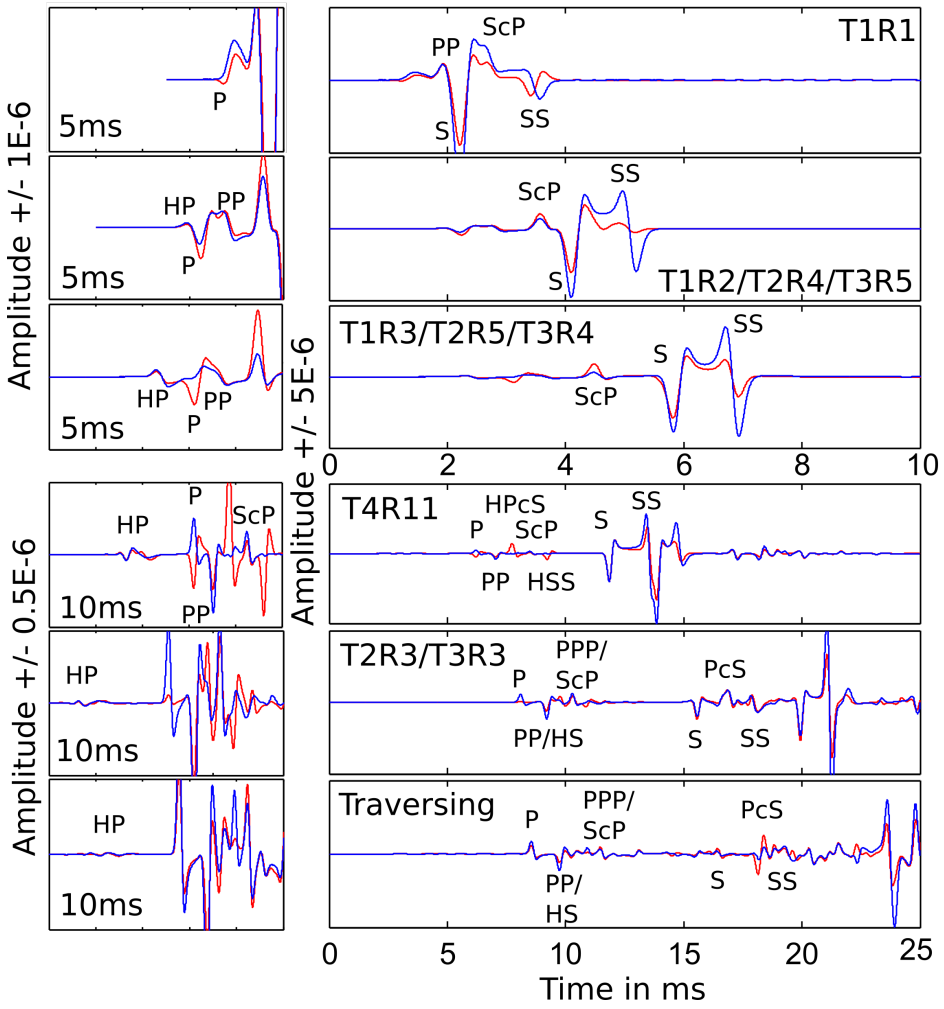

Figure 5.13: Figure from Plenkers et al. (2019). Waveforms for different transmitter-receivers pairs as extracted from the numerical simulation (elastic model). For comparison the seismogram for vertical (blue) and for orthogonal wave incidence (red) are shown. Direct wave (P, S), reflected waves (PP, SS, PPP), refracted (HP, HS) and converted waves (PcS, ScP) are visible. On the left a zoom into the onset is given. T1 to T4 are assumed to be located at the positions marked by S1, S2, S3 and GP1, respectively, in Figure 5.A2, and R1 to R5 at locations denoted by E1 to E5, respectively. We can see that P-waves are better observed at short distances (T1R1) while S-waves are more observable at short and medium distances (T1R1, T1R2, T2R4 and T3R5).

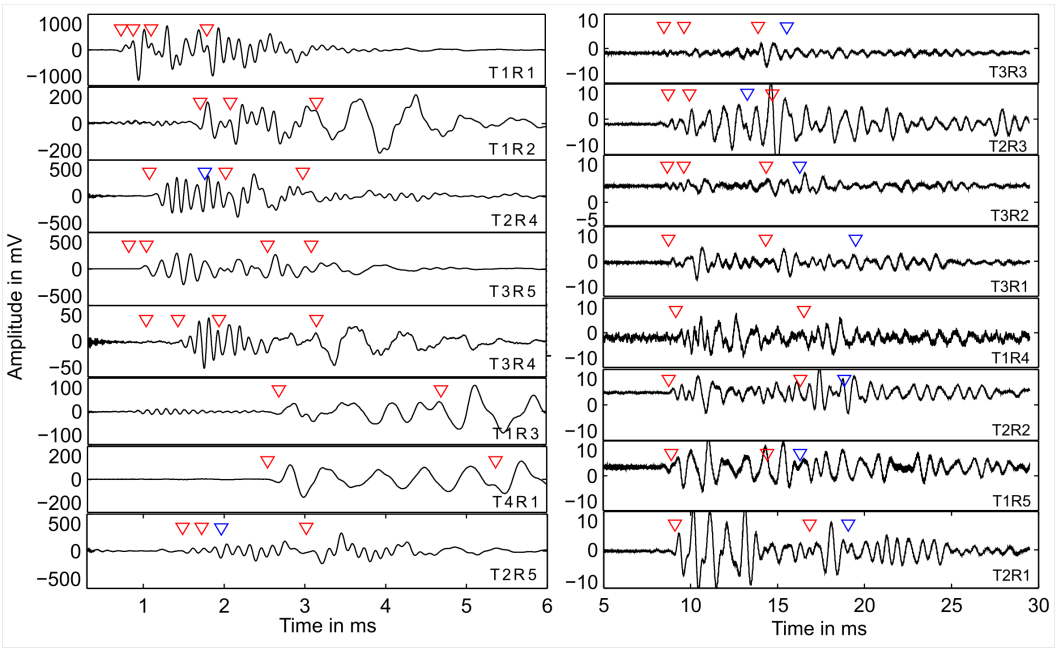

Figure 5.14: Figure from Plenkers et al. (2019). Stacked waveforms (1 week, End October 2018) with picks for short and intermediate tramsmitter-receiver distances (left) and long distances (right). Waveforms are sorted from top to bottom according to the travel distance. Manual picks are marked by triangles (red: used in interpretation, blue: discarded). Picks were chosen where dominant wave packages are visible over time. Note that during picking wave packages are chosen that are visible over some extended time period i.e. in an individual weekly stack the wave package might be less pronounced.

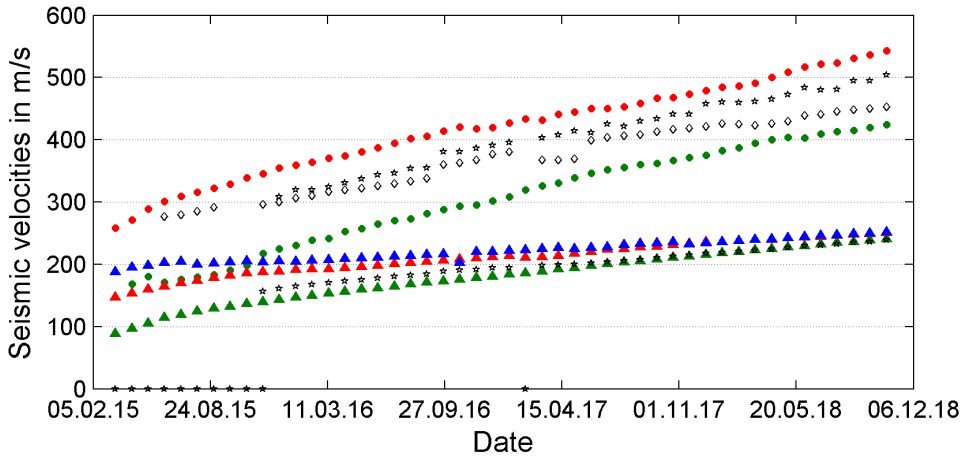

Figure 5.15: Figure from Plenkers et al. (2019). Final Result: Averaged velocities for P wave and S wave. Averaged data estimated near the tunnel roof (green), near the tunnel bottom (red) and from signals traversing the tunnel (blue) is shown. P wave velocities are shown with filled circles; S wave velocities are shown with filled triangles. For comparison the velocities estimated for data of the temporary array is added (T4R1: starts; T4R11: diamonds).

5.5 Conclusions

High radioactive waste repositories must ensure the long-term shielding of the residuals and allow the monitoring of its state in an accurate way. As such monitoring has to be non-invasive, seismic monitoring techniques are being applied. This work, by means the numerical modelling, shows the great influence that the tunnel shape, the seismic properties of materials involved and the location of receivers have on the recorded signals, highlighting that such seismic monitoring is not possible without the detailed knowledge of the above elements and its changes over time. For this reason, more research should be done in this field and more accurate seismic models should be obtained, especially for bentonite.

5.6 Acknowledgements

This project has received funding from the European Union's Horizon 2020 research and innovation programme under the Marie Sklodowska-Curie grant agreement No 642029 - ITN CREEP.

We are grateful to Tom Spillmann (Nagra) and people from GMuG for the opportunity to collaborate in the FE-experiment and Hansruedi Maurer for his comments about the seismic properties of the materials.

The authors gratefully acknowledge the developers of the software SOFI2D and the computing time granted on the supercomputer Mogon at Johannes Gutenberg University Mainz (hpc.uni-mainz.de).

5.7 Appendix

5.7.1 Choice of the numerical setup

In order to get the position of sources and receivers with respect to the cross-section of the tunnel under investigation (GM 17.5) we use coordinates from Tables A.1 and A.2 (figure 5.A1) in the Technical report 2015-27 (Spillmann & Philipp (2015)).

Figure 5.A2 shows the vertical projection (coordinates x and y) of such coordinates and, in red line, the position of GM 17.5. By considering the vertical plane defined by the red line and the depth of each element from the aforementioned Tables A.1 and A.2 we get the 2D numerical model for our simulation (figure 5.A4). The new relatives coordinates and the distances source-receivers can be see in Table 5.A1. As suggests figure 3 in Spillmann & Philipp (2015) (figure 5.A3) we considered a diameter of 2.8 meters for bentonite and 0.20 meters of concrete (3.2 meters total diameter of the tunnel). As stations are pointing towards the centre of the tunnel a rotation of the coordinate axis for each receiver is needed (figure 5.A5).

Tab. A-1: Coordinates of the geophysical pipe (centre).

	GP1 (left)			
GM	**Y** [m]	**X** [m]	**Z** [m]	**Pipe length XYZ** [m]
5.65	2579279.55	1247614.59	516.64	17.70
5.71	2579279.50	1247614.56	516.64	17.63
9.81	2579275.91	1247612.57	516.73	13.54
14.80	2579271.53	1247610.18	516.81	8.54
16.01	2579270.49	1247609.55	516.79	7.33
17.94	2579268.79	1247608.65	516.80	5.40
19.85	2579267.10	1247607.74	516.80	3.49
21.78	2579265.41	1247606.81	516.80	1.56
23.34	2579264.04	1247606.07	516.80	0.00
	GP2 (right)			
5.61	2579278.99	1247615.74	516.61	17.70
5.76	2579278.85	1247615.67	516.61	17.55
9.74	2579275.33	1247613.80	516.72	13.56
14.80	2579270.82	1247611.53	516.82	8.51
15.73	2579269.98	1247611.12	516.82	7.58
17.67	2579268.26	1247610.22	516.82	5.64
19.66	2579266.50	1247609.30	516.83	3.65
21.55	2579264.82	1247608.43	516.82	1.76
22.78	2579263.74	1247607.86	516.81	0.53
23.31	2579263.27	1247607.60	516.79	0.00

Tab. A.2: Coordinates of fix installed sensors.

Array	**Sensor**	**Easting** [m]	**Northing** [m]	**Elevation** [m]
Roof	S1	2579268.910	1247609.353	517.129
Floor	S2	2579269.201	1247610.095	514.734
Floor	S3	2579268.641	1247609.793	514.724
Roof	E1	2579268.762	1247609.583	517.169
Roof	E2	2579268.652	1247609.844	517.130
Roof	E3	2579268.518	1247610.056	517.035
Floor	E4	2579269.387	1247609.584	514.691
Floor	E5	2579268.777	1247609.255	514.660

Figure 5.A1: Coordinates of source and receivers (from Technical note 2015-27).

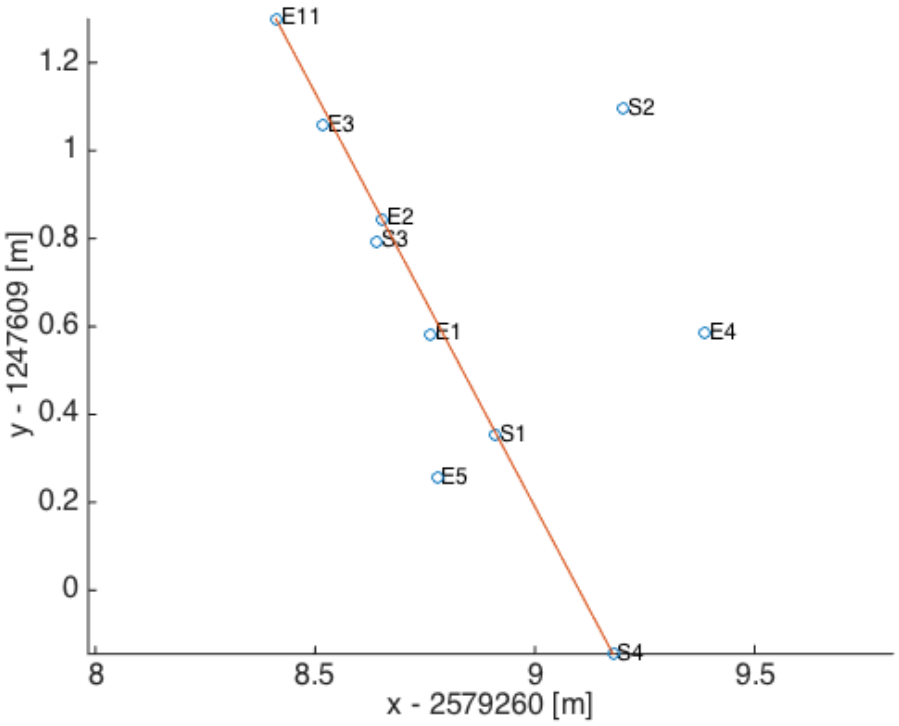

Figure 5.A2: Vertical projection of sources (S1, S2, S3 and S4) and receivers (E1, E2, E3, E4, E5 and E11). Coordinates uses are from Table A.1 and A.2 (figure 5.A1) in the Technical report 2015-27 (Spillmann & Philipp (2015)). Red line shows the position of the cross-section GM 17.5.

Table 5.A1: Coordinates of FE elements with respect to the centre of the tunnel, angle with respect to azimuth and distances from source S1 to receivers. There is a small discrepancy between distances deduced and distances listed in Spillmann & Philipp (2015).

	x $[m]$	depth $[m]$	angle $[^o]$	distance to S1 $[m]$	distance to S1 in Spillmann & Philipp (2015)
S1	−0.273	−1.190	167		
E1	0.000	−1.230	180	0.2758	0.28
E2	0.282	−1.191	193	0.5546	0.52
E3	0.532	−1.096	206	0.8103	0.81
E11	0.797	−0.881	222	1.1133	-

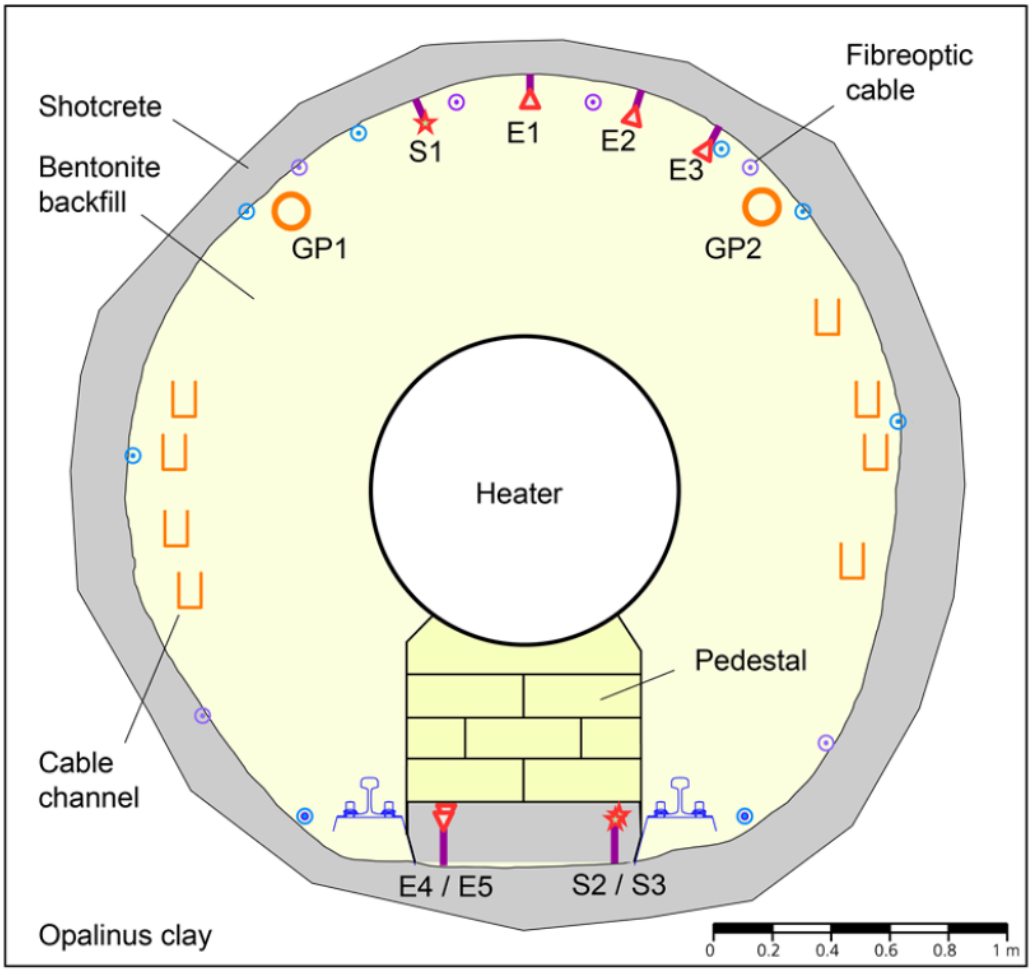

Figure 5.A3: Figure 3 from Spillmann & Philipp (2015). "FE tunnel cross-section at GM 17.5 m, view to tunnel end. Note heater location is behind profile"

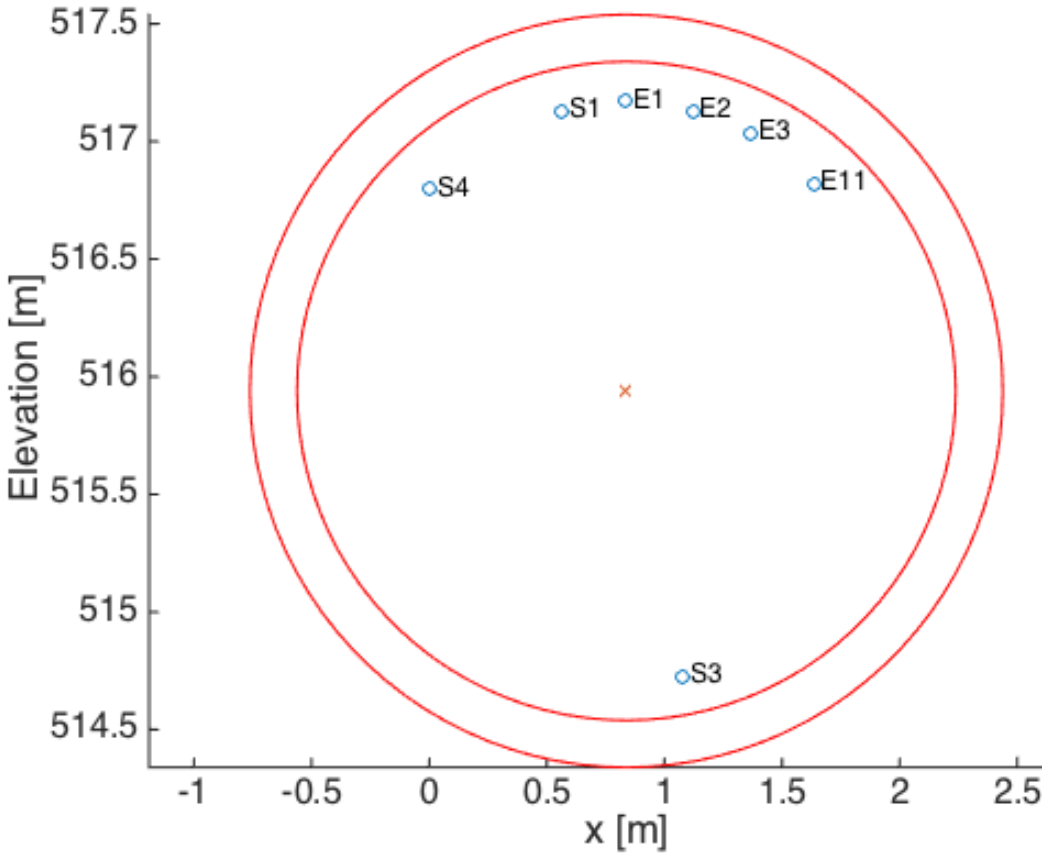

Figure 5.A4: Localization of FE elements for a 2D numerical model of the tunnel cross-section GM 17.5.

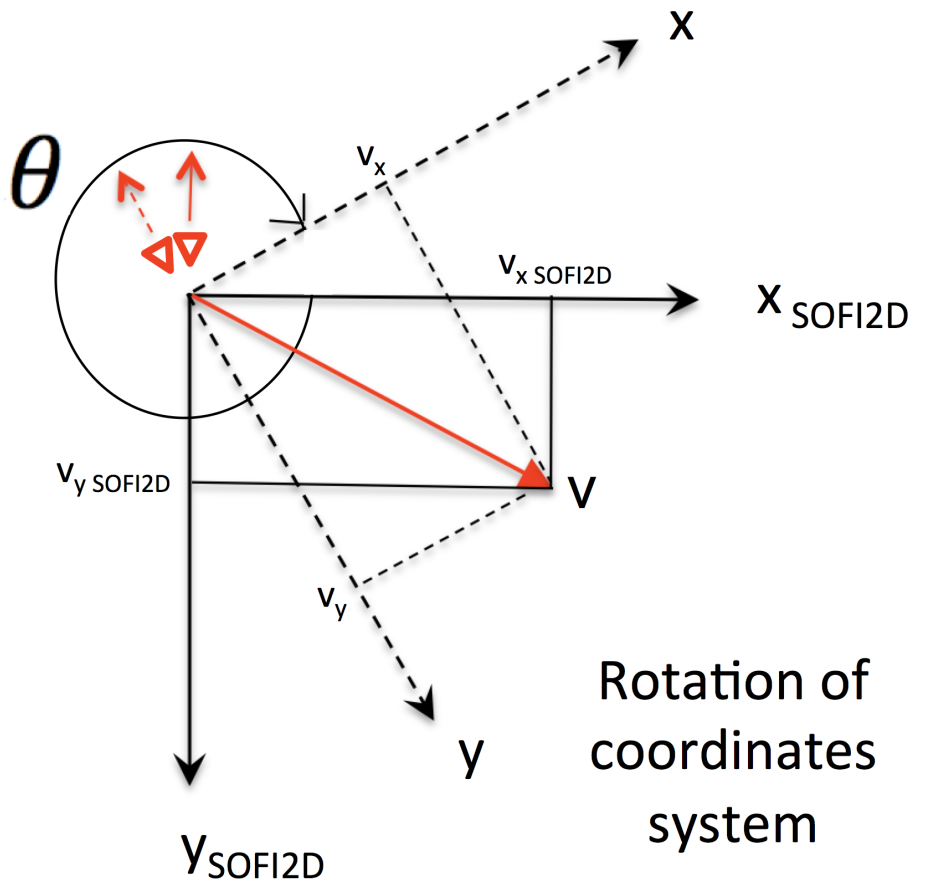

$$\begin{pmatrix} v_x \\ v_y \end{pmatrix} = \begin{pmatrix} cos\theta & sin\theta \\ -sin\theta & cos\theta \end{pmatrix} \begin{pmatrix} v_{x\ SOFI2D} \\ v_{y\ SOFI2D} \end{pmatrix}$$

Figure 5.A5: Rotation of coordinate axis.

5.7.2 Properties for shotcrete

As described in Tables 1 and 3 from the Technical report 2012-97 (Wetzig & Reinhold (2014)), we consider for shotcrete a density of 2209 Kg/m^3 and a modulus of elasticity of 10.8 GPa. These properties correspond to a gallery specimen in phase 1. To calculate seismic velocities from these data we use a Poisson ratio of 0.25 and apply the relations:

$$v_p = \sqrt{\frac{(1-\nu)E}{(1+\nu)(1-2\nu)\delta}} \tag{5.4}$$

$$v_s = \frac{v_p}{\sqrt{3}} \tag{5.5}$$

which give us a P-wave velocity (v_p) of 2422 m/s and a S-wave velocity of (v_s) of 1398 m/s.

5.7.3 Snapshots corresponding to the elastic simulation in tunnel model

Figures 5.A6 to 5.A14 show P- and S-waves for the first 24 milliseconds of the elastic simulation in tunnel model.

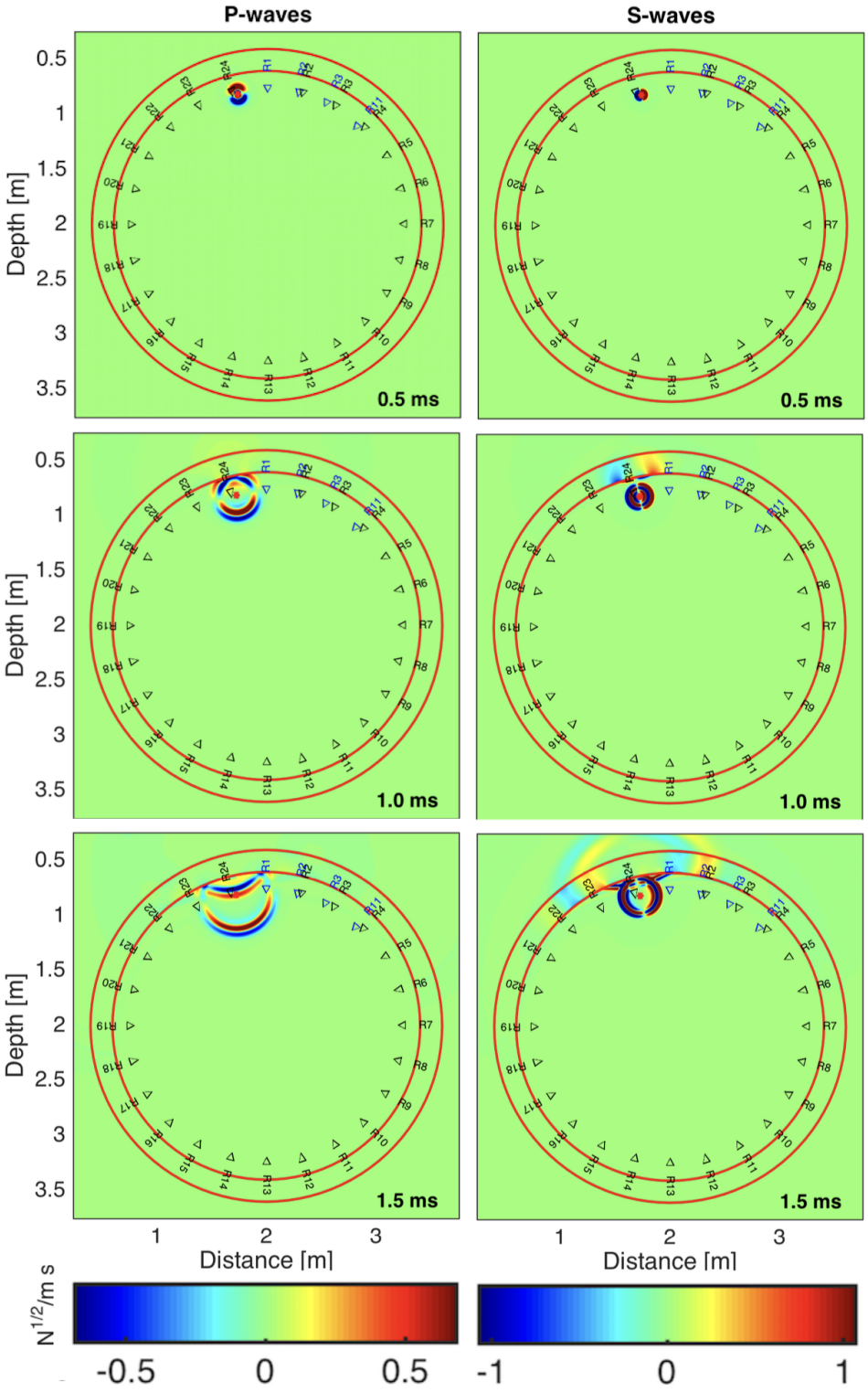

Figure 5.A6: Snapshots corresponding to 0.5, 1.0 and 1.5 milliseconds of the elastic simulation in the tunnel model.

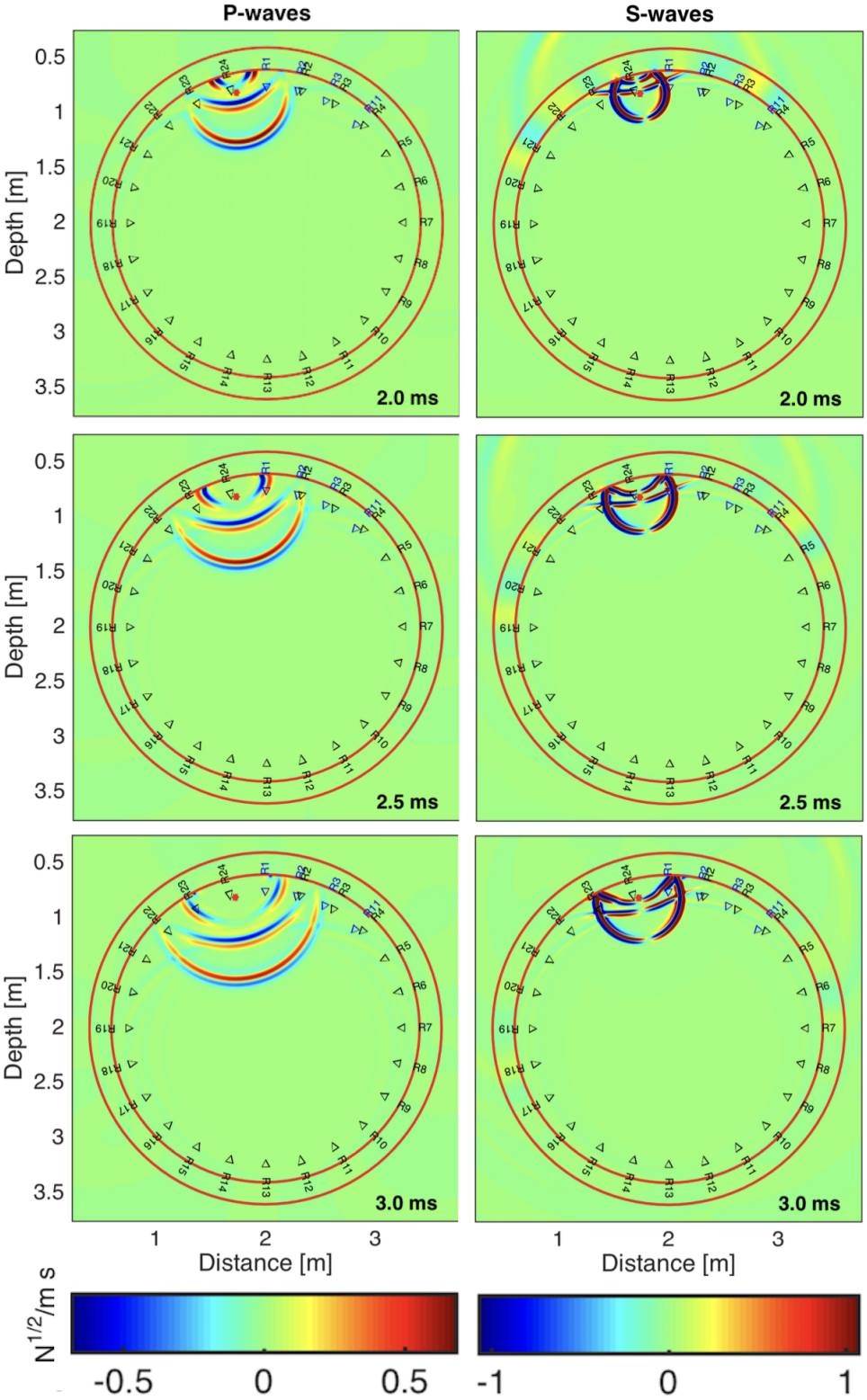

Figure 5.A7: Snapshots corresponding to 2.0, 2.5 and 3.0 milliseconds of the elastic simulation in the tunnel model.

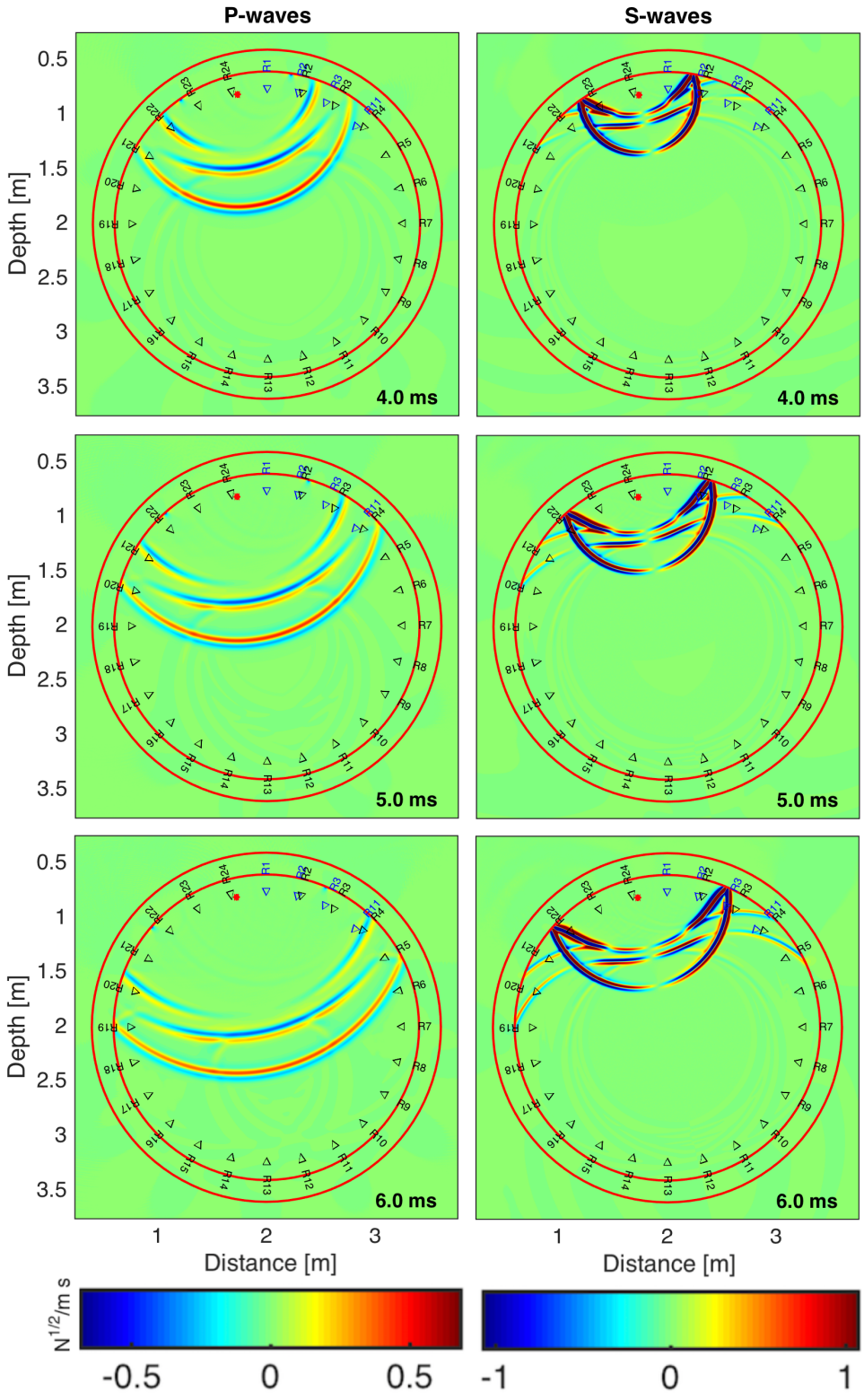

Figure 5.A8: Snapshots corresponding to 4.0, 5.0 and 6.0 milliseconds of the elastic simulation in the tunnel model.

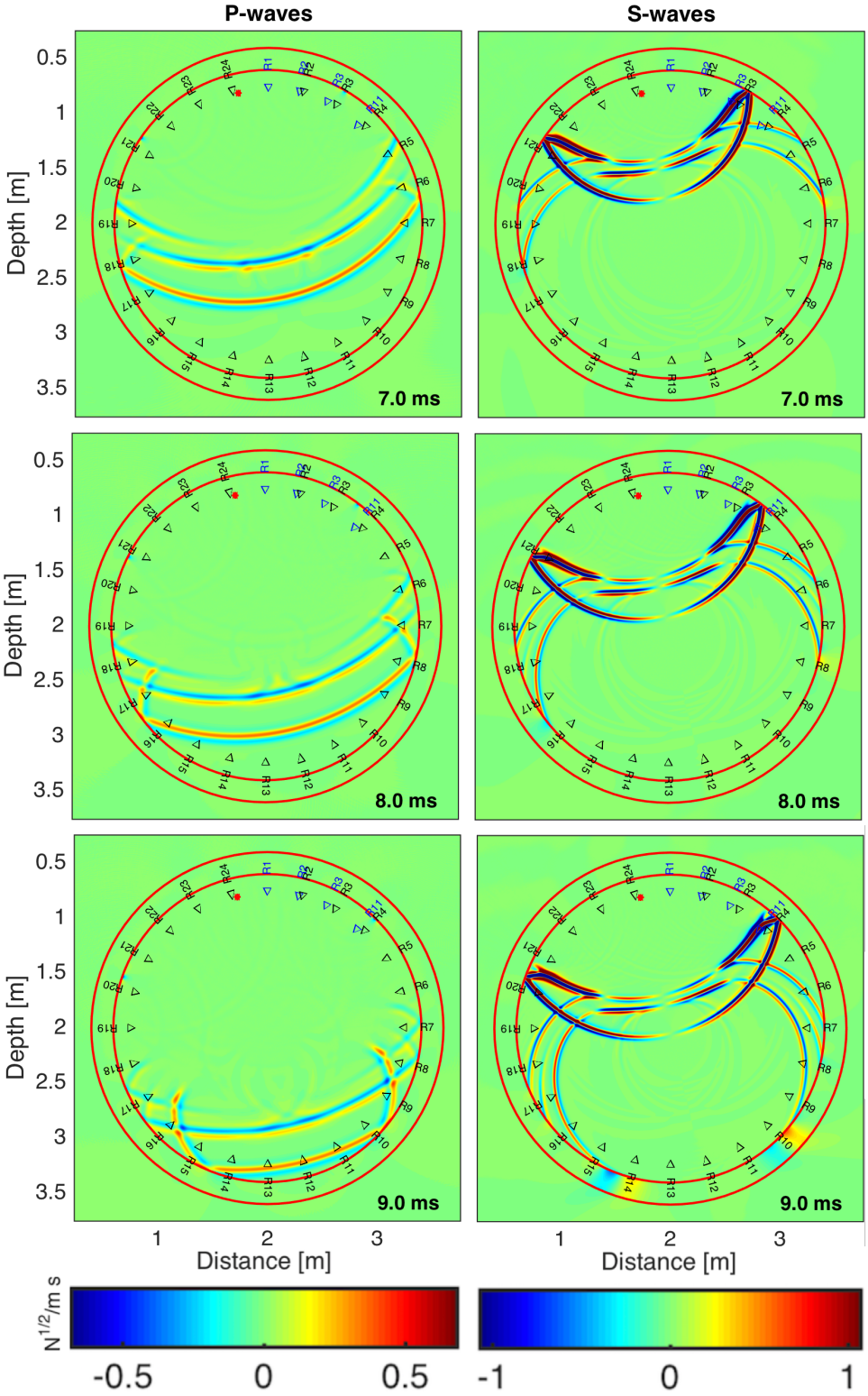

Figure 5.A9: Snapshots corresponding to 7.0, 8.0 and 9.0 milliseconds of the elastic simulation in the tunnel model.

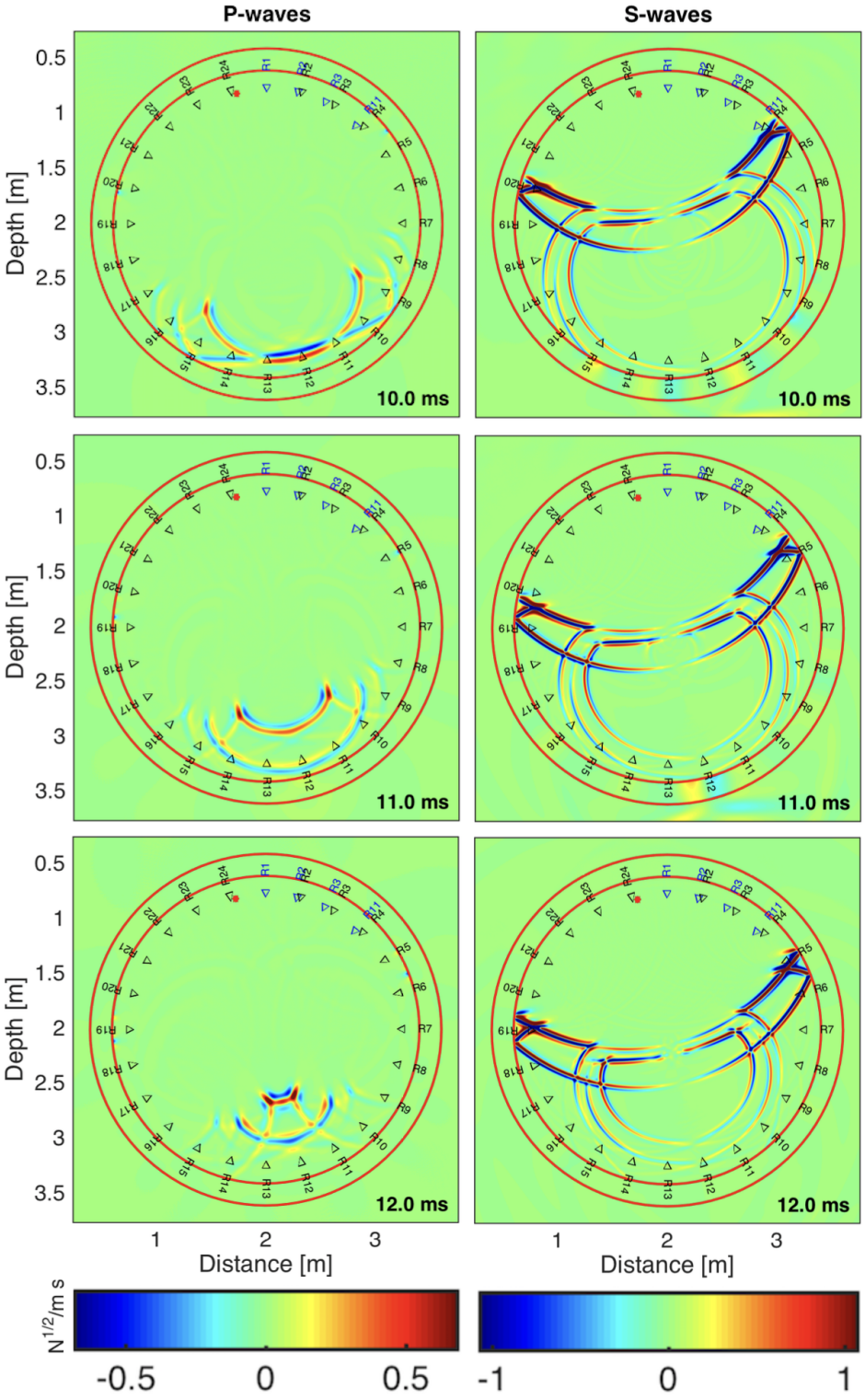

Figure 5.A10: Snapshots corresponding to 10.0, 11.0 and 12.0 milliseconds of the elastic simulation in the tunnel model.

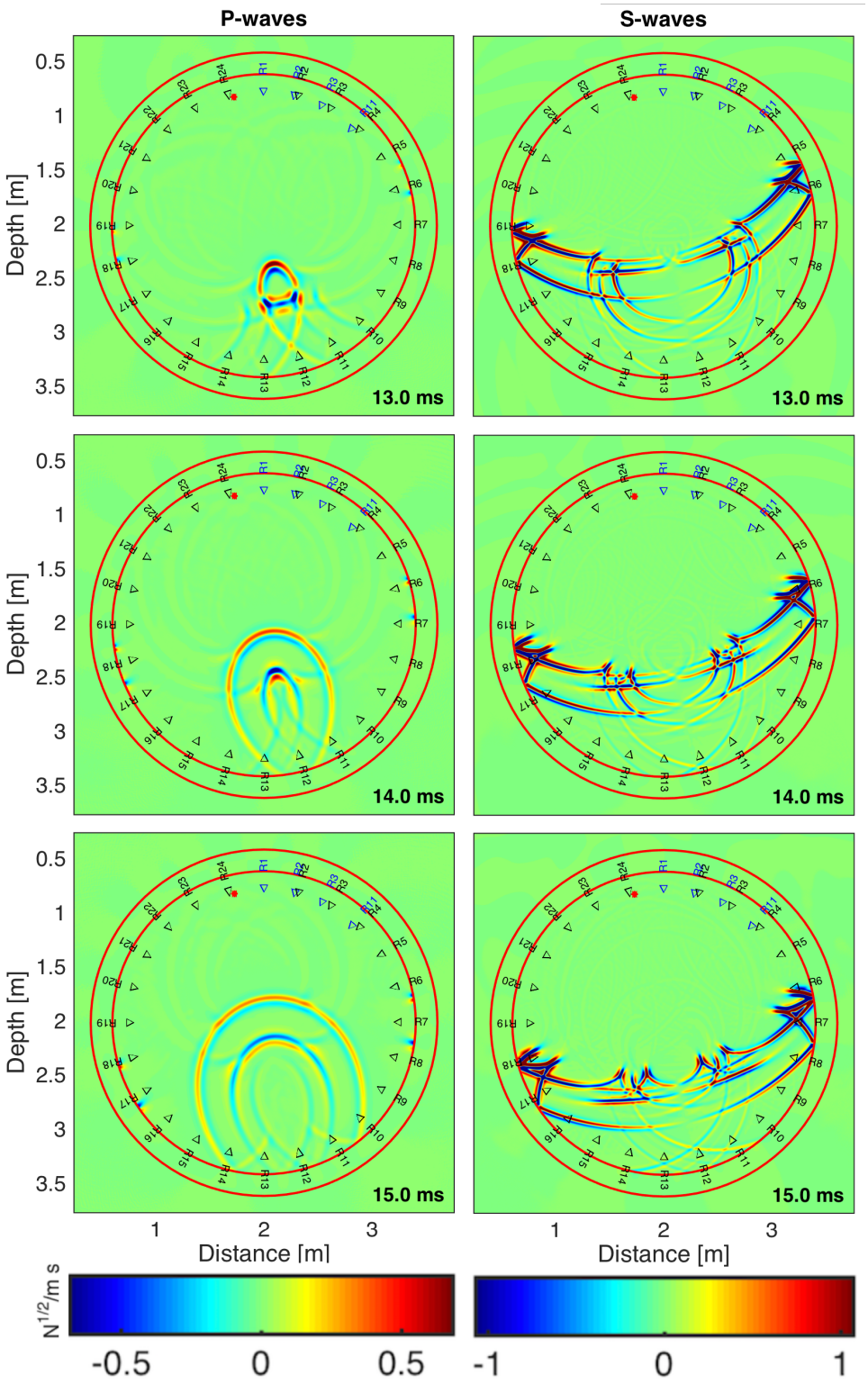

Figure 5.A11: Snapshots corresponding to 13.0, 14.0 and 15.0 milliseconds of the elastic simulation in the tunnel model.

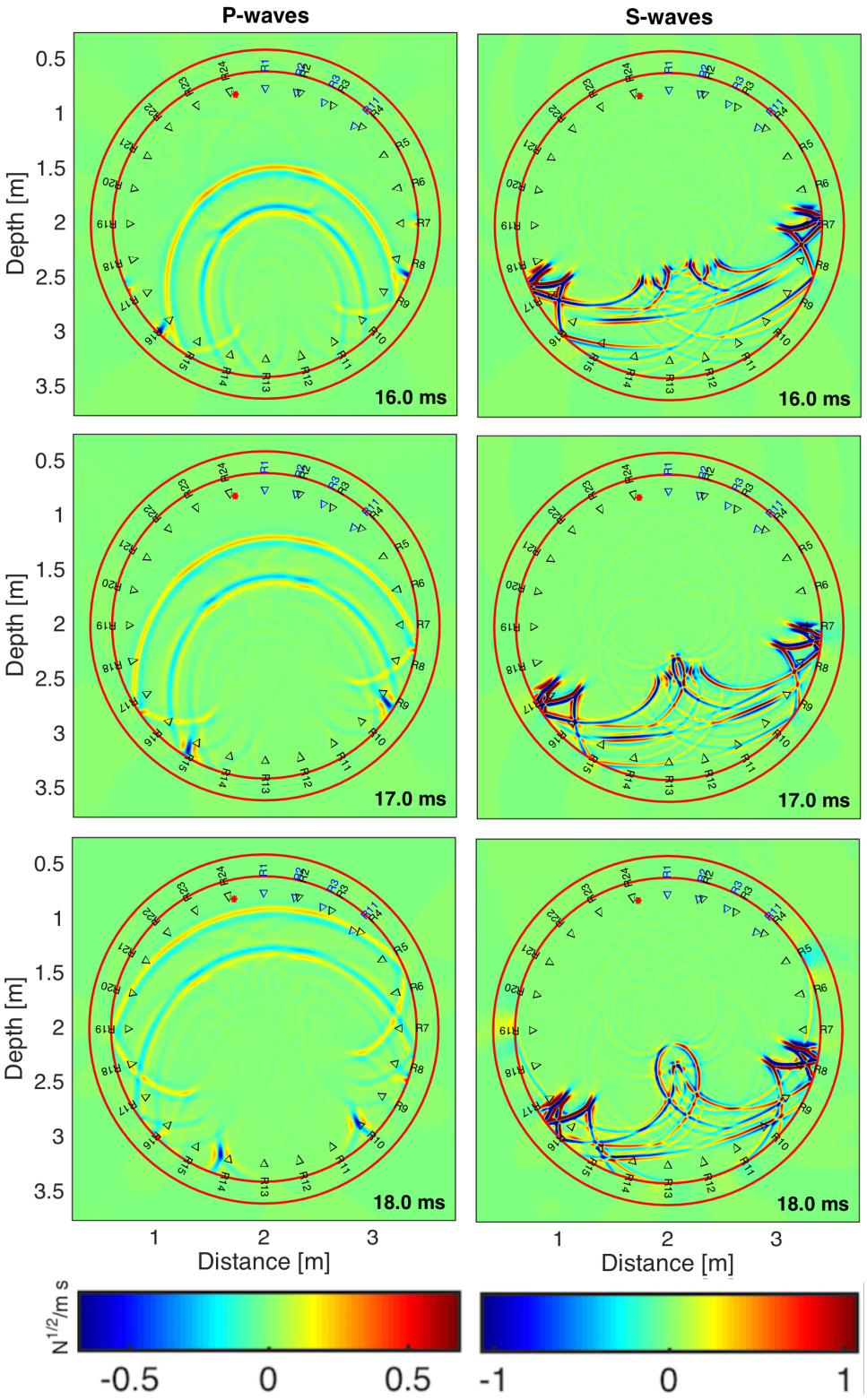

Figure 5.A12: Snapshots corresponding to 16.0, 17.0 and 18.0 milliseconds of the elastic simulation in the tunnel model.

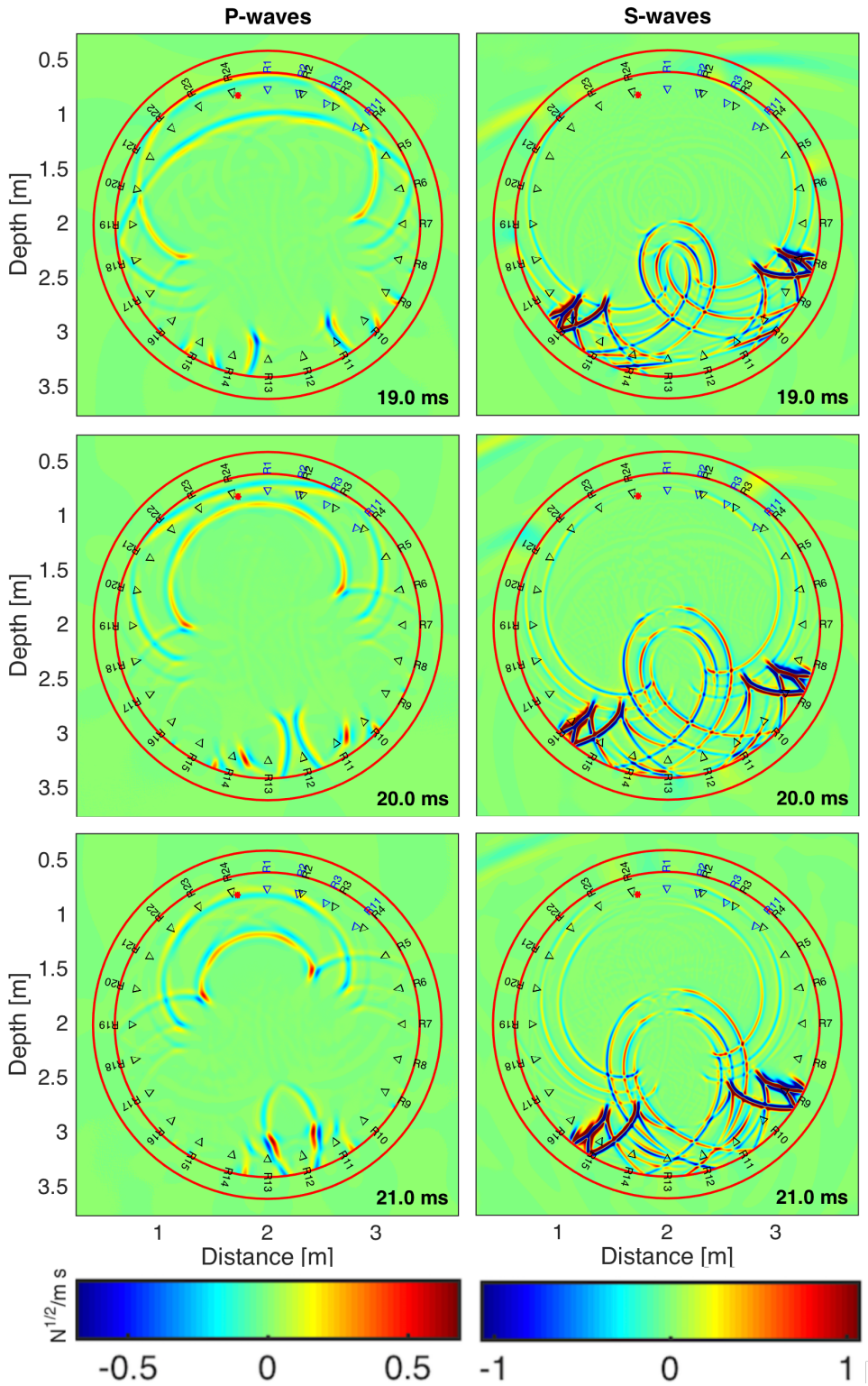

Figure 5.A13: Snapshots corresponding to 19.0, 20.0 and 21.0 milliseconds of the elastic simulation in the tunnel model.

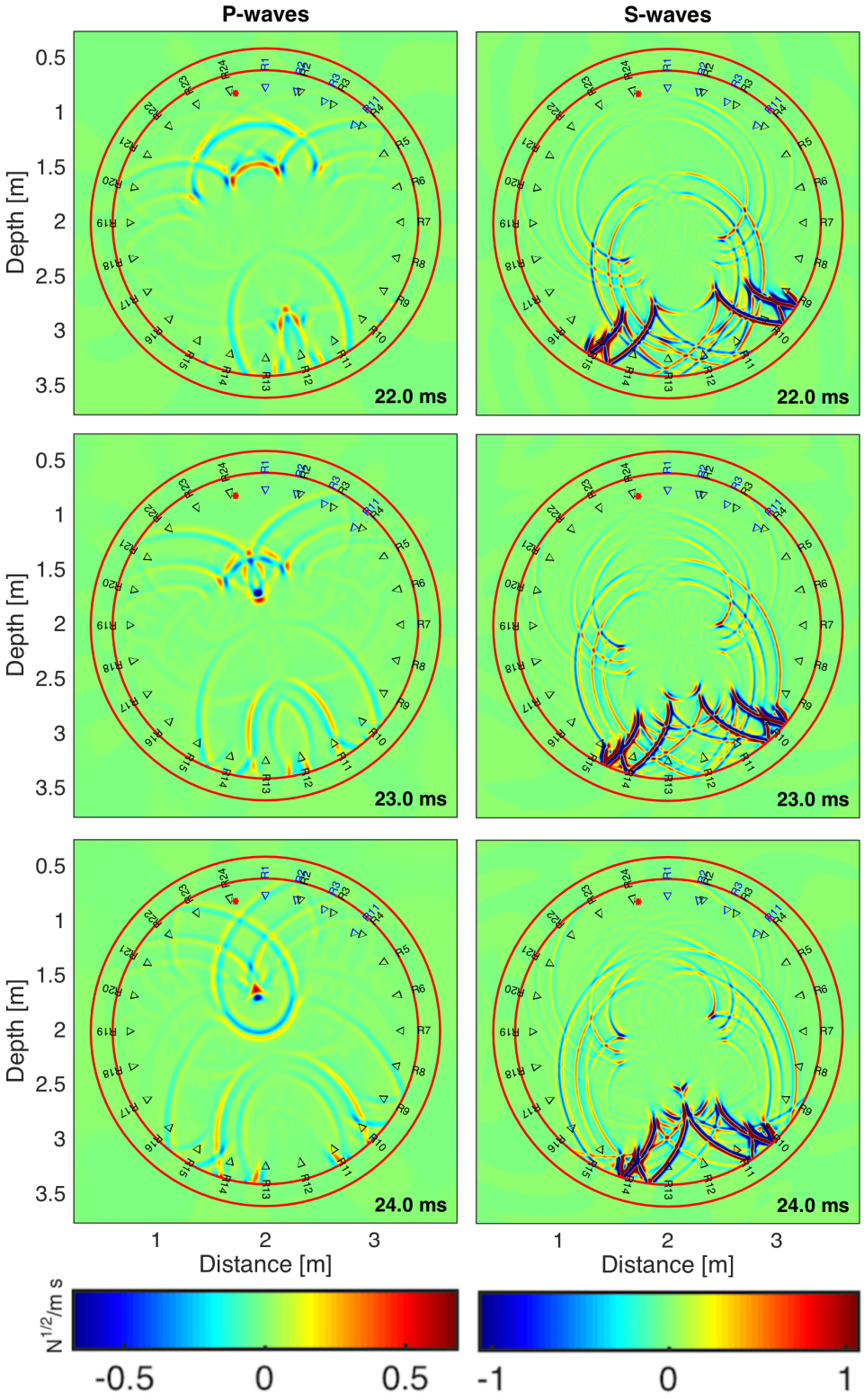

Figure 5.A14: Snapshots corresponding to 22.0, 23.0 and 24.0 milliseconds of the elastic simulation in the tunnel model.

Chapter 6

Remarks and outlook

> The soul seeks solace but man
> must seek heaven...
>
> Claudio González Grueso,
> *The Connection*

We built a new 3D parallel software tool to simulate fluid injection and crack propagation in poro-visco-elasto-plastic rheologies. We made this by coupling the physics describing lithospheric deformation in visco-elasto-plastic rheologies and those expressing the pressure of liquids in porous rocks.

We used the resulting code for modelling the formation of localized shear and tensile zones and to reproduce 2D failure patterns generated by a localized pore-pressure increase. Our results are in accordance with those presented by other authors through theoretical, numerical and/or experimental investigations. Furthermore, we simulated the injection of fluid in 3D setups under different initial stress conditions to investigate how the reservoir stress state influences on the propagation of failure zones. As a result of this study, we gave a generalization of possible 3D failure patterns caused by pore-pressure increase concluding that, if stress conditions are low, failure zones develop in spheroidal shape propagating predominantly in the direction of the max-

imum and intermediate principal stresses and, if stress conditions are high, failures bifurcate in the plane defined by the minimum and the maximum principal stresses producing buttery-like shape oriented in the direction of the intermediate principal stress. We performed the numerical simulation of a hydraulic fracture project showing the significant influence of permeability values on the development of fractures.

The new numerical tool includes the dominant physics of the hydrofracturing processes being able, in particular, to localize the areas where failure occurs, either in tensile or shear mode. However, for describing the proper iteration between the porous flow and the host rocks, physical models must be improved by means a better understanding of how material properties change during deformation and failure stages, specially quantifying how hydraulic properties as permeability and porosity are enhanced when increasing stress. In addition, for post-failure stages, fracture sealing and compaction processes must be implemented to control the evolution of fractures and the reservoir stress conditions over time.

Furthermore, given that induced seismicity is often associated with injection projects, this tool can be highly useful as well to investigate the relationship between the generation of fractures and the generation of seismic signals in real reservoirs, helping to constrain the relation between failure areas and seimicity location and magnitude. Further, since we already implemented in the past an explicit solver to simulate seismic wave propagation[1], the integration of this code in the new tool would be a perfect complement for this issue.

In the field of volcanology, the methodology has the potential to understand magma propagation and interpret focal mechanisms during volcanic eruptions. Nevertheless, the inclusion of the fluid temperature in the physical model would provide a more realistic result.

On the other hand, we used a software code to simulate the non-invasive

[1]Package is available at https://bitbucket.org/bkaus/lamem branch “explicit”

seismic monitoring system of a high radioactive waste repository showing the significant impact of the tunnel shape and the seismic properties of materials on the recorded signals. In spite of the ignorance of the exact seismic properties of the materials and their changes over time, we obtained a key help for the understanding of the expected waveforms behaviour and for the estimation of seismic velocities. Nevertheless, for an exact comparison between the synthetic signals and the real ones more research should be done in the investigation of seismic models and properties for materials involved in these processes.

In general, the heterogeneity of the subsurface and the lack of knowledge of material properties and how they change over time due to the action of temperature, liquid pressure, compaction, etc., make realistic modelling difficult. Nevertheless, numerical modelling is a key tool to investigate physical processes, with the advantage of allowing a wide range of physical hypotheses and parameters to be considered, complementing other studies such as laboratory experiments, in situ seismic monitoring, real borehole data or inversion techniques used to obtain the distribution of fractures within a site, feeding back one each other to upgrade current models and tools.

Therefore, more work needs to be done in these fields to improve the planning and monitoring of current issues as hydrofracturing or nuclear waste management projects.

Bibliography

Abeyartne, R. (2012), 'Continuum Mechanics Volume II of Lecture Notes on The Mechanics of Elastic Solids Cambridge, http', *web. mit. edu/abeyartne/lecture_notes. html* **11**.

Apted, M. J. & Ahn, J. (2017), *Geological repository systems for safe disposal of spent nuclear fuels and radioactive waste*, Woodhead Publishing.

Arthur, J., Dunstan, T., Al-Ani, Q. & Assadi, A. (1977), 'Plastic deformation and failure in granular media', *Geotechnique* **27**(1), 53–74.

Balay, S., Abhyankar, S., Adams, M. F., Brown, J., Brune, P., Buschelman, K., Dalcin, L., Dener, A., Eijkhout, V., Gropp, W. D., Kaushik, D., Knepley, M. G., May, D. A., McInnes, L. C., Mills, R. T., Munson, T., Rupp, K., Sanan, P., Smith, B. F., Zampini, S., Zhang, H. & Zhang, H. (2018), PETSc Users Manual, Technical Report ANL-95/11 - Revision 3.10, Argonne National Laboratory. http://www.mcs.anl.gov/petsc.

Biot, M. & Willis, D. (1957), 'The elastic coeff cients of the theory of consolidation', *J. appl. Mech* **24**, 594–601.

Biryukov, A., Tisato, N. & Grasselli, G. (2016), 'Attenuation of elastic waves in bentonite and monitoring of radioactive waste repositories', *Geophysical Journal International* **205**, 105–121.

Bohlen, T. (2002), 'Paralel 3-D viscoelastic finite difference seismic modelling', **28**, 887–899.

Bohlen, T., De Nil, D., Daniel, K. & Jetschny, S. (2015), 'SOFI2D, seismic modeling with finite differences 2D-elastic and viscoelastic version, User's Guide', *Karlsruhe Institute of Technology, Karlsruhe* .

Bossart, P. (2017), 'Characteristics of the Opalinus Clay at Mont Terri'.

Buiter, S. J. (2012), 'A review of brittle compressional wedge models', *Tectonophysics* **530**, 1–17.

Cesca, S., Grigoli, F., Heimann, S., González, A., Buforn, E., Maghsoudi, S., Blanch, E. & Dahm, T. (2014), 'The 2013 September–October seismic sequence offshore Spain: a case of seismicity triggered by gas injection?', *Geophysical Journal International* **198**(2), 941–953.

Choi, E. & Petersen, K. D. (2015), 'Making Coulomb angle-oriented shear bands in numerical tectonic models', *Tectonophysics* **657**, 94–101.

Clark, J. et al. (1949), 'A hydraulic process for increasing the productivity of wells', *Journal of Petroleum Technology* **1**(01), 1–8.

Collignon, M., Yamato, P., Castelltort, S. & Kaus, B. J. (2016), 'Modeling of wind gap formation and development of sedimentary basins during fold growth: application to the Zagros Fold Belt, Iran', *Earth Surface Processes and Landforms* **41**(11), 1521–1535.

Coulomb, C. (1773), 'Test on the applications of the rules of maxima and minima to some problems of statics related to architecture', *Mem. Math. Phys* **7**, 343–382.

David, C., Wong, T.-F., Zhu, W. & Zhang, J. (1994), 'Laboratory measurement of compaction-induced permeability change in porous rocks: Implications for the generation and maintenance of pore pressure excess in the crust', *Pure and Applied Geophysics* **143**(1-3), 425–456.

Duretz, T., May, D. A., Gerya, T. & Tackley, P. (2011), 'Discretization errors and free surface stabilization in the finite difference and marker-in-cell method for applied geodynamics: A numerical study', *Geochemistry, Geophysics, Geosystems* **12**(7).

E Manukyan, H Maurer, S. M. S. G. A. G. (2012), 'Seismic monitoring of radioactive waste repositories'.

Galvan, B. & Miller, S. (2013), A full GPU simulation of evolving fracture networks in a heterogeneous poro-elasto-plastic medium with effective-stress-dependent permeability, *in* 'GPU Solutions to Multi-scale Problems in Science and Engineering', Springer, pp. 305–319.

Gens, A., Guimaraes, L. d. N., Garcia-Molina, A. & Alonso, E. (2002), 'Factors controlling rock–clay buffer interaction in a radioactive waste repository', *Engineering Geology* **64**(2-3), 297–308.

Gerya, T. (2009), *Introduction to numerical geodynamic modelling*, Cambridge University Press.

Gerya, T. V. & Yuen, D. A. (2007), 'Robust characteristics method for modelling multiphase visco-elasto-plastic thermo-mechanical problems', *Physics of the Earth and Planetary Interiors* **163**(1-4), 83–105.

Häring, M. O., Schanz, U., Ladner, F. & Dyer, B. C. (2008), 'Characterisation of the Basel 1 enhanced geothermal system', *Geothermics* **37**(5), 469–495.

Harlow, F. H. & Welch, J. E. (1965), 'Numerical calculation of time-dependent viscous incompressible flow of fluid with free surface', *The physics of fluids* **8**(12), 2182–2189.

Kaus, B. J. (2010), 'Factors that control the angle of shear bands in geodynamic numerical models of brittle deformation', *Tectonophysics* **484**(1-4), 36–47.

Kaus, B. J., Mühlhaus, H. & May, D. A. (2010), 'A stabilization algorithm for geodynamic numerical simulations with a free surface', *Physics of the Earth and Planetary Interiors* **181**(1-2), 12–20.

Kaus, B. J., Popov, A. A., Baumann, T., Pusok, A., Bauville, A., Fernandez, N. & Collignon, M. (2016), Forward and inverse modelling of lithospheric deformation on geological timescales, *in* 'NIC Symposium 2016-Proceedings, NIC Series, Jülich, DE'.

Lade, P. & De Boer, R. (1997), 'The concept of effective stress for soil, concrete and rock', *Geotechnique* **47**(1), 61–78.

Le Pourhiet, L. (2013), 'Strain localization due to structural softening during pressure sensitive rate independent yielding', *Bulletin de la Société Géologique de France* **184**(4-5), 357–371.

Lechmann, S., Schmalholz, S., Hetenyi, G., May, D. & Kaus, B. (2014), 'Quantifying the impact of mechanical layering and underthrusting on the dynamics of the modern India-Asia collisional system with 3-D numerical models', *Journal of Geophysical Research: Solid Earth* **119**(1), 616–644.

Lemiale, V., Mühlhaus, H.-B., Moresi, L. & Stafford, J. (2008), 'Shear banding analysis of plastic models formulated for incompressible viscous flows', *Physics of the Earth and Planetary Interiors* **171**(1-4), 177–186.

LiU, H.-P., Anderson, D. L. & Kanamori, H. (1976), 'Velocity dispersion due to anelasticity; implications for seismology and mantle composition', *Geophysical Journal of the Royal Astronomical Society* **47**(1), 41–58.
URL: *http://dx.doi.org/10.1111/j.1365-246X.1976.tb01261.x*

Lukawski, M. Z., Anderson, B. J., Augustine, C., Capuano Jr, L. E., Beckers, K. F., Livesay, B. & Tester, J. W. (2014), 'Cost analysis of oil, gas, and geothermal well drilling', *Journal of Petroleum Science and Engineering* **118**, 1–14.

Majer, E. L., Baria, R., Stark, M., Oates, S., Bommer, J., Smith, B. & Asanuma, H. (2007), 'Induced seismicity associated with enhanced geothermal systems', *Geothermics* **36**(3), 185–222.

Mignan, A., Landtwing, D., Kästli, P., Mena, B. & Wiemer, S. (2015), 'Induced seismicity risk analysis of the 2006 Basel, Switzerland, Enhanced Geothermal System project: Influence of uncertainties on risk mitigation', *Geothermics* **53**, 133–146.

Miller, S. A. & Nur, A. (2000), 'Permeability as a toggle switch in fluid-controlled crustal processes', *Earth and Planetary Science Letters* **183**(1-2), 133–146.

Moeck, I. S. (2014), 'Catalog of geothermal play types based on geologic controls', *Renewable and Sustainable Energy Reviews* **37**, 867–882.

Moresi, L., Quenette, S., Lemiale, V., Meriaux, C., Appelbe, B. & Mühlhaus, H.-B. (2007), 'Computational approaches to studying non-linear dynamics

of the crust and mantle', *Physics of the Earth and Planetary Interiors* **163**(1-4), 69–82.

Müller, H. R., Garitte, B., Vogt, T., Köhler, S., Sakaki, T., Weber, H., Spillmann, T., Hertrich, M., Becker, J. K., Giroud, N. et al. (2018), Implementation of the full-scale emplacement (FE) experiment at the Mont Terri rock laboratory, *in* 'Mont Terri Rock Laboratory, 20 Years', Springer, pp. 289–308.

Munn, E. (1979), 'Environmental impact assessment'.

Murrell, S. (1964), 'The theory of the propagation of elliptical Griffith cracks under various conditions of plane strain or plane stress: Parts II and III', *British Journal of Applied Physics* **15**(10), 1211.

Nur, A. (1971), 'Effects of stress on velocity anisotropy in rocks with cracks', *Journal of Geophysical Research* **76**(8), 2022–2034.

Osborn, S. G., Vengosh, A., Warner, N. R. & Jackson, R. B. (2011), 'Methane contamination of drinking water accompanying gas-well drilling and hydraulic fracturing', *proceedings of the National Academy of Sciences* **108**(20), 8172–8176.

Paterson, M. S. & Wong, T.-f. (2005), *Experimental rock deformation-the brittle field*, Springer Science & Business Media.

Plenkers et al., K. (2019), NAGRA NIB18027 - quantifying seismic velocities in backfill of full-scale emplacement experiment, Technical report, Gesellschaft für Materialprüfung und Geophysik mbH.

Plenkers, K., Fischer, T. & Dörner, D. (2017), 'Technical Note 2017-13 - Analyses of seismic velocities in FE Experiments using two acoustic sensor arrays'.

Poliakov, A. N., Herrmann, H. J., Podladchikov, Y. Y. & Roux, S. (1994), 'Fractal plastic shear bands', *Fractals* **2**(04), 567–581.

Popov, A. & Sobolev, S. (2008), 'SLIM3D: A tool for three-dimensional thermomechanical modeling of lithospheric deformation with elasto-visco-plastic rheology', *Physics of the Earth and Planetary Interiors* **171**(1-4), 55–75.

Pusok, A. & Kaus, B. J. (2015), 'Development of topography in 3-D continental-collision models', *Geochemistry, Geophysics, Geosystems* **16**(5), 1378–1400.

Roscoe, K. H. (1970), 'The influence of strains in soil mechanics', *Geotechnique* **20**(2), 129–170.

Rozhko, A., Podladchikov, Y. & Renard, F. (2007), 'Failure patterns caused by localized rise in pore-fluid overpressure and effective strength of rocks', *Geophysical Research Letters* **34**(22).

Schmeling, H., Babeyko, A., Enns, A., Faccenna, C., Funiciello, F., Gerya, T., Golabek, G., Grigull, S., Kaus, B., Morra, G. et al. (2008), 'A benchmark comparison of spontaneous subduction models-Towards a free surface', *Physics of the Earth and Planetary Interiors* **171**(1-4), 198–223.

Seiphoori, A. (2014), 'Thermo-hydro-mechanical characterisation and modelling of MX-80 granular bentonite'.

Shapiro, S. & Dinske, C. (2009), 'Fluid-induced seismicity: Pressure diffusion and hydraulic fracturing', *Geophysical Prospecting* **57**(2), 301–310.

Siegesmund, S., Popp, T., Kaufhold, A., Dohrmann, R., Graesle, W., Hinkes, R. & Schulte-Kortnack, D. (2014), 'Seismic and mechanical properties of Opalinus Clay: Comparison between sandy and shaly facies from Mont Terri (Switzerland)', **71**, 3737–3749.

Simpson, G. (2017), *Practical Finite Element Modeling in Earth Science Using Matlab*, John Wiley & Sons.

Skempton, A. (1984), 'Effective stress in soils, concrete and rocks', *Selected papers on soil mechanics* **1032**, 4–16.

Spillmann, T. & Philipp, J. (2015), 'Technical Note 2015-27 - Geophysical Monitoring and Installation of Acoustic Sensors for the FE Experiment'.

Third Energy (2017), Hydraulic fracture plan for Well KM-8, Kirby Misperton Alpha wellsite, Technical report, Third Energy. http://www.third-energy.com.

Vengosh, A., Warner, N., Jackson, R. & Darrah, T. (2013), 'The effects of shale gas exploration and hydraulic fracturing on the quality of water resources in the United States', *Procedia Earth and Planetary Science* **7**, 863–866.

Vermeer, P. (1990), 'The orientation of shear bands in biaxial tests', *Geotechnique* **40**(2), 223–236.

Vermeer, P. A. & De Borst, R. (1984), 'Non-associated plasticity for soils, concrete and rock', *HERON, 29 (3), 1984* .

Wetzig, V. & Reinhold, M. (2014), 'Technical Note 2012-97 - FE-C experiment: Mechanical lab investigations on low-pH shotcrete samples during the excavation of the Gallery FE'.

Acknowledgments

This project has received funding from the European Union's Horizon 2020 research and innovation program under the Marie Sklodowska-Curie grant agreement No 642029, CREEP.

Declaration

I hereby declare that the contents of this dissertation are original and have not been submitted for any other degree or qualifications. This dissertation is the result of my own work, except where specifically indicated in the text.

Erklärung

Ich versichere hiermit gemäß §10 Abs. 3d der Promotionsordnung des Fachbereichs 09 (Chemie, Pharmazie und Geowissenschaften) der Johannes Gutenberg-Universität Mainz vom 24.07.2007, die als Dissertation vorgelegte Arbeit selbständig und nur unter Verwendung der in der Arbeit angegebenen Hilfsmittel verfasst zu haben. Ich habe oder hatte die hier als Dissertation vorgelegte Arbeit nicht als Prüfungsarbeit für eine staatliche oder andere wissenschaftliche Prüfung eingereicht. Ich hatte weder die jetzt als Dissertation vorgelegte Arbeit noch Teile davon bei einer anderen Fakultät bzw. einem anderen Fachbereich als Dissertation eingereicht.

_____

(Beatriz Martínez Montesinos)
Mainz, 8.05.2019